Department of Precision and Microsystems Engineering

Foldable FEM: using enriched and mixed/hybrid methods for the mesh-independent modeling of folds

M.J.B. Theulings

Report no	:	2019.039
Coach	:	A.M. Aragón and S. van den Boom
Professor	:	R.A.J. van Ostayen, S.R. Turteltaub and F. van Keulen
Specialisation	:	Engineering Mechanics
Type of report	:	Master of Science Thesis
Date	:	2 November 2019

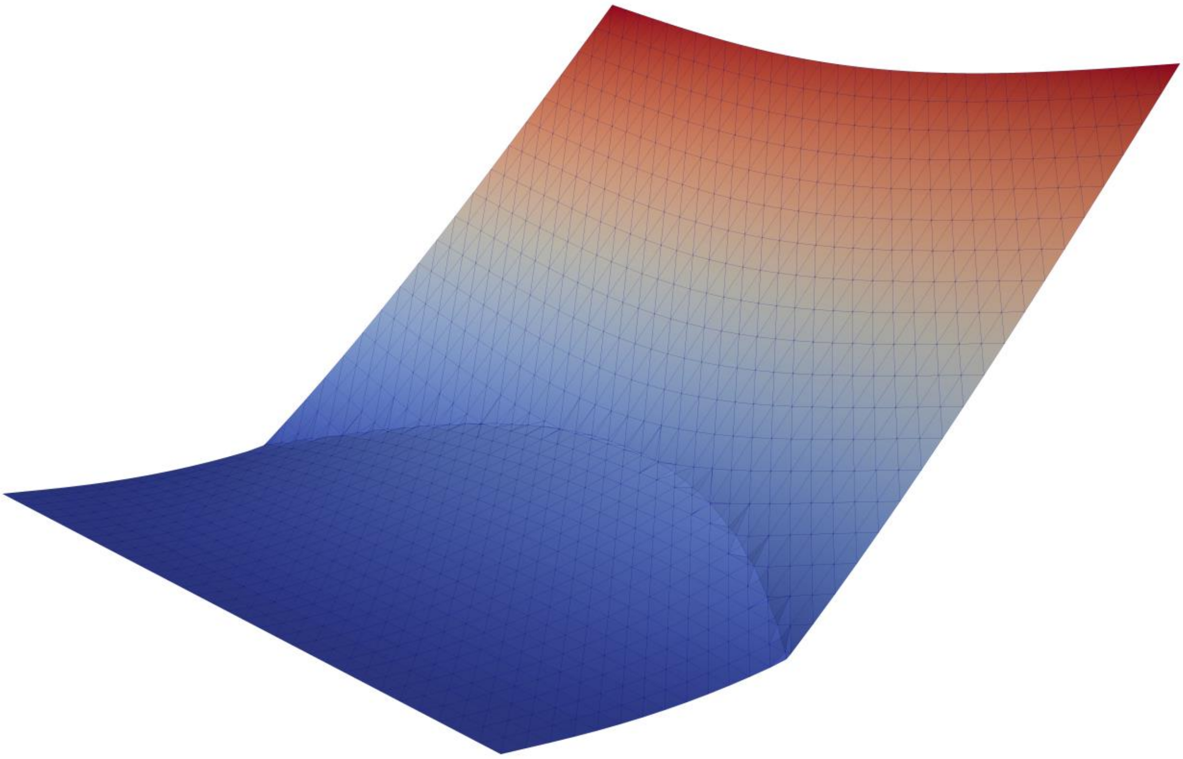

Delft University of Technology
Challenge the future

Foldable FEM: using enriched and mixed/hybrid methods for the mesh-independent modeling of folds

by

Maarten Theulings

to obtain the degree of Master of Science
at the Delft University of Technology,
to be defended publicly on Tuesday November 19, 2019 at 13:00 PM.

Student number:	4326539	
Project duration:	September, 2018 – November, 2019	
Thesis committee:	Prof. dr. ir. F. van Keulen,	TU Delft, chair
	Dr. A.M. Aragón,	TU Delft, supervisor
	Dr. ir. R.A.J. van Ostayen,	TU Delft
	Dr. S.R. Turteltaub,	TU Delft
	Ir. S.J. van den Boom,	TNO, supervisor

Abstract

Due to their lightweight, compact, and stiff properties, origami structures have become of increasing importance in the field of engineering. Many applications of origami structures have been found, ranging from deployable solar arrays to roof panel design. However, most current methods of origami modeling assume facets to be infinitely stiff, or approximate a folded structure using bar-hinge models, creating fast but often inaccurate simulations. To design fast and accurate origami models, progress is being made into incorporating origami modeling in the Finite Element Method (FEM). Folds can be incorporated in FEM either on conforming meshes using interface elements or on non-conforming meshes using enriched elements. When implementing an arbitrarily located fold on an existing mesh using interface elements, re-meshing would be required. However, when using enriched elements, no re-meshing is required, which would be an advantage in fold pattern optimization of origami structures.

This thesis is therefore aimed at deriving foldable Kirchhoff-Love plate elements, using a mixed/hybrid element formulation in combination with an enriched finite element formulation. By using a mixed/hybrid element formulation, an enrichment function on the plate can be greatly simplified, because the discontinuous rotation field is evaluated only at the boundaries of the enriched elements. As a preliminary one-dimensional study, a foldable beam element is examined, and different options for a moment field enrichment are investigated with respect to accuracy and stability. Thereafter, six foldable plate elements of varying complexity are derived in detail, using constant and linear moment fields. Stability of the elements is improved by local condensation of the enriched elements, or by applying a precondition matrix. All enriched elements are formulated using linear folds; curved folds are modeled by piecewise linear approximations of the curve within each enriched element.

The enriched formulation is evaluated using several benchmark tests. Foldable constant moment elements are found to have a convergence behavior similar to the behavior found using standard FEM on a conforming mesh. Foldable linear moment elements are found to attain lower convergence rates than expected. In the enriched elements a trade of between accuracy and matrix condition is observed, elements with lower errors have worse condition numbers and vice versa.

Acknowledgements

The past year, working on this thesis, I found myself liking the scientific process very much. Reading about the theories and derivations used in this thesis, and experimenting with the formulas myself, brought me excitement when formulations or insights were found. Although I had a lot of fun creating the theoretical background, I had some difficulties in coding and writing for my thesis. Luckily I could always reach my daily supervisor Sanne van den Boom when I found myself stuck in these problems. Furthermore, I would like to thank Alejandro Aragón and Fred van Keulen for the help and nice discussions we had about the thesis.

Beside technical help a lot of people helped me on a personal level. My girlfriend Emma Polman who helped me relax when I was stuck on a problem, and the board of ”De Bolk” where I spent many days working on my thesis and with whom I had many lunches.

The past year has been a great learning experience, and a successful conclusion of my master studies. I am looking forward to the PhD I will be starting in cooperation with the NLR in Amsterdam and the many exiting things I will continue to learn.

Maarten Theulings
Delft, November 2019

Contents

1

Introduction

Origami, the ancient art of paper folding, originates from fourteenth century Japan [1]. Recently, more and more applications for origami in engineering have been found, for instance: deployable solar arrays and antennas [2, 3], acoustic beam steering [4], self-folding robots [5], design of metamaterials [6], and deployable shelters [7]. For the proper design of these origami structures, adequate modeling tools are required to accurately predict their mechanical behavior.

Current modeling tools, such as rigid foldability analysis [8] and truss-based analysis [9], approximate kinematic and structural properties, but are limited in the accurate modeling of deformable origami and design flexibility for structural optimization. When folds are seen as discontinuities in the rotational field, enriched finite element methods, like the Discontinuity-Enriched Finite Element Method (DE-FEM) [10] and the Interface-enriched Generalized Finite Element Method (IGFEM) [11], could prove to be useful in origami modeling. Using these methods, a fold pattern and underlying finite element discretization can be decoupled, creating an accurate and flexible method for origami modeling.

1.1. Numerical methods for origami modeling

Three main numerical approaches for origami modeling can be found in the literature, in increasing order of complexity, they are:

- **Rigid foldability analysis**, as introduced in [8], is used when mechanical properties are not important for a design, but kinematic properties are. It models rigidly foldable structures, ignoring mechanical effects of facet deformation and torsional fold stiffness. The model is constructed by creating constraints around fold vertices [12], and projecting the folded structure on these constraints. Although rigid origami simulations are useful to model a folding process, the problem of introducing finite stiffness in the simulated structures and calculating accurate stress distributions remains.

- **Truss-based analysis** is used when there is no interest in the minutiae of the displacement and stress distributions throughout the origami structure, but there is interest in the overall mechanical behavior of the structure, or the effects of varying stiffness [9]. In truss-based analysis, the origami structure is modeled as a pin-joint network where each vertex of the origami structure is modeled as a pin joint connected to the other vertices via bar elements. Bending behavior of the fold is added by adding degrees of freedom (DOFs) containing the fold angle to the bars along fold lines, and coupling the fold angle to a torsional stiffness (K_{fold}). Bending behavior of the facets is added by triangulating the facets and adding DOFs in a similar way as for the folds, but with a higher torsional stiffness ($K_{facet} > K_{fold}$), as in Figure 1.1. The power in this method lies in its simple description of the internal mechanics and kinematics, which can be used to create a general design for an origami structure, but not for analysing detailed designs.

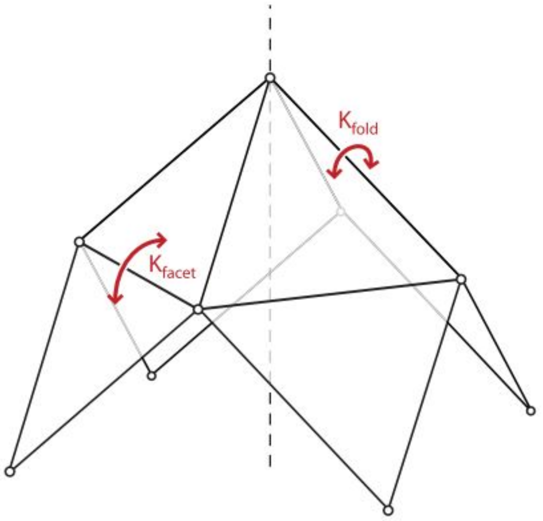

Figure 1.1: A pin joint representation of a simple origami structure. Facets are triangulated to add a facet stiffness, K_{facet}. Along fold lines the torsional stiffness K_{fold} is added. [9]

- **The finite element method with interface elements** is used in the modeling of structures with predefined fold patterns along which interface elements elements can be placed. Simple interface elements behaving like hinges with a torsional stiffness have been used in [13]. More complicated hinge elements include kinematic and constitutive equations particular to folds [14]. In [13], it is found that in certain origami structures, where membrane deformations are dominant, creating hinge elements which take into account compression and stretching of the crease line could improve accuracy of the solution. Although interface elements in combination with finite element analysis can create highly accurate descriptions of displacement and stress distributions, it lacks flexibility. Hinge elements need to be placed on the interface between two plate or shell elements, and the mesh thus needs to be conforming to the fold-pattern. Imposing an arbitrary fold on an existing mesh would thus require a modification of the mesh. Modifying a mesh is not desired in problems where the fold-pattern is not known a priori, such as fold-pattern optimization, where creating a fold-conforming mesh for every intermediate design would take considerable computational time.

In Table 1.1, based on the described literature, an overview of the capabilities of the methods is given; the methods are rated for their design flexibility and accuracy in their calculated displacement field and stress distribution. All three methods are able to calculate the displacement field and stress distribution to varying accuracy, but none of the methods combine accurate solutions with design flexibility. Using interface elements in combination with the Finite Element Method (FEM), highly detailed descriptions of the displacement and stress distribution are achieved. However, design flexibility is limited, and needs to be improved. Enriched Finite Element Analysis (Enriched FEM) is a method which can be used to impose a fold on a finite element mesh, without the need for a conforming mesh. Using Enriched FEM to model folds could result in a highly accurate and flexible modeling tool.

	Displacement field	Stress distribution	Design flexibility
Rigid foldability analysis	✓	✗	-
Truss-based analysis	-	-	-
Interface elements	✓	✓	✗

Table 1.1: The three existing methods for origami modeling rated in their displacement and stress distribution accuracy, and their design flexibility.

1.2. Enriched finite element method

Enriched FEM is a method used to introduce discontinuities on finite elements. Since a fold can be seen as a discontinuity in rotation, these methods show great promise in fold modeling. In enriched FEM, the standard finite element approximation space is augmented with functions reflecting *a priori* known information about the problem [15]. The augmentation is based around designing adequate enrichment functions for the standard shape functions of an element. An example of enriched FEM are the eXtended/Generalized Finite Element Methods (X/GFEM) [16, 17]. X/GFEM allows any function $\Psi(\boldsymbol{x})$, to be added to a local finite element space Ω, using a partition of unity, $\sum_{j\in J} N_j(\mathbf{x}) = 1$ on Ω and 0 everywhere else, as:

$$\mathbf{u}^h(\boldsymbol{x}) = \sum_{i\in I} \mathbf{u}_i N_i(\boldsymbol{x}) + \sum_{j\in J} \mathbf{b}_j N_j(\boldsymbol{x}) \sum_{k\in K} \Psi_k(\boldsymbol{x}), \tag{1.1}$$

where $\mathbf{u}_i$ are the standard element DOFs, $N(\boldsymbol{x})$ the standard shape functions, $\boldsymbol{b}_j$ the enriched DOFs (added to the standard nodes), and $\Psi(\boldsymbol{x})$ the enrichment function. In X/GFEM the completely cracked element in Figure 1.2 is modeled by introducing the Heaviside function as the enrichment function, $\Psi(\boldsymbol{x}) = H(\boldsymbol{x})$, where the enriched DOFs ($\boldsymbol{b}_j$) of the completely cracked element are located at the circled standard element nodes. Elements containing a crack tip are furthermore enriched using asymptotic crack tip functions. Using standard quadrature on the enriched element, the enrichment function will not be properly integrated because it is by definition a discontinuous function. Quadrature for the enriched element is commonly done by partitioning the element into subdomains called *integration elements*, as in Figure 1.3; on these *integration elements*, standard Gaussian quadrature is used for numerical integration.

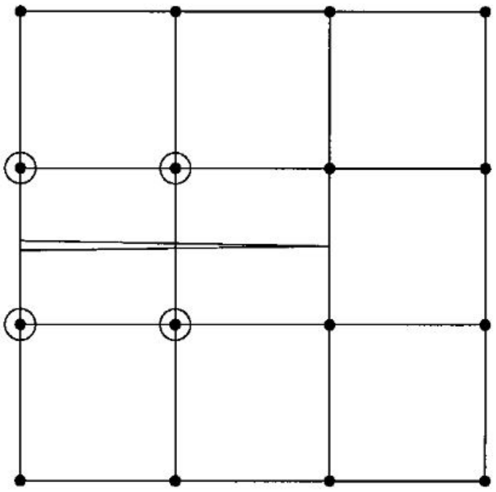

Figure 1.2: 2D cracked surface with enriched DOFs for the completely cracked element located at the circled nodes. [16]

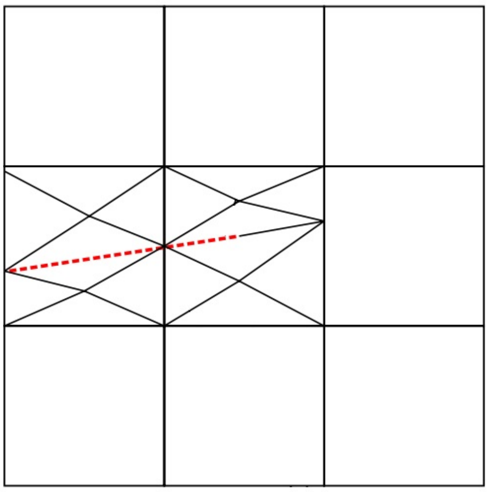

Figure 1.3: The cracked surface as in Figure 1.2 with the enriched elements divided into triangular sub-elements for numerical integration. [16]

An often observed problem in enriched FEM is ill-conditioning of the stiffness matrix leading to a loss of accuracy [18]. Different methods can be used to improve conditioning, preconditioning improves the matrix condition but requires extra computational steps like post-processing and the formulation of the precondition matrix [19]. In the Stable Generalized Finite Element Method (SGFEM) [18], the finite element space is enriched with functions representing the *a priori* known solution minus the used standard shape functions. Using this finite element space, the enrichment and standard finite element interpolation become almost orthogonal with respect to the inner energy product, causing an improved matrix condition [20]. The Strongly Stable Generalized Finite Element Method (SSGFEM) [21], is the subject of ongoing research to find stable and accurate X/GFEM formulations. A X/GFEM is an SSGFEM if it has the same order of convergence and similar matrix condition as standard

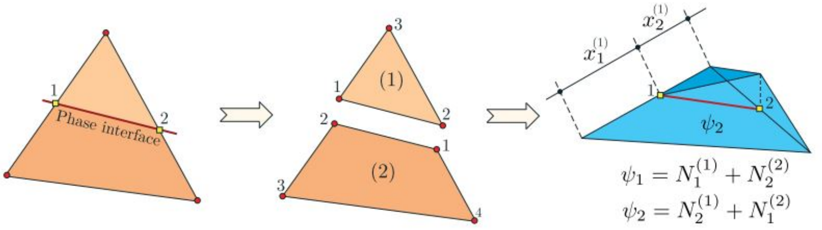

Figure 1.4: An enriched triangular finite element divided into a triangular (1) and a quadrilateral (2) sub-element by the enriched nodes located at the intersection of the discontinuity and element edge. The enrichment functions connected to the enriched nodes are constructed by combining two Lagrangian shape functions on sub-elements (1) and (2). [22]

FEM, and if the condition of the enriched part of the stiffness matrix is bound independent of mesh and discontinuity.

The main advantage of X/GFEM is the method's ability to model discontinuities, without the need to create a conforming mesh for the problem. This flexibility comes at the cost of a demanding geometric engine, which needs to detect discontinuities and subdivide elements into integration elements. A difficulty of the method is the correspondence between the DOFs of enriched elements and adjacent non-enriched elements. Due to the enriched DOFs being located at the standard nodes, the standard DOFs at these nodes do not correspond to the displacements at these nodes. The lack of a direct physical connection between displacement and the DOFs at enriched nodes creates difficulties in physical interpretation of the results, and the implementation of Dirichlet boundary conditions.

An alternative to X/GFEM is the Interface-enriched Generalized Finite Element Method (IGFEM) [11]. IGFEM was initially proposed for problems with jumps in their gradient field, also known as weak discontinuities. An example of such a problem would be the displacement field of a composite material with different material phases in parts of the overall structure. The main advantage of IGFEM over X/GFEM is the location of the enriched DOFs; instead of locating them at the standard nodes they are located at newly generated enriched nodes, positioned at the intersections between discontinuities and element edges, as illustrated in Figure 1.4. In IGFEM the formulation of the enriched finite element space becomes:

$$\boldsymbol{u}^h(\boldsymbol{x}) = \sum_{i=1}^{n} N_i(\boldsymbol{x})\boldsymbol{u}_i + \sum_{i=1}^{n_{en}} s_i \Psi_i(\boldsymbol{x})\boldsymbol{\alpha}_i, \tag{1.2}$$

where the first part represents the standard FEM formulation, n_{en} is the number of enriched nodes, Ψ_i the enrichment functions, $\boldsymbol{\alpha}_i$ the enriched DOFs, and s_i a scaling parameter for the enrichment. To ensure continuity throughout the mesh, enriched DOFs are shared between adjacent elements. The enrichment functions are constructed by combining standard Lagrange shape functions in integration elements created by the discontinuity, as shown in Figure 1.4. At standard nodes, the enrichment functions vanish, allowing the standard DOFs to retain their physical interpretation. A major advantage of IGFEM is the easy implementation of Dirichlet boundary conditions. Since standard DOFs retain their physical interpretation, boundary conditions can be implemented using standard FEM procedures[11]. Enriched element stiffness matrices can become ill-conditioned when discontinuities come arbitrarily close to standard nodes. To partially solve this problem the scaling factor s_i is introduced, which decreases the enrichment function for enriched nodes close to the standard nodes. As in X/GFEM standard Gaussian integration on the enriched element can not be performed, and sub-elements are used to define the quadrature.

Many applications and advancements of IGFEM have already been implemented and tested. In [23] the hierarchical interface-enriched finite element method (HIFEM) is introduced as an improvement upon IGFEM. HIFEM is used to model problems including many discontinuities and multiple interfaces crossing a single element. Within the IGFEM framework, curved interfaces can be modeled by piecewise linear approximations of the interface within an element, this approximation can cause an increase in error. In [22] this error is decreased by increasing the number of integration elements in h-IGFEM, or by using higher order integration elements in p-IGFEM. Due to the higher-order enrichment functions, p-IGFEM more accurately captures the stress concentration in the vicinity of interfaces, and it is found to be superior to h-IGFEM. Besides the application of IGFEM to 2D problems, the method is also proven to work for 3D problems in [24, 25]. For many problems, the convergence behavior of IGFEM with a non-matching mesh, was found to be similar to the convergence behavior of standard FEM using a matching mesh [11, 24]. Often, equal convergence rates and similar levels of accuracy are found, using IGFEM and standard FEM.

Building upon IGFEM, the Discontinuity-Enriched Finite Element Method (DE-FEM) is introduced in [10]. The main advancement of DE-FEM over IGFEM lies in the ability to model both weak and strong discontinuities by adding not only weak but also strong enrichment functions. Strong enrichment functions are needed in problems where the solution field includes a jump, an example is the modeling of a cracked surface. Using DE-FEM, the formulation of the enriched finite element space becomes:

$$\boldsymbol{u}^h(\boldsymbol{x}) = \sum_{i=1}^{n} N_i(\boldsymbol{x})\boldsymbol{u}_i + \sum_{i=1}^{n_w} s_i \Psi_i(\boldsymbol{x})\boldsymbol{\alpha}_i + \sum_{i=1}^{n_s} s_i \mathrm{X}_i(\boldsymbol{x})\boldsymbol{\beta}_i, \tag{1.3}$$

where the first two terms are the IGFEM formulation, X_i are the strong enrichment functions and $\boldsymbol{\beta}_i$ the enriched DOFs located at enriched nodes. Strong enrichment functions are created similarly to the weak enrichment functions, by combining Lagrange shape functions on the subdomains created by the discontinuity.

1.3. Enriched methods for plates

Most existing research on enriched plate elements has been focused on deriving cracked plate or shell elements using X/GFEM. Although, the aim of this thesis is to derive foldable plate elements, reviewing the current work on enriched plate elements for strong discontinuities gives a good indication of the possibilities and difficulties in enriching plate elements. A cracked plate element using Reissner-Mindlin plate theory was first introduce in [26]. In Reissner-Mindlin plates, the displacement and rotational fields are not directly related, and only C^0-continuity is required for both fields. Separate enrichment functions can thus be defined for both fields, and completely cracked elements are enriched using simple step functions, as commonly used in X/GFEM. In addition, elements containing a crack tip are enriched using specialized crack tip enrichment functions for plates. The formulation of [26] is extended to shells and crack propagation in [27]. A difficulty in modeling cracked shell elements with large displacements is the correct representation of the crack opening. The director, a unit vector representing the direction in which the plate displaces, is different in the two subdomains created by a crack. For this reason, a different interpretation of the X/GFEM enrichment is implemented in [27]. Instead of decomposing the displacement in a standard and enriched displacement field, the director field is enriched using decomposed degrees of freedom as:

$$u_{Ki} = u_{Ki}^{std} + H_K(\xi)u_{Ki}^{*} \tag{1.4}$$

$$\theta_{Ki} = \theta_{Ki}^{std} + H_K(\xi)\theta_{Ki}^{*}, \tag{1.5}$$

where the DOFs u_{Ki}, θ_{Ki}, are defined using their standard part u_{Ki}^{std}, θ_{Ki}^{std}, and their discontinuous part u_{Ki}^{*}, θ_{Ki}^{*}, and $H_K(\xi)$ is a function discontinuous over the crack. Consequently, the displacement field is defined as:

$$\boldsymbol{u} = \sum_{K=1}^{4} N_K(\xi)\boldsymbol{u}_K + \sum_{K=1}^{4} \frac{h\xi_3}{2} N_K(\xi)\Delta\boldsymbol{t}_K, \tag{1.6}$$

where $\Delta\boldsymbol{t}_K(\theta_{Ki})$ are the nodal director variables as a function of the nodal rotations θ_{Ki}, N_K the standard shape functions, h the plate thickness, and ξ_3 the out of plane coordinate.

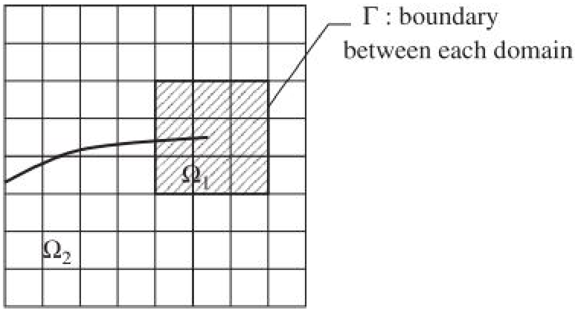

Figure 1.5: A cracked finite element mesh, crack tip enrichmnets span the entire domain depicted by Ω_1.

In [28] the effect of crack tip enrichments in shell elements is examined. Using crack-tip enrichments, more accurate fracture behavior can be modelled, at the expense of increased computational time and matrix condition number. Reissner-Mindlin plate theory is known to cause shear locking for thin plates. In [26], the enriched plate elements are based on standard locking free Reissner-Mindlin plate elements, but in the enriched elements shear locking is again observed. A solution for the shear locking in enriched plate elements, is the use of Kirchhoff-Love plate elements, which generally do not suffer from shear locking.

In Kirchhoff-Love plate elements, the displacement w and rotation $\boldsymbol{\phi}$ are related through $\nabla w = \boldsymbol{\phi}$. This relation causes the shape function for both fields to be coupled, and requires the displacement to be C^1-continuous in elements and over inter-element boundaries [29]. In enriched Kirchhoff-Love plate elements, the enrichment functions of the displacement field need to reflect both discontinuities in the displacement and the rotational field. In [30] a cracked Kirchhoff-Love plate is derived using X/GFEM. Completely cracked elements are enriched with a step function spanning one element, but crack tip enrichmnets often span several elements, as shown in Figure 1.5. Implementing the crack tip enrichment using X/GFEM, each node of the elements in the crack tip enriched finite element space Ω_1 is enriched, and many enriched DOFs are included. Generally, a lot of additional DOFs in a crack tip area leads to a high condition number [31]. To reduce the additional DOFs connected to the crack tip enrichment, *XFEM DOF gathering with pointwise matching*, as in [31], is used for the crack tip enrichment. Using this technique, the displacement field within Ω_1 is enriched with only four additional DOFs as:

$$u_1^h = \sum_{i \in N_1} a_i N_i(\boldsymbol{x}) + \sum_{j \in J_1} b_j H(\boldsymbol{x}) N_j(\boldsymbol{x}) + \sum_{i=1}^{4} c_i F_i(\boldsymbol{x}) \quad \text{in } \Omega_1, \tag{1.7}$$

where the first two terms is the standard X/GFEM formulation, c_i the four enriched DOFs, and F_i the four enrichment functions. Since the crack tip enrichments F_i offend C^1-continuity over the boundary between the Ω_1 and Ω_2 (Γ in Figure 1.5) *integral matching* is applied on the displacement (u_1, u_2) to ensure rotational continuity in the two subdomains (Ω_1, Ω_2), as:

$$\int_\Gamma u_1 \lambda d\Gamma = \int_\Gamma u_2 \lambda d\Gamma \ \forall \lambda \in \Lambda, \tag{1.8}$$

where Λ is a space of appropriate multipliers to ensure inter-element continuity. Advancing on [30], a cracked Kirchhoff-Love shell element is derived in [32]. As was the case in the cracked Reissner-Mindlin plate, the director field is discontinuous along the crack and is thus enriched. In the cracked elements a piecewise enrichment strategy is used, described in [32] as: " ...an independent interpolation for the displacement for both sides of a cracked finite element." Instead of augmenting the finite element space by adding a discontinuous displacement enrichment to the standard displacement interpolations, a fully discontinuous finite element space is thus used.

Not much work on enriched plate elements for fold modeling has been done, but recent work by Barbieri *et al.* [33] introduces the possibility of including folds in non-linear plates using an enriched formulation. Instead of using a finite element setting, Barbieri *et al.* uses a meshfree setting to model a plate and its discontinuities, and is thus not an enriched FEM. A von Kármán plate is used to model flat plates that develop ridge like deformations as a result of the applied loads, the plates are thus not used to model pre-folded structures. Furthermore, since no fold stiffness is introduced, the model is not yet suited to accurately model the mechanics of origami structures. The plate is based in Reissner-Mindlin theory, and only an enrichment for the rotational field is introduced. The problem of shear locking is solved by using a full third order polynomial basis for the shape functions, obtained using the Reproducing Kernel Particle Method (RKPM) [34]. This method allows the accurate modeling of plates with a thickness to length ratio of up to $\frac{h}{L} = 10^{-2}$. The main aim of Barbieri *et al.* is to show that it is possible to model folds, using the same methods developed for cracks, and the results in Figure 1.6 clearly illustrate this possibility. To avoid shear locking in foldable plates, it is suggested to use Kirchhoff-Love plates in combination with X/GFEM. To account for the fold, Barbieri *et al.* proposes to introduce the discontinuities of the rotational field directly into the derivatives of the displacement field enrichment.

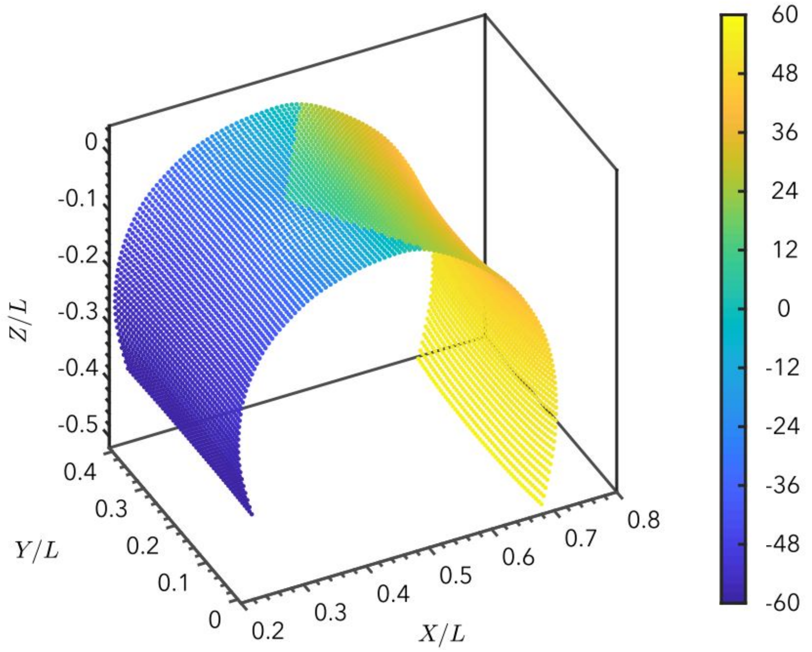

Figure 1.6: A folded plate modeled using the finite strain large deformation enriched plate derived in [33].

1.4. Mixed/hybrid elements

Elements derived using a different field in their formulation than the field they calculate in their matrix equations are called mixed/hybrid elements [35]. Using another field, besides the displacement or rotational field in the finite element formulation, could simplify enrichment functions. Generally, a mixed/hybrid element formulation is constructed by introducing interpolation functions for two types of fields; the primary and the auxiliary field:

$$\boldsymbol{u}^h = \boldsymbol{L}(\boldsymbol{x})\boldsymbol{q}, \tag{1.9}$$

where $\boldsymbol{u}^h$ is the primary field that is of main interest, $\boldsymbol{q}$ are the primary DOFs, and $\boldsymbol{L}(\boldsymbol{x})$ are the shape functions. As auxiliary field, often the element stress is used:

$$\boldsymbol{\sigma}^h = \boldsymbol{P}(\boldsymbol{x})\boldsymbol{\beta}, \tag{1.10}$$

where $\boldsymbol{\sigma}^h$ is the auxiliary field, $\boldsymbol{\beta}$ the auxiliary DOFs, and $\boldsymbol{P}(\boldsymbol{x})$ the auxiliary shape functions. Using these fields, a problem specific energy function for a finite element can be expressed as [35]:

$$U = -\frac{1}{2}\boldsymbol{\beta}^{\mathrm{T}}\boldsymbol{A}\boldsymbol{\beta} + \boldsymbol{\beta}^{\mathrm{T}}\boldsymbol{B}\boldsymbol{q} - \boldsymbol{f}^{\mathrm{T}}\boldsymbol{q}, \tag{1.11}$$

where $\boldsymbol{f}$ is a vector containing the applied loads, $\boldsymbol{A}$ is a matrix connected to the energy inside an element, and $\boldsymbol{B}$ a matrix connecting the auxiliary and primary fields. In the energy function, kinematic relations are often enforces via Lagrange multipliers. Using virtual variations, the final stiffness equations can be expressed as:

$$\boldsymbol{K}\boldsymbol{q} = \boldsymbol{B}^{\mathrm{T}}\boldsymbol{A}^{-1}\boldsymbol{B}\boldsymbol{q} = \boldsymbol{f}. \tag{1.12}$$

A mixed/hybrid element formulation may simplify the enrichment functions, required for a folded plate element. Using IGFEM or DE-FEM, C^0- continuous and C^{-1}-continuous shape functions can be added in a finite element formulation. A folded plate element has a displacement field which is C^0-continuous and rotation field which is C^{-1}-continuous. Furthermore, the enrichment functions created from Lagrange shape functions in DE-FEM and IGFEM can not be used since they would create weak discontinuities along inter-element boundaries, and would thus violate continuity requirements for Kirchhoff-Love plate elements. A solution could be to use *integral matching* as in [30] to ensure C^1-continuity, but this would increase the complexity of the shape functions and quadrature used in enriched elements. Enriching the displacement field to model foldable Kirchhoff-Love elements thus requires complex enrichment functions. Contrary to the displacement field, the moment field of a folded plate is C^0-continuous, and no inter-element moment continuity is required in a finite element formulation. Using the moment field in a mixed/hybrid formulation could thus greatly simplify the enrichment procedure for a folded plate.

To develop further understanding of the use of mixed/hybrid plate formulations in combination with enriched FEM, some non-enriched elements are examined. Many different mixed/hybrid plate formulations have already been proposed. A mixed/hybrid plate element is formulated using Reissner-Mindlin plate theory in [36], where as governing equations, a modified Hellinger-Reissner principle is used. In this governing equation, the potential energy within an element is expressed in terms of the curvature as a function of displacement, rotation, and shear strain. This allows for an independent interpolation for the shear strain, next to the standard interpolation for the displacement and rotation. By introducing an independent shear strain interpolation, the problem of shear locking is reduced and the Reissner-Mindlin elements can be used for relatively thin plates. In [37] the hybrid stress model (HSM) element is formulated, using as governing equations a hybrid stress functional, derived from the Hellinger-Reissner principle for Kirchhoff-Love plates. The hybrid stress functional can be derived from the complementary potential energy for plates by relaxing the natural boundary conditions, and assuming the geometrical boundary conditions to be satisfied [37]. A more detailed derivation of the hybrid stress functional derivation can be found in [38]. In the HSM-element, the only field defined on the plate's surface is a linear moment field. On its boundaries interpolation functions for the displacement and rotation are still required. In a folded plate, enrichment functions for the displacement field would thus only need to be defined on the boundary of the element, and only the moment field would require enrichment functions on the plate's surface.

In [39], among other elements, two Kirchhoff-Love plate elements are derived using a mixed/hybrid formulation, much like the HSM formulation. The two elements assume a constant or a linear moment field in the element, resulting in the $KL0$ and $KL1$ element respectively. The difference between the linear moment HSM and $KL1$ elements is the location and number of DOFs used. The triangular HSM element uses only 9 DOFs, located at the element nodes, while the triangular $KL1$ element uses 12 DOFs, located at the element nodes and sides. As explained in [39], a linear moment plate element has 3 rigid body modes and 9 deformation modes, using less than $3 + 9 = 12$ DOFs in a linear moment element, could lead to elements which react too stiff or contain spurious energy modes.

Besides the non-enriched mixed/hybrid elements, several examples of enriched elements using a mixed/hybrid formulation are found. A Timoshenko beam and Reissner-Mindlin plate containing a material interface are derived in [40]. These elements have continuous displacement and rotational fields, but a discontinuous strain field. Using X/GFEM, the displacement field is enriched with the enrichment function found in [41], which is a hat function similar to the enrichment used in IGFEM. Next to the enriched displacement, an enriched strain field is used as auxiliary field. Although the resulting enriched plate element is based in Reissner-Mindlin plate theory, no locking behavior is observed, which is achieved by a proper choice in strain field interpolations. In [42], the use of X/GFEM in combination with a hybrid/mixed formulation to impose interfacial element constraints is examined. The paper proposes a method which is able to enforce a variety of interface constraints via the use of auxiliary variables. Instead of using virtual variations on the weak formulation to arrive at Equation 1.12, the method defines the stiffness matrix in terms of primary and auxiliary variables, and removes auxiliary variables using static condensation on a local element level.

1.5. Research goal

In order to use optimization algorithms for origami design, flexible modeling methods need to be derived that are able to easily relocate fold lines independently of the mesh. Enriched FEM in combination with a hybrid element formulation has great promise in the derivation of folded elements. Furthermore, Kirchhoff plate theory has the preference over Reissner-Mindlin plate theory, because origami structures are often made of thin sheet materials for which Reissner-Mindlin plates suffer from shear locking. By deriving foldable plate elements this thesis attempts to answer the question:

Can mixed/hybrid Kirchhoff plate elements be enriched using IGFEM to create enriched elements for the accurate modeling of origami structures?

This question can be split into three parts:

1. Can the potential energy equation of a folded plate be expressed in terms of the moment field within the plate?
2. What enrichment functions are required in a mixed/hybrid plate to accurately model the behavior specific to a fold?
3. How does the matrix condition number change for a folded plate element, and how can it be improved?

1.6. Outline

The thesis begins with an investigation into the problem by developing a foldable beam element in Chapter 2. Two options in deriving a foldable beam element emerge from the potential energy formulation and are investigated. Both elements are compared in matrix condition number and accuracy of the solution. Using the lessons learned in the folded beam derivation three plate elements are enriched with a fold in Chapter 3: the KL0 and KL1 elements [39] and the HSM element [37]. Several enrichment techniques are implemented resulting in six foldable elements; the $KL0^{(1)}$, $KL0^{(2)}$, $KL0^{(c)}$, $HSM^{(2)}$, $KL1^{(2)}$, and $KL1^{(c)}$ elements. Appropriate enrichment functions for the elements are derived. In Chapter 4 the three enriched plate elements are compared in accuracy and stability. The accuracy is tested for straight and curved folds by comparing to analytical and numerical solutions. The matrix condition number is tested for folds close to element edges and for a system with an increasingly fine mesh. Finally, in Chapter 5 the results are discussed and suggestions for further advancement of the methods used are given.

2

Foldable Beam

Developing foldable Kirchhoff-Love plate elements using IGFEM, some problems are expected. The displacement field enrichment in IGFEM would lead to C^0-continuity across neighboring element edges, and would thus violate the continuity constraints for Kirchhoff-Love plates. A mixed/hybrid formulation is investigated, to solve the continuity problem for IGFEM in foldable Kirchhoff-Love plate elements. In mixed/hybrid bending elements, a moment field interpolation is used, instead of a displacement field interpolation. Since the moment field does not have to conform to any continuity requirements, the IGFEM enrichment functions can be used to enrich the moment field. As a first step towards the derivation of mixed/hybrid foldable plate elements a foldable beam element will be investigated. Since the beam element is one-dimensional the focus will be on the enriched method, without obscuring the derivation with the tedious bookkeeping, that is required for 2D plates. The lessons learned in this exercise will be used as an input in the 2D plate derivation.

2.1. 1D Problem definition

In Figure 2.1 a beam of length L with a fold located at $x = x_\Gamma$ is depicted, the beam has a displacement field $w(x)$, and rotation field $\phi(x)$. Standard DOFs are defined on the standard nodes at $x = 0$ and $x = L$ as $w_{1,2}$ and $\phi_{1,2}$, and on the enriched node at $x = x_\Gamma$, enriched DOFs are defined as w_Γ, $w_\Gamma^\pm$ and $\phi_\Gamma^\pm$. Point loads $F_{1,2}$ and $M_{1,2}$ are applied on the standard nodes, a distributed load, $q(x)$, is applied on the entire beam, and a force is applied on the fold F_Γ. Compared to standard beam elements, the loads at the left node are oppositely defined. This is done to connect positive loads to positive displacements. To account for the discontinuity, the domain Ω is subdivided into two subdomains,

$$\begin{aligned} \Omega_1 &: 0 \leq x < x_\Gamma, \\ \Omega_2 &: x_\Gamma < x \leq L, \end{aligned} \tag{2.1}$$

$$\text{and the discontinuity } \Gamma. \tag{2.2}$$

The two subdomains do not include the discontinuity since different kinematic and constitutive equations apply at the discontinuity; strictly speaking there are two different values for the rotation at the discontinuity. A short hand notation is introduced to account for approaching the discontinuity form the left (to x_Γ^-), or approaching the discontinuity from the right (to x_Γ^+). Functions approached from either the left or the right will be defined as:

$$\lim_{x \to x_\Gamma^\pm} f(x) = f(x_\Gamma^\pm) = f_\Gamma^\pm. \tag{2.3}$$

Standard kinematic relations are used on the two subdomains,

$$\begin{aligned} \phi(x) &= \frac{\partial w}{\partial x} \text{ on } \Omega_i,\ i = 1, 2, \\ \kappa(x) &= \frac{\partial \phi}{\partial x} \text{ on } \Omega_i, \end{aligned} \tag{2.4}$$

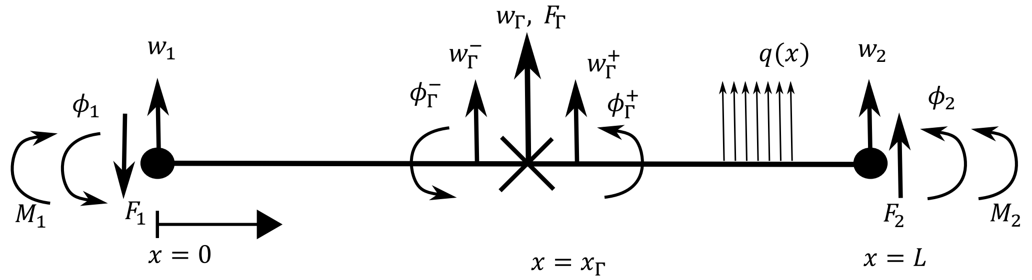

Figure 2.1: The discretized foldable beam element, with a hinge located at the fold (depicted as a cross). The DOFs located on the enriched node at $x = x_\Gamma$, differ from approaching the fold from either the left (ϕ_Γ^-, w_Γ^-) or the right (ϕ_Γ^+, w_Γ^+), with the exception of w_Γ which is located exactly at the fold. Point loads F_i and M_i are applied on the standard and enriched nodes, and a distributed force $q(x)$ is applied on the entire element. The loads applied on the standard nodes and the force applied on the fold (F_Γ) will be used as the external load application in the potential energy derivation.

where $\phi(x)$ is the rotational field, defined as the derivative of the displacement field $w(x)$, and $\kappa(x)$ is the curvature field, defined as the derivative of the rotational field. At the discontinuity, standard kinematic relations do not hold. Instead, to ensure displacement continuity throughout the beam, the displacement on the discontinuity is constrained as:

$$w_\Gamma^- = w_\Gamma^+ = w_\Gamma \text{ on } \Gamma. \tag{2.5}$$

No extra kinematic relations for the rotational field are required, since it will be discontinuous on the fold. As constitutive equation, the standard relation between moment and curvature is used:

$$M(x) = EI\kappa(x) \text{ on } \Omega_i,\ i = 1, 2 \tag{2.6}$$

where E denotes Young's modulus and I the moment of inertia. In addition, it is assumed that the fold behaves as a rotational spring, and a relation between moment and rotation is posed:

$$M_\Gamma = k_t(\phi_\Gamma^+ - \phi_\Gamma^-) = k_t\Delta\phi, \tag{2.7}$$

where M_Γ is the moment at the fold and k_t the rotational stiffness at the fold in N m rad^{-1}.

2.2. Foldable beam derivation

A mixed/hybrid foldable beam element is derived using shape functions for the internal moment field. Auxiliary DOFs connected to the moment field are used in the element formulation, but are removed using virtual variations in the discretization. The standard non-foldable mixed/hybrid beam element formulated in [13], will be expanded with additional terms concerning the discontinuities on the fold. Firstly, the potential energy of a deformed beam is described, and the kinematic equations are enforced by means of Lagrange multipliers. Secondly, the multipliers are interpreted via virtual variations, and the formulation is simplified by using integration by parts.

2.2.1. 1D modified potential energy derivation

The modified potential energy stored in a deformed folded beam, with the kinematic equations enforced via Lagrange multipliers, is expressed as:

$$\Pi = \int_0^{x_\Gamma^-} \left\{ \frac{1}{2}EI\kappa^2 + \lambda_1(\phi - \frac{\partial w}{\partial x}) + \lambda_2(\kappa - \frac{\partial \phi}{\partial x}) - q(x)w \right\} dx + \frac{1}{2}k_t\Delta\phi^2 + \lambda_3(w_\Gamma - w_\Gamma^-) +$$

$$\lambda_4(w_\Gamma^+ - w_\Gamma) + \int_{x_\Gamma^+}^{L} \left\{ \frac{1}{2}EI\kappa^2 + \lambda_5(\phi - \frac{\partial w}{\partial x}) + \lambda_6(\kappa - \frac{\partial \phi}{\partial x}) - q(x)w \right\} dx + W, \tag{2.8}$$

where W, the potential energy of the externally applied loads on the system is:

$$W = F_1 w_1 + M_1 \phi_1 - F_2 w_2 - M_2 \phi_2 - F_\Gamma w_\Gamma. \tag{2.9}$$

The differences of sign in W are due to the non-standard sign convention. This sign convention is used to allow for an easier interpretation of the results in the modified potential energy derivation. In the element discretization the sign convention can be changed to the standard convention for beams. The full derivation of the modified potential energy equation, its interpretation, and simplification, can be found in Appendix A. Important results are found in the interpretation of the Lagrange multipliers; C^0 moment continuity within the element is ensured when the function is varied to the rotation ϕ:

$$M|_{x_\Gamma^-} = M|_{x_\Gamma^+} = k_t(\phi_\Gamma^+ - \phi_\Gamma^-) = k_t \Delta\phi = M_\Gamma. \tag{2.10}$$

Furthermore, if no external force is applied on the fold, the moment field within the element becomes C^1-continuous:

$$\left.\frac{\partial M}{\partial x}\right|_{x_\Gamma^+} - \left.\frac{\partial M}{\partial x}\right|_{x_\Gamma^-} = F_\Gamma = 0. \tag{2.11}$$

If no force is applied on the fold, the derivative of the moment field is thus constant over the entire element, no weak moment field enrichment is needed, and standard linear shape functions can be used in the entire element.

Two final expressions for the modified potential energy are found, one derived with a force applied on the fold, and one derived without a force applied on the fold. Using a force applied on the fold, the final potential energy equation is:

$$\begin{aligned}\Pi = \int_0^{x_\Gamma^-} \left\{-\frac{1}{2EI}M^2 + \left(\frac{\partial^2 M}{\partial^2 x} - q(x)\right)w\right\} dx + [M\phi]_{x=0}^{x=x_\Gamma^-} + \frac{1}{2}k_t \Delta\phi^2 + \\ \left.\frac{\partial M}{\partial x}\right|_0 w_1 - \left.\frac{\partial M}{\partial x}\right|_L w_2 + w_\Gamma\left(\left.\frac{\partial M}{\partial x}\right|_{x_\Gamma^+} - \left.\frac{\partial M}{\partial x}\right|_{x_\Gamma^-}\right) + \\ \int_{x_\Gamma^+}^{L} \left\{-\frac{1}{2EI}M^2 + \left(\frac{\partial^2 M}{\partial^2 x} - q(x)\right)w\right\} dx + [M\phi]_{x_\Gamma^+}^{L} + W,\end{aligned} \tag{2.12}$$

where the displacement on the fold w_Γ is still present in the expression, since it is energetically coupled to the force on the fold. The two terms integrating the moment field over the two subdomains $\int_{\Omega_i} -\frac{1}{2EI}M^2 dx$, represent the bending energy in the beam. The term representing the bending energy in the fold is the same as the standard potential energy equation for springs: $\frac{1}{2}k_t \Delta\phi^2$. Lastly, the terms representing the potential energy of the reaction forces in the beam are found as: $[M\phi]_{x=0}^{x=x_\Gamma^-} + [M\phi]_{x_\Gamma^+}^{L} + \left.\frac{\partial M}{\partial x}\right|_0 w_1 - \left.\frac{\partial M}{\partial x}\right|_L w_2 + w_\Gamma\left(\left.\frac{\partial M}{\partial x}\right|_{x_\Gamma^+} - \left.\frac{\partial M}{\partial x}\right|_{x_\Gamma^-}\right)$.

When no external load is applied on the fold, the moment field becomes linear and the displacement on the fold (w_Γ) is removed from the expression, resulting in:

$$\begin{aligned}\Pi = \int_0^{x_\Gamma^-} \left\{-\frac{1}{2EI}M^2 + \left(\frac{\partial^2 M}{\partial^2 x} - q(x)\right)w\right\} dx + [M\phi]_{x=0}^{x=x_\Gamma^-} + \frac{1}{2}k_t \Delta\phi^2 + \left.\frac{\partial M}{\partial x}\right|_0 w_1 - \\ \left.\frac{\partial M}{\partial x}\right|_L w_2 + \int_{x_\Gamma^+}^{L} \left\{-\frac{1}{2EI}M^2 + \left(\frac{\partial^2 M}{\partial^2 x} - q(x)\right)w\right\} dx + [M\phi]_{x_\Gamma^+}^{L} + W,\end{aligned} \tag{2.13}$$

because the displacement on the fold is removed, one DOF less will be needed in the discretization. One term has not yet been discussed $\left(\frac{\partial^2 M}{\partial^2 x} - q(x)\right)w$, this term can be partially omitted because only linear functions for $M(x)$ are used, $\partial^2 M/\partial x^2 = 0$. The distributed load term $-q(x)w$, is also omitted in the discretization, and applied instead via an equivalent load vector in Appendix B.

2.2.2. 1D discretization

Two different stiffness matrices are derived; one using the modified potential energy as shown in Equation 2.12, resulting in the "6 DOF system", and one using the modified potential energy as shown in Equation 2.13, resulting in the "5 DOF system". In all cases the equation is discretized by evaluating three matrices: the $\boldsymbol{A}$-matrix, which contains the potential energy terms on the two subdomains; the $\boldsymbol{B}$-matrix, which contains the potential energy terms on the boundaries; and the $\boldsymbol{K}_t$-matrix containing the terms of the fold energy. In discretized form, the modified potential energy is written as:

$$\Pi = -\frac{1}{2}\mathbf{m}^{\mathsf{T}}\boldsymbol{A}\mathbf{m} - \mathbf{m}^{\mathsf{T}}\boldsymbol{B}\mathbf{u} + \frac{1}{2}\mathbf{u}^{\mathsf{T}}\boldsymbol{K}_t\mathbf{u} - \mathbf{f}^{\mathsf{T}}\mathbf{u}, \tag{2.14}$$

where $\mathbf{m}$ is a vector containing auxiliary DOFs concerning the moment field, $\mathbf{u}$ is a vector containing the displacement and rotation DOFs, and $\mathbf{f}$ is the vector containing the externally applied point loads. To transform the potential energy equation to a normal stiffness relation it is varied with respect to $\mathbf{m}$:

$$\partial\Pi = \frac{\partial\Pi}{\partial\mathbf{m}}\delta\mathbf{m} = \{-\boldsymbol{A}\mathbf{m} - \boldsymbol{B}\mathbf{u}\}\cdot\delta\mathbf{m} = 0. \tag{2.15}$$

The equation is rewritten to find an expression for $\mathbf{m}$, to allow the auxiliary DOFs to be removed,

$$\mathbf{m} = -\boldsymbol{A}^{-1}\boldsymbol{B}\mathbf{u}. \tag{2.16}$$

To formulate the stiffness matrix, the modified potential energy equation is varied with respect to $\mathbf{u}$,

$$\partial\Pi = \frac{\partial\Pi}{\partial\mathbf{u}}\delta\mathbf{u} = \{-\mathbf{m}^{\mathsf{T}}\boldsymbol{B} + \mathbf{u}^{\mathsf{T}}\boldsymbol{K}_t - \mathbf{f}^{\mathsf{T}}\}\delta\mathbf{u} = 0. \tag{2.17}$$

The expression for $\mathbf{m}$ is inserted, and making use in advance of the fact that $\boldsymbol{A}$ is a symmetric matrix, the equation is rewritten as:

$$(\boldsymbol{B}^{\mathsf{T}}\boldsymbol{A}^{-1}\boldsymbol{B} + \boldsymbol{K}_t^{\mathsf{T}})\mathbf{u} = \mathbf{f}, \tag{2.18}$$

resulting in the stiffness matrix:

$$\boldsymbol{K} = \boldsymbol{B}^{\mathsf{T}}\boldsymbol{A}^{-1}\boldsymbol{B} + \boldsymbol{K}_t^{\mathsf{T}}. \tag{2.19}$$

This formulation and Equation 2.19 holds for all elements derived in this thesis, with the difference being the details of the vectors $\boldsymbol{u}$ and $\boldsymbol{f}$, and the $\boldsymbol{A}$, $\boldsymbol{B}$,and $\boldsymbol{K}_t$ matrices.

Moving on to the formulations of the 5 and 6 DOF systems, the displacement vectors are defined as:

$$\begin{aligned} \mathbf{u}_6^{\mathsf{T}} &= [w_1,\ \phi_1,\ w_2,\ \phi_2,\ w_\Gamma,\ \Delta\phi] \text{ for 6 DOFs,} \\ \mathbf{u}_5^{\mathsf{T}} &= [w_1,\ \phi_1,\ w_2,\ \phi_2,\ \Delta\phi] \text{ for 5 DOFs,} \end{aligned} \tag{2.20}$$

where the rotation at the fold is simplified to a jump in rotation as: $\phi_\Gamma^+ - \phi_\Gamma^- = \Delta\phi$. The 5 and 6 DOF systems have similar definitions for the $\boldsymbol{A}$-matrix, but they differ in the auxiliary DOFs and shape functions used in the moment interpolation:

$$\begin{aligned} -\frac{1}{2}\mathbf{m}^{\intercal}\boldsymbol{A}\mathbf{m} &= -\int_{0}^{x_\Gamma^-}\frac{1}{2EI}M^2dx - \int_{x_\Gamma^+}^{L}\frac{1}{2EI}M^2dx = \mathbf{m}^{(6)T}\frac{1}{2k_b}\int_{0}^{L}\mathbf{N}^{(6)}\mathbf{N}^{(6)T}dx\mathbf{m}^{(6)} \text{ for 6 DOFs,} \\ -\frac{1}{2}\mathbf{m}^{\intercal}\boldsymbol{A}\mathbf{m} &= -\int_{0}^{x_\Gamma^-}\frac{1}{2EI}M^2dx - \int_{x_\Gamma^+}^{L}\frac{1}{2EI}M^2dx = \mathbf{m}^{(5)T}\frac{1}{2k_b}\int_{0}^{L}\mathbf{N}^{(5)}\mathbf{N}^{(5)T}dx\mathbf{m}^{(5)} \text{ for 5 DOFs,} \end{aligned} \tag{2.21}$$

where $\mathbf{N}^{(5,6)T}$ and $\mathbf{m}^{(5,6)T}$ are the shape functions and auxiliary DOFs for the 5 and 6 DOF system defined in Equations 2.26 and 2.27. The bending stiffness k_b of the beam is introduced as: $k_b = EI$, and is assumed to be constant throughout the entire beam. The $\boldsymbol{B}$-matrices are defined as:

$$\begin{aligned} -\mathbf{m}^{\intercal}\boldsymbol{B}\mathbf{u} &= [M\phi]_0^L - M\Delta\phi + \left.\frac{\partial M}{\partial x}\right|_0 w_1 - \left.\frac{\partial M}{\partial x}\right|_L w_2 + w_\Gamma\left(\left.\frac{\partial M}{\partial x}\right|_{x_\Gamma^+} - \left.\frac{\partial M}{\partial x}\right|_{x_\Gamma^-}\right) \text{ for 6 DOFs,} \\ -\mathbf{m}^{\intercal}\boldsymbol{B}\mathbf{u} &= [M\phi]_0^L - M\Delta\phi + \left.\frac{\partial M}{\partial x}\right|_0 w_1 - \left.\frac{\partial M}{\partial x}\right|_L w_2 \text{ for 5 DOFs,} \end{aligned} \tag{2.22}$$

and can be written down by hand using the appropriate shape functions and auxiliary DOFs. Finally, the $\boldsymbol{K}_t$-matrix and force vectors are defined as

$$\frac{1}{2}\mathbf{u}^{\intercal}\boldsymbol{K}_t\mathbf{u} = \frac{1}{2}k_t\Delta\phi^2, \tag{2.23}$$

$$-\mathbf{f}^{\intercal}\mathbf{u} = F_1w_1 + M_1\phi_1 - F_2w_2 - M_2\phi_2 - F_\Gamma w_\Gamma \text{ for 6 DOFs,} \tag{2.24}$$

$$-\mathbf{f}^{\intercal}\mathbf{u} = F_1w_1 + M_1\phi_1 - F_2w_2 - M_2\phi_2 \text{ for 5 DOFs.} \tag{2.25}$$

The stiffness matrices are calculated using the symbolic toolbox in MATLAB. As an interpolation field for the 6 DOF discretization, standard linear shape functions enriched with only a weak enrichment as found in [11] are used:

$$M^6(\xi) = N_1(\xi)M_1 + N_2(\xi)M_2 + \Psi(\xi)\alpha = (1-\xi)M_1 + \xi M_2 + \alpha\begin{cases} \frac{\xi}{\xi_\Gamma} & 0 \le \xi \le \xi_\Gamma \\ \frac{\xi-1}{\xi_\Gamma-1} & \xi_\Gamma \le \xi \le 1 \end{cases} = \mathbf{N}^{(6)\intercal}\mathbf{m}^{(6)}, \tag{2.26}$$

with the auxiliary DOFs, $\mathbf{m}^{(6)\intercal} = [M_1,\ M_2,\ \alpha]$, the generalized coordinate $\xi = x/L$, and the discontinuity at $\xi_\Gamma = x_\Gamma/L$. The enrichment function is defined such that it has a height of 1 at the fold, coupling the enriched DOF α to the moment added at the fold. In the 5 DOF discretization, only linear shape functions are used:

$$M^5(\xi) = N_1(\xi)M_1 + N_2(\xi)M_2 = (1-\xi)M_1 + \xi M_2 = \mathbf{N}^{(5)\intercal}\mathbf{m}^{(5)}, \tag{2.27}$$

with the auxiliary DOFs, $\mathbf{m}^{(5)\intercal} = [M_1,\ M_2]$.

The 6 DOF $\boldsymbol{B}$-matrix is found as:

$$\boldsymbol{B}^6 = \frac{1}{L}\begin{bmatrix} 1 & L & -1 & 0 & 0 & -L(\xi_\Gamma - 1) \\ -1 & 0 & 1 & -L & 0 & L\xi_\Gamma \\ -\frac{1}{\xi_\Gamma} & 0 & \frac{1}{\xi_\Gamma-1} & 0 & -\frac{1}{\xi_\Gamma^2-\xi_\Gamma} & L \end{bmatrix}, \tag{2.28}$$

and the 6 DOF $\boldsymbol{A}$-matrix is calculated in MATLAB as:

$$\boldsymbol{A}^6 = \frac{L}{3k_b}\begin{bmatrix} 1 & \frac{1}{2} & -\frac{\xi_\Gamma-2}{2} \\ \frac{1}{2} & 1 & \frac{\xi_\Gamma+1}{2} \\ -\frac{\xi_\Gamma-2}{2} & \frac{\xi_\Gamma+1}{2} & 1 \end{bmatrix}. \tag{2.29}$$

Note the symmetry in the $\boldsymbol{A}$-matrix, used in the stiffness matrix formulation, originating from the $\mathbf{NN}^{\mathsf{T}}$ term. The rotational stiffness matrix $\boldsymbol{K}_t$, is a 6×6 matrix consisting of mostly zeros, except for the diagonal value with its index equal to the index of $\Delta\phi$ in the displacement vector, which is equal to k_t. Using Equation 2.19, the 6 DOF stiffness matrix is calculated as:

$$\boldsymbol{K}^6 = k_b \cdot \begin{bmatrix} \frac{(3\xi_\Gamma+1)}{L^3\xi_\Gamma^3} & \frac{3(\xi_\Gamma+1)}{L^2\xi_\Gamma^2} & -\frac{9}{L^3\xi_\Gamma(\xi_\Gamma-1)} & \frac{3}{L^2\xi_\Gamma} & \frac{3(2\xi_\Gamma+1)}{L^3\xi_\Gamma^3(\xi_\Gamma-1)} & -\frac{6}{L^2\xi_\Gamma} \\ & \frac{(\xi_\Gamma+3)}{L\xi_\Gamma} & -\frac{3}{L^2(\xi_\Gamma-1)} & -\frac{1}{L} & \frac{3}{L^2\xi_\Gamma^2(\xi_\Gamma-1)} & -\frac{2}{L} \\ & & \frac{3(3\xi_\Gamma-4)}{L^3(\xi_\Gamma-1)^3} & \frac{3(\xi_\Gamma-2)}{L^2(\xi_\Gamma-1)^2} & -\frac{3(2\xi_\Gamma-3)}{L^3\xi_\Gamma(\xi_\Gamma-1)^3} & \frac{6}{L^2(\xi_\Gamma-1)} \\ & & \frac{(\xi_\Gamma-4)}{L(\xi_\Gamma-1)} & \frac{3}{L^2\xi_\Gamma(\xi_\Gamma-1)^2} & \frac{2}{L} & \\ & \mathit{symm.} & & & -\frac{3}{L^3\xi_\Gamma^3(\xi_\Gamma-1)^3} & -\frac{6}{L^2\xi_\Gamma(\xi_\Gamma-1)} \\ & & & & & \frac{4}{L} + \frac{k_t}{k_b} \end{bmatrix}. \tag{2.30}$$

Furthermore, the 5 DOF $\boldsymbol{B}$-matrix is found as:

$$\boldsymbol{B}^5 = \frac{1}{L}\begin{bmatrix} 1 & L & -1 & 0 & -L(\xi_\Gamma - 1) \\ -1 & 0 & 1 & -L & L\xi_\Gamma \end{bmatrix}, \tag{2.31}$$

and the 5 DOF $\boldsymbol{A}$-matrix is calculated in MATLAB as:

$$\boldsymbol{A}^5 = \frac{L}{3k_b}\begin{bmatrix} 1 & \frac{1}{2} \\ \frac{1}{2} & 1 \end{bmatrix}. \tag{2.32}$$

It can be seen that both $\boldsymbol{B}^5$ and $\boldsymbol{A}^5$ are submatrices of $\boldsymbol{B}^6$ and $\boldsymbol{A}^6$. Combining $\boldsymbol{B}^5$ and $\boldsymbol{A}^5$ and using a 5×5 $\boldsymbol{K}_t$ matrix, the 5 DOF stiffness matrix is found as:

$$\boldsymbol{K}^5 = k_b \cdot \begin{bmatrix} \frac{12}{L^3} & \frac{6}{L^2} & -\frac{12}{L^3} & \frac{6}{L^2} & -\frac{6(2\xi_\Gamma-1)}{L^2} \\ & \frac{4}{L} & -\frac{6}{L^2} & \frac{2}{L} & -\frac{2(3\xi_\Gamma-2)}{L} \\ & & \frac{12}{L^3} & -\frac{6}{L^2} & \frac{6(2\xi_\Gamma-1)}{L^2} \\ & \mathit{symm.} & & \frac{4}{L} & -\frac{2(3\xi_\Gamma-1)}{L} \\ & & & & \frac{4(3\xi_\Gamma^2-3\xi_\Gamma+1)}{L} + \frac{k_t}{k_b} \end{bmatrix}. \tag{2.33}$$

As can be seen $\boldsymbol{K}^5$ contains only terms bounded for $0 \le \xi_\Gamma \le 1$, and is a much simpler matrix than $\boldsymbol{K}^6$. Furthermore, $\boldsymbol{K}^6$ contains terms divided by ξ_Γ or $\xi_\Gamma - 1$, which are unbounded when the enriched node approximates standard nodes and $\xi_\Gamma \approx 0$ or $\xi_\Gamma \approx 1$. These unbounded terms are expected to cause ill-conditioning of the enriched stiffness matrix.

2.3. Numerical results and verification

Both the 5 and 6 DOF systems are verified using the test case in Figure 2.2, with the values as in Table 2.1. In Figure 2.2, a beam of length L, with a fold at x_Γ, and constant bending stiffness $E_1I_1 = E_2I_2 = k_b$ is clamped on its left side at $x = 0$, and loaded on its right side at $x = L$ with a force F. Only one folded beam element is used in the calculations. The right tip displacement w_2, is calculated for varying fold location $\xi_\Gamma = x_\Gamma/L$ and compared to the linearly exact solution:

k_b	k_t	F	L
100 N m^2	500 N m rad^{-1}	10 N	1 m

Table 2.1: Values used in the beam calculations, for the problem in Figure 2.2, with the analytical solution in Equation 2.34.

$$w_2 = \frac{FL^3}{3k_b} + \frac{FL^2(1-\xi_\Gamma)^2}{k_t}. \tag{2.34}$$

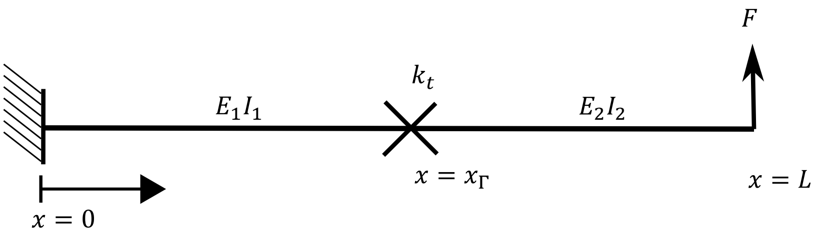

Figure 2.2: A beam of Length L, folded at $x = x_\Gamma$, clamped at $x = 0$ and loaded with a force F at $x = L$.

In Figure 2.3, the 5 and 6 DOF system are both found to be exact under this load case; this is due to the fact that under the applied force, the moment field within the beam is linear, and both the 5 and 6 DOF system use linear interpolations for the moment field.

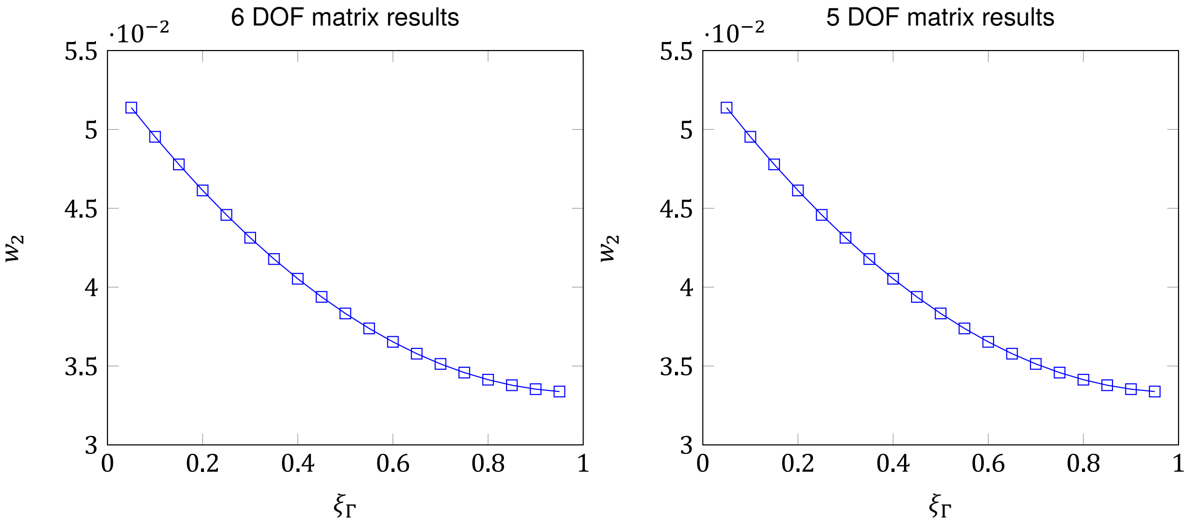

Figure 2.3: The right tip displacement w_2 of the beam in Figure 2.2, the results are calculated with the 5 and 6 DOF system and both are exact compared to the solution in Equation 2.34.

2.4. 1D matrix condition

As an indicator of stability of the solver and numerical accuracy, often the condition number of the stiffness matrix is computed as:

$$\chi = \frac{\lambda_{max}}{\lambda_{min}}, \tag{2.35}$$

where λ_{max} is the largest eigenvalue of the stiffness matrix and λ_{min} is the smallest non-zero eigenvalue. Modeling discontinuities using enriched formulations often causes ill-conditioning of the system matrices, characterized by large condition numbers. The condition number is calculated for the 5 and 6 DOF systems, and compared to a system of two hinged beam elements on a matching discretization. The hinged system is constructed by connecting two Euler beam elements, as found in [43]. One beam of length $L\xi_\Gamma$ with DOFs $\boldsymbol{u}^\intercal = [w_1,\ \phi_1,\ w_\Gamma,\ \phi_\Gamma^-]$, and another beam of length $L(1-\xi_\Gamma)$ with DOFs $\boldsymbol{u}^\intercal = [w_\Gamma,\ \phi_\Gamma^+,\ w_2,\ \phi_2]$, are connected via a hinge element with stiffness matrix:

$$\boldsymbol{K}_h\boldsymbol{u} = k_t \begin{bmatrix} 1 & -1 \\ -1 & 1 \end{bmatrix} \begin{bmatrix} \phi_\Gamma^- \\ \phi_\Gamma^+ \end{bmatrix}. \tag{2.36}$$

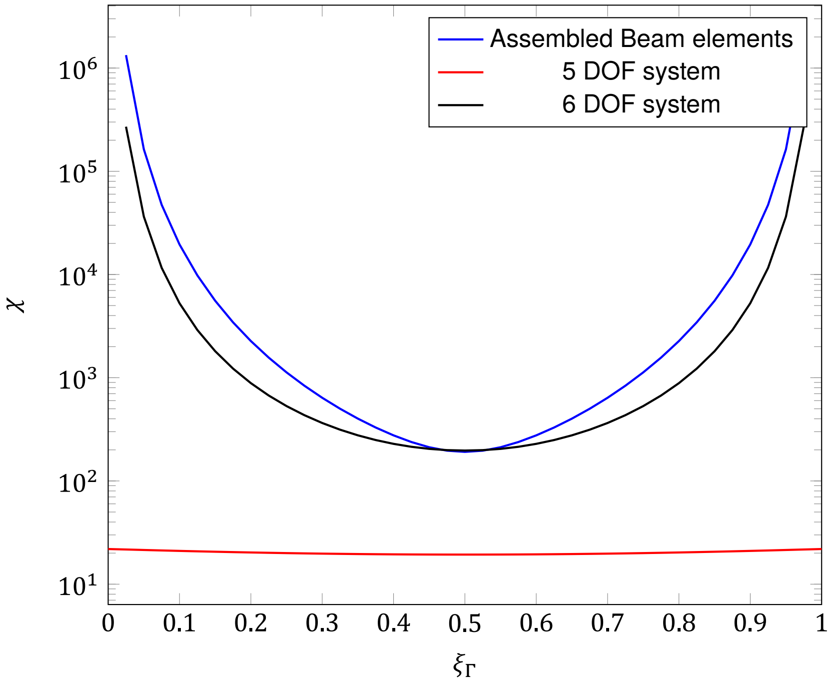

Figure 2.4: The matrix condition of the assembled folded beam element and the 5 and 6 DOF system, calculated using the parameters in Table 2.1.

The hinged beam element simulates the case when local re-meshing is applied to a beam element to account for an arbitrary fold placement. Assembling the two beam elements and the hinge element, a system is formulated containing the 7 DOFs: w_1, ϕ_1, ϕ_Γ^-, w_Γ, ϕ_Γ^+, w_2, ϕ_2. The matrix condition of the 5 and 6 DOF system can be found in Figure 2.4, the 5 DOF system performs very well with a condition number of $\chi \approx 20$. Furthermore its condition number is bounded and has a maximum value of $\chi = 21.9$ at $\xi_\Gamma = 0$ and $\xi_\Gamma = 1$. The 6 DOF system does not achieve bounded condition numbers, and performs slightly better than the assembled system when the fold location is not around $\xi_\Gamma = 0.5$, and worse when the fold is at $\xi_\Gamma = 0.5$.

Following standard procedure in IGFEM [11] to improve the condition number of the 6 DOF system, a scaling parameter s is introduced as:

$$M^6(\xi) = (1-\xi)M_1 + \xi M_2 + s \cdot \alpha \begin{cases} \frac{\xi}{\xi_\Gamma} & 0 \leq \xi \leq \xi_\Gamma \\ \frac{\xi - 1}{\xi_\Gamma - 1} & \xi_\Gamma \leq \xi \leq 1 \end{cases} . \tag{2.37}$$

Because a mixed/hybrid element formulation is used, the introduction of the scaling parameter in this manner has no effect on the final stiffness matrix, as explained in Appendix C. Another method of introducing a scaling parameter, is by inserting it directly into the displacement vector as: $\mathbf{u}^\intercal = [w_1,\ \phi_1,\ w_2,\ \phi_2,\ s_w \cdot w_\Gamma,\ s_\phi \cdot \Delta\phi]$. This method is also investigated in Appendix C, and although it improves the condition numbers of the 6 DOF system, it does not lead to the drastic improvements needed to attain similar condition numbers as the 5 DOF system. A common method of improving condition numbers, is by using a precondition matrix. The condition number of the 6 DOF system is improved by using a jacobi preconditioner of the form:

$$\boldsymbol{K}' = \boldsymbol{PKP}, \tag{2.38}$$

where the precondition matrix is defined as:

$$P_{ij} = \frac{\delta_{ij}}{\sqrt{K_{ij}}}, \tag{2.39}$$

and no scaling parameter is used. The matrix condition numbers can be found for a beam with zero fold stiffness in Figure 2.5a, and for a beam with a fold stiffness of $k_t = 500$ in Figure

2.5b. The condition number of the preconditioned 6 DOF system is drastically improved, and decreased slightly below the 5 DOF system condition number for low k_t.

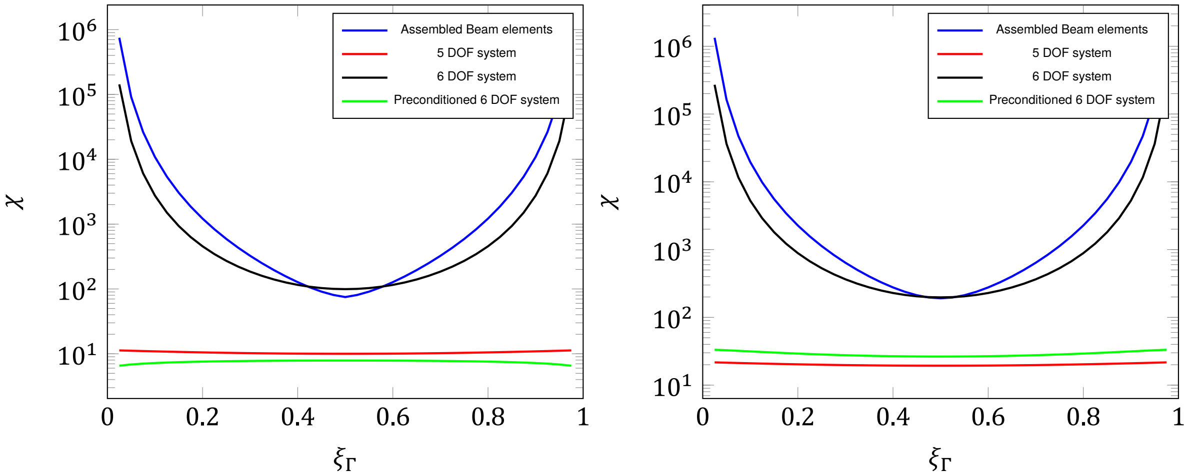

(a) Condition numbers χ, calculated using a fold stiffness of $k_t = 0$

(b) Condition numbers χ, calculated using a fold stiffness of $k_t = 500$

Figure 2.5: The matrix condition for assembled, 5 DOF, 6 DOF, and preconditioned 6 DOF systems for varying the fold location ξ_Γ, calculated for one element constructed using the material parameters in Table 2.1.

The 5 DOF system has the exceptional property of a condition number which does not grow to infinity, for discontinuities located at the boundaries; $\xi_\Gamma = 0$ and $\xi_\Gamma = 1$. Furthermore, for these discontinuities, the 5 DOF system still achieves analytically exact solutions. Using a preconditioner on the 6 DOF system drastically improves the condition number, but the condition number does not become bounded. For discontinuities at $\xi_\Gamma = 0$ and $\xi_\Gamma = 1$, the 6 DOF stiffness matrix has elements which grow to infinity, and the preconditioner can not be applied to improve condition number.

2.5. Condensed foldable beam element

The number of DOFs in the 5 DOF system can be decreased one final time, resulting in a foldable beam element with the exact same DOFs as a non-foldable beam element, and thus no enriched DOFs. In Appendix D, the 5 DOF system is condensed using the static condensation algorithm as described in [44]. Another way of condensing the system, in line with the mixed/hybrid element formulation, can be defined. By splitting the displacement vector into the standard beam element displacement vector $\boldsymbol{u}^4 = [w_1,\ \phi_1,\ w_2,\ \phi_2]$, and the jump in rotation $\Delta\phi$, the discretization can be changed to:

$$\Pi = -\frac{1}{2}\mathbf{m}^\intercal \boldsymbol{A}\mathbf{m} - \mathbf{m}^\intercal \boldsymbol{B}_S \mathbf{u}^4 - \mathbf{m}^\intercal \boldsymbol{B}_E \Delta\phi + \frac{1}{2}\Delta\phi k_t \Delta\phi - \mathbf{f}^\intercal \mathbf{u}^4, \tag{2.40}$$

where the $\boldsymbol{B}$-matrix as defined for the 5 DOF system is split into the 2×4 $\boldsymbol{B}_S$-matrix, connected to the DOFs in $\boldsymbol{u}^4$, and the 2×1 $\boldsymbol{B}_E$-matrix, connected to $\Delta\phi$, as $\boldsymbol{B}^5 = [\boldsymbol{B}_S,\ \boldsymbol{B}_E]$. Using similar steps as in the discretization in Section 2.2.2, the potential energy is firstly varied with respect to $\Delta\phi$:

$$\frac{\partial\Pi}{\partial\Delta\phi}\delta\Delta\phi = \left(-\boldsymbol{m}^\intercal \boldsymbol{B}_E + k_t\Delta\phi\right)\delta\Delta\phi = 0, \tag{2.41}$$

and rewritten to find an expression for $\Delta\phi$:

$$\Delta\phi = k_t^{-1}\boldsymbol{B}_E^\intercal \boldsymbol{m}. \tag{2.42}$$

The next step is to find an expression for $\boldsymbol{m}$, and to substitute the expression for $\Delta\phi$ in this equation to remove the enriched DOF from the discretized potential energy equation. This is done by varying with respect to $\boldsymbol{m}$:

$$\frac{\partial\Pi}{\partial\boldsymbol{m}}\delta\boldsymbol{m} = \left(-\boldsymbol{A}\boldsymbol{m} - \boldsymbol{B}_S\boldsymbol{u}^4 - \boldsymbol{B}_E\Delta\phi\right)\cdot\delta\boldsymbol{m} = \left(-\boldsymbol{A}\boldsymbol{m} - \boldsymbol{B}_S\boldsymbol{u}^4 - \boldsymbol{B}_E k_t^{-1}\boldsymbol{B}_E^\intercal\boldsymbol{m}\right)\cdot\delta\boldsymbol{m} = 0, \tag{2.43}$$

and rewriting to find an expression for $\boldsymbol{m}$:

$$\boldsymbol{m} = -(\boldsymbol{A} + \boldsymbol{B}_E k_t^{-1} \boldsymbol{B}_E^{\intercal})^{-1} \boldsymbol{B}_S \boldsymbol{u}^4. \tag{2.44}$$

To find the condensed stiffness matrix, the potential energy equation is varied with respect to $\boldsymbol{u}^4$, and the expression for $\boldsymbol{m}$ is substituted as:

$$\frac{\partial \Pi}{\partial \boldsymbol{u}^4} \delta \boldsymbol{u}^4 = \left(-\boldsymbol{m}^{\intercal} \boldsymbol{B}_S - \boldsymbol{f}^{\intercal}\right) \delta \boldsymbol{u}^4 = \left(\boldsymbol{B}_S^{\intercal} (\boldsymbol{A} + \boldsymbol{B}_E k_t^{-1} \boldsymbol{B}_E^{\intercal})^{-1} \boldsymbol{B}_S \boldsymbol{u}^4 - \boldsymbol{f}\right) \cdot \delta \boldsymbol{u}^4 = 0, \tag{2.45}$$

resulting in the condensed stiffness matrix:

$$\boldsymbol{K}^{(c)} = \boldsymbol{B}_S^{\intercal} (\boldsymbol{A} + \boldsymbol{B}_E k_t^{-1} \boldsymbol{B}_E^{\intercal})^{-1} \boldsymbol{B}_S = \boldsymbol{B}_S^{\intercal} \boldsymbol{A}_c^{-1} \boldsymbol{B}_S. \tag{2.46}$$

In Equation 2.46, all terms concerning the potential energy due to the fold (k_t^{-1}, $\boldsymbol{B}_E$) are now part of the newly formed $\boldsymbol{A}_c$-matrix. The $\boldsymbol{A}$-matrix generally contains the bending energy in the beam. The folding energy thus becomes part of the internal deformation energy in the beam, instead of the energy due to the reaction forces, contained in the $\boldsymbol{B}$-matrix. Furthermore, the condensed stiffness matrix derivation can be seen as a continuation of the mixed/hybrid method, where $\Delta\phi$ is used as an auxiliary, instead of a primary DOF.

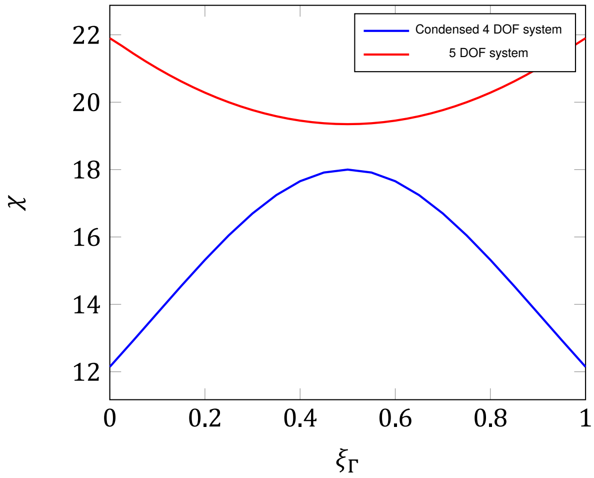

Figure 2.6: The condition numbers of the 5 DOF and condensed 4 DOF elements for varying fold location ξ_Γ, calculated using the material parameters in Table 2.1.

The condensed formulation for the 4 DOF folded beam stiffness matrix is tested using the test case in Section 2.3, and achieves the same exact results as the 5 and 6 DOF formulations. More interesting is the condition number of the condensed folded beam, as Found in Figure 2.6. The condition number of $\boldsymbol{K}^{(c)}$, has decreased with respect to the condition number of $\boldsymbol{K}^{(5)}$, and remains bounded for $0 \leq \xi_\Gamma \leq 1$.

2.6. Discussion

Two methods for deriving a foldable element have been used; the 6 DOF derivation, which implements a weak enrichment in the moment field, and the 5 DOF derivation, which uses no enrichment function. Both systems achieve the same level of numerical accuracy. The disadvantage of the 5 DOF system is the fact that a force cannot be straightforwardly implemented on the fold, whereas using the 6 DOF system this can be easily done. To compensate for this fact, a method is derived to implement a force on the fold for the 5 DOF system in Appendix B. The force is applied on the fold via a work equivalent load vector, derived using the applied moment interpolations and relations between moment, curvature, rotation, and displacement.

The matrix condition numbers of both formulations are compared. In the 6 DOF system, the condition numbers are unbounded for folds approximating standard element nodes, while the condition numbers of the 5 DOF system remain fairly constant and are bounded. The condition numbers of the 6 DOF system can be drastically improved by using a precondition matrix. Even though the preconditioned 6 DOF system achieves a well-conditioned stiffness matrix, it still requires some post-processing to calculate the element DOFs, and the preconditioner can not be applied for folds located at standard element nodes. The 5 DOF system and preconditioned 6 DOF system attain similar condition numbers, but the 5 DOF system is preferred since it is easier to implement, uses less DOFs, and requires no post-processing. Condensing the 5 DOF system improves the matrix condition even further, and may reduce computational time as less DOFs are needed to model a problem.

The increase in condition number of the 6 DOF system for folds approximating standard nodes, can be explained by investigating the displacement DOFs w_Γ and w_i, of the fold and standard node respectively. When a fold approximates a standard node these DOFs should become equal $w_\Gamma = w_i$, and the stiffness matrix becomes linear with respect to these DOFs. The 6 DOF system condition numbers can be slightly improved by introducing an optimized scaling factor for the enriched DOFs, as shown in Appendix C. The optimal scaling factor can be interpreted as defining an enrichment, such that it has a constant jump in derivative at the fold. Introducing a moment field enrichment, defined by a constant jump in derivative at the fold, connects the enrichment to the force at the fold: $F_\Gamma = \frac{\partial M}{\partial x}|_{x_\Gamma^+} - \frac{\partial M}{\partial x}|_{x_\Gamma^-}$, which is energetically conjugate to w_Γ. The changed definition also forces the enrichment function to tend to zero near the standard node locations, removing some of the linearity's in the system. Although the condition numbers of the 6 DOF system are improved by introducing the scaling function, they remains worse than the 5 DOF system condition numbers.

3

Foldable Plate

Advancing on the procedure developed for a foldable beam, several foldable plate elements will be derived. In the foldable beam formulation, a C^1-continuous moment field lead to improved condition numbers, relative to a C^0-continuous moment field. For this reason, no load will be applied on the fold, resulting in a C^1-continuous moment field in the plate, that does not require an enrichment. Although no moment field enrichment will be required, enrichment functions will be defined for the rotation and displacement on the element boundary. As found in the scaled moment enrichment for the 6 DOF beam in Equation C.11, and suggested in [33], the discontinuous rotational field will be implemented by introducing a discontinuity directly in the derivative of the displacement field.

Based on three different standard plate elements, six foldable elements will be derived. Besides four foldable elements containing enriched DOFs, two foldable elements containing only standard DOFs will be derived by condensing the elements locally. Since condition numbers of the condensed beam in Section 2.5 were improved, it is expected that condition numbers will be improved by condensing the plate elements. The foldable elements are based on three standard elements: the $KL0$ and $KL1$ elements [39] (a constant moment, and a linear moment plate element), and the HSM element [37] (another linear moment plate element). The $KL0$ element will be enriched using either one or two enriched DOFs, the $KL1$ and HSM elements will both be enriched using two enriched DOFs. As explained in Chapter 1, the difference between the $KL1$ and HSM elements is the location and number of DOFs: the HSM element uses only 9 DOFs, 1 displacement and 2 rotations at each node, whereas the $KL1$ element uses 12 DOFs, 1 displacement at each node, one displacement at each side, and 2 rotations at each side.

3.1. 2D problem definition

In Figure 3.1, an arbitrarily shaped plate domain Ω in the $x-y$ plane, with closed boundary $\Gamma = \overline{\Omega} \setminus \Omega$, is depicted. An out of plane displacement field, $w(x,y)$, and an in plane rotational vector field, $\boldsymbol{\phi}(x,y)$, are defined on the plate. Because different kinematic and constitutive equations hold on the domain and fold line, the domain Ω is divided into two subdomains and a fold line:

$$\begin{aligned} &\Omega = \Omega_1 \cup \Omega_2 \cup \Gamma_F, && \text{such that,} \\ &\Omega_1 \cap \Omega_2 = \emptyset, && \text{and,} \\ &\overline{\Omega}_1 \cap \overline{\Omega}_2 = \Gamma_F. \end{aligned} \tag{3.1}$$

The subdomain Ω_1 (Ω_2) has a closed boundary Γ_1 (Γ_2), where the subdomain boundaries are defined as:

$$\begin{aligned} &\Gamma_i = \overline{\Omega}_i \setminus \Omega_i,\ i = 1,2, \quad \text{such that,} \\ &\Gamma_i = \Gamma_i' + \Gamma_F^i, \\ &\Gamma_1' + \Gamma_2' = \Gamma, \\ &\Gamma_F^1 = \Gamma_F^2 = \Gamma_F. \end{aligned} \tag{3.2}$$

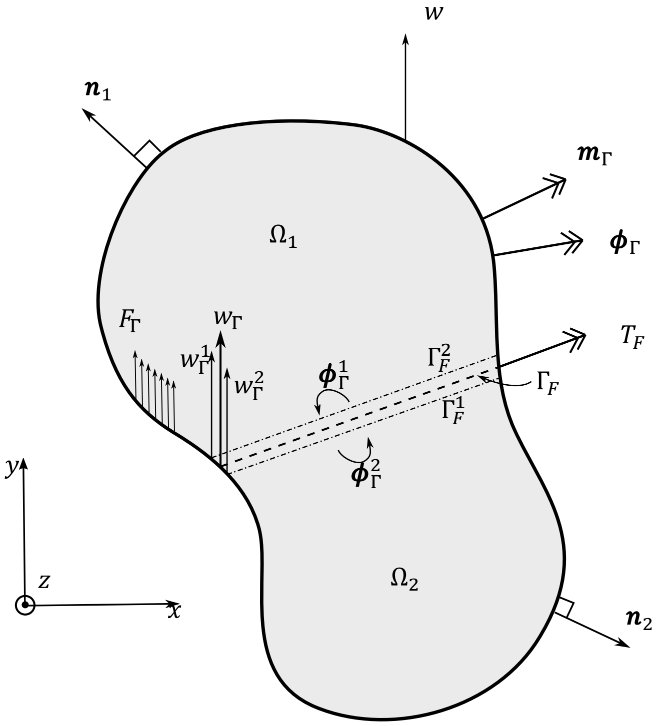

Figure 3.1: A foldable plate element located in the $x-y$-plane with a displacement field in the z-direction $w(x,y)$, and a rotation field in the $x-y$-plane $\boldsymbol{\phi}(x,y)$. It is loaded on the boundary Γ by a distributed force in z direction, $F_\Gamma(x,y)$, and a distributed moment vector in the $x-y$-plane, $\boldsymbol{m}_\Gamma(x,y)$.

Three fold lines (Γ_F^1, Γ_F^2, and Γ_F) are defined because approaching the fold from either Ω_1 or Ω_2, different values for the rotation are defined. A short notation for functions approaching the fold line from either side is defined:

$$\lim_{\boldsymbol{r}\to\Gamma_F^i} f(\boldsymbol{r}) = f_\Gamma^i,\ i = 1,2 \tag{3.3}$$

The plate is loaded on the boundary Γ by a distributed force in the z direction $F_\Gamma(x,y)$, and a distributed moment in the $x-y$ plane $\boldsymbol{m}_\Gamma(x,y)$. On the plate domain Ω, a distributed load is applied $q(x,y)$. Furthermore, the outward normal, $\boldsymbol{n}_1$, $\boldsymbol{n}_2$, and $\boldsymbol{n}$ of Ω_1, Ω_2, and Ω respectively, are related by:

$$\begin{aligned} \boldsymbol{n}_1 &= -\boldsymbol{n}_2 \text{ on } \Gamma_F, \\ \boldsymbol{n}_1 &= \boldsymbol{n} \text{ on } \Gamma_1', \\ \boldsymbol{n}_2 &= \boldsymbol{n} \text{ on } \Gamma_2', \end{aligned} \tag{3.4}$$

On the two subdomains, standard kinematic equations for the rotation and the curvature of the plate are used:

$$\begin{aligned} \boldsymbol{\phi}(\boldsymbol{r}) &= \nabla w(\boldsymbol{r}) \text{ on } \Omega_1 \cup \Omega_2, \\ \boldsymbol{C}(\boldsymbol{r}) &= \nabla \boldsymbol{\phi}(\boldsymbol{r}) \text{ on } \Omega_1 \cup \Omega_2, \end{aligned} \tag{3.5}$$

where the curvature $\boldsymbol{C}$, is a symmetric 2×2 matrix which can be written in vector form:

$$\boldsymbol{\kappa}^\intercal = [C_{11},\ C_{22},\ 2C_{12}]. \tag{3.6}$$

On the fold line, standard kinematic relations do not hold, as the rotation is discontinuous. To ensure a C^0-continuous displacement field at the fold, we define:

$$w_\Gamma^1 = w_\Gamma^2 = w_\Gamma \text{ on } \Gamma_F. \tag{3.7}$$

Although it is possible to implement different material parameters on the subdomains created by the fold, it is chosen to use constant parameters for simplicity, and because origami structures are often made from one piece of sheet material. Standard linearly elastic material properties are assumed as:

$$\begin{aligned} \boldsymbol{m} &= \boldsymbol{D}\boldsymbol{\kappa} \quad \text{on } \Omega_1 \cup \Omega_2, \\ \boldsymbol{M} &= \boldsymbol{\mathcal{D}}\boldsymbol{C} \quad \text{on } \Omega_1 \cup \Omega_2, \end{aligned} \tag{3.8}$$

where $\boldsymbol{m}$ is the moment vector derived from the 2×2 symmetric moment matrix $\boldsymbol{M}$ as:

$$\boldsymbol{m}^\mathrm{T} = [M_{11},\ M_{22},\ M_{12}]. \tag{3.9}$$

The constitutive matrix $\boldsymbol{D}$, is defined on Ω_i as:

$$\boldsymbol{D} = \frac{Et^3}{12(1-\nu^2)} \begin{bmatrix} 1 & \nu & 0 \\ \nu & 1 & 0 \\ 0 & 0 & \frac{1-\nu}{2} \end{bmatrix}, \tag{3.10}$$

and its counterpart, the fourth order stiffness tensor $\boldsymbol{\mathcal{D}}$, is defined on Ω_i as:

$$\mathcal{D}_{ijkl} = \frac{t^3}{12}\left(\mu\left(\delta_{ij}\delta_{jl} + \delta_{il}\delta_{jk}\right) + \frac{2\lambda\mu}{\lambda + 2\mu}\delta_{ij}\delta_{kl}\right) \quad \text{where,} \tag{3.11}$$

$$\lambda = \frac{\nu E}{(1+\nu)\,(1-2\nu)}, \tag{3.12}$$

$$\mu = \frac{E}{2\,(1+\nu)}, \tag{3.13}$$

where E denotes the Young's modulus, t the plate thickness, ν the Poisson's ratio, and δ_{ij} the Kronecker delta function. In the modified potential energy derivation, the fold is modeled as a torsional spring relating rotations and moments in the 2D $x - y$ plane:

$$\boldsymbol{T}_F = \int_{\Gamma_F} \boldsymbol{K}_T(\boldsymbol{\phi}_\Gamma^1 - \boldsymbol{\phi}_\Gamma^2)dS_F = \int_{\Gamma_F} \boldsymbol{K}_T \Delta\boldsymbol{\phi} dS_F \text{ on } \Gamma_F, \tag{3.14}$$

where $\boldsymbol{K}_T$ is a 2×2 torsional stiffness matrix, which will be simplified and specified in the element discretization.

3.2. 2D modified potential energy derivation

The modified potential energy derivation for a foldable plate, is similar to the modified potential energy derivation for a foldable beam. The full modified potential energy derivation can be found in Appendix E; only the important results are discussed in this section. The modified potential energy term for a deformed foldable plate, with its kinematic relations enforced by Lagrange multipliers ($\boldsymbol{\lambda}_1$, $\boldsymbol{\Lambda}_2$, $\boldsymbol{\lambda}_3$, $\boldsymbol{\Lambda}_4$, λ_5, and λ_6), is expressed as:

$$\begin{aligned} \Pi = &\int_{\Omega_i} \left\{ \frac{1}{2}\boldsymbol{\kappa}^\mathrm{T}\boldsymbol{D}\boldsymbol{\kappa} + \boldsymbol{\lambda}_{1,3}\cdot(\boldsymbol{\phi} - \nabla w) + \boldsymbol{\Lambda}_{2,4} : (\boldsymbol{C} - \nabla\boldsymbol{\phi}) - qw \right\} dA_i + \\ &\int_{\Gamma_F} \left\{ \frac{1}{2}\Delta\boldsymbol{\phi}^\mathrm{T}\boldsymbol{K}_T\Delta\boldsymbol{\phi} + \lambda_5(w_\Gamma^1 - w_\Gamma) + \lambda_6(w_\Gamma - w_\Gamma^2) \right\} dS_F - \int_\Gamma [F_\Gamma w + \boldsymbol{m}_\Gamma\boldsymbol{\phi}_\Gamma] dS. \end{aligned} \tag{3.15}$$

By not including an externally applied force on the fold, a C^1-continuous moment field interpolation can be used in the elements, as in the derivation of the modified potential energy equation it is found that:

$$m\boldsymbol{n} = \boldsymbol{m}_\Gamma \text{ on } \Gamma, \tag{3.16}$$

$$(\nabla\cdot\boldsymbol{M}_\Gamma^1)\cdot\boldsymbol{n}_1 = -(\nabla\cdot\boldsymbol{M}_\Gamma^2)\cdot\boldsymbol{n}_2 = (\nabla\cdot\boldsymbol{M}_\Gamma^2)\cdot\boldsymbol{n}_1 \text{ on } \Gamma_F, \tag{3.17}$$

where the relation between $\boldsymbol{n}_1$ and $\boldsymbol{n}_2$ is inserted. Using integration by parts, the modified potential energy equation is simplified, and surface integrals containing the displacement and rotation are transformed into boundary integrals:

$$\Pi = -\int_{\Omega_i} \frac{1}{2}\boldsymbol{m}^{\mathsf{T}}\boldsymbol{D}^{-1}\boldsymbol{m}\,dA_i - \int_{\Gamma} \left\{w \cdot (\nabla \cdot \boldsymbol{M}) \cdot \boldsymbol{n}_{1,2} - \boldsymbol{\phi} \cdot \boldsymbol{M}\boldsymbol{n}\right\} dS + \int_{\Gamma_F} \left\{\frac{1}{2}\Delta\boldsymbol{\phi}^{\mathsf{T}}\boldsymbol{K}_T\Delta\boldsymbol{\phi} + \Delta\boldsymbol{\phi} \cdot \boldsymbol{M}\boldsymbol{n}_1\right\} dS_F - \int_{\Gamma} [F_{\Gamma} w + \boldsymbol{m}_{\Gamma}\boldsymbol{\phi}_{\Gamma}] dS - \int_{\Omega} qw\,dA. \tag{3.18}$$

3.3. 2D discretization

3.3.1. Discretized matrix definitions

As can be seen in the modified potential energy function in Equation 3.18, interpolation functions for the displacement and rotational field at the boundaries are needed in the discretization. In addition, enrichment functions need to be defined for boundaries intersected by the fold. Firstly, the modified potential energy equation is discretized, using the same formulation as the discretized modified potential energy equation of the beam:

$$\Pi = -\frac{1}{2}\boldsymbol{\beta}^{\mathsf{T}}\boldsymbol{A}\boldsymbol{\beta} - \boldsymbol{\beta}^{\mathsf{T}}\boldsymbol{B}\boldsymbol{u} + \frac{1}{2}\boldsymbol{u}^{\mathsf{T}}\boldsymbol{K}_F\boldsymbol{u} - \boldsymbol{f}^{\mathsf{T}}\boldsymbol{u}, \tag{3.19}$$

where the auxiliary DOFs $\boldsymbol{\beta}$, are related to the moment field interpolation in the plate, and the $\boldsymbol{A}$-matrix is defined:

$$-\frac{1}{2}\boldsymbol{\beta}^{\mathsf{T}}\boldsymbol{A}\boldsymbol{\beta} = -\int_{\Omega_i} \frac{1}{2}\boldsymbol{m}^{\mathsf{T}}\boldsymbol{D}^{-1}\boldsymbol{m}\,dA_i = -\int_{\Omega} \frac{1}{2}\boldsymbol{m}^{\mathsf{T}}\boldsymbol{D}^{-1}\boldsymbol{m}\,dA. \tag{3.20}$$

Constant material parameters are assumed throughout the entire element, which simplifies the two integrals over Ω_i, to one integral over Ω. The $\boldsymbol{B}$-matrix is defined by an integral over the element boundary Γ, and the fold line Γ_F:

$$-\boldsymbol{\beta}^{\mathsf{T}}\boldsymbol{B}\boldsymbol{u} = -\int_{\Gamma} \{w \cdot (\nabla \cdot \boldsymbol{M}) \cdot \boldsymbol{n} - \boldsymbol{\phi} \cdot \boldsymbol{M}\boldsymbol{n}\}\, dS + \int_{\Gamma_F} \Delta\boldsymbol{\phi} \cdot \boldsymbol{M}\boldsymbol{n}_1 dS_F, \tag{3.21}$$

Additionally, the $\boldsymbol{B}$-matrix is split into two parts as: $\boldsymbol{B} = [\boldsymbol{B}_S, \boldsymbol{B}_E]$, where the standard $\boldsymbol{B}$-matrix ($\boldsymbol{B}_S$) and enriched $\boldsymbol{B}$-matrix ($\boldsymbol{B}_E$) are defined:

$$\boldsymbol{\beta}^{\mathsf{T}}\boldsymbol{B}\boldsymbol{u} = \boldsymbol{\beta}^{\mathsf{T}}\boldsymbol{B}_S\boldsymbol{u}_S + \boldsymbol{\beta}^{\mathsf{T}}\boldsymbol{B}_E\boldsymbol{u}_E \tag{3.22}$$

$$-\boldsymbol{\beta}^{\mathsf{T}}\boldsymbol{B}_S\boldsymbol{u}_S = -\int_{\Gamma} \left\{w_S \cdot (\nabla \cdot \boldsymbol{M}) \cdot \boldsymbol{n}_{1,2} - \boldsymbol{\phi}_S \cdot \boldsymbol{M}\boldsymbol{n}\right\} dS, \tag{3.23}$$

$$-\boldsymbol{\beta}^{\mathsf{T}}\boldsymbol{B}_E\boldsymbol{u}_E = -\int_{\Gamma} \left\{w_E \cdot (\nabla \cdot \boldsymbol{M}) \cdot \boldsymbol{n}_{1,2} - \boldsymbol{\phi}_E \cdot \boldsymbol{M}\boldsymbol{n}\right\} dS + \int_{\Gamma_F} \Delta\boldsymbol{\phi} \cdot \boldsymbol{M}\boldsymbol{n}_1 dS_F. \tag{3.24}$$

The displacement vector $\boldsymbol{u}$ is split into a part containing only standard DOFs $\boldsymbol{u}_S$, and a part containing only enriched DOFs $\boldsymbol{u}_E$ as: $\boldsymbol{u}^{\mathsf{T}} = \left[\boldsymbol{u}_S^{\mathsf{T}}, \boldsymbol{u}_E^{\mathsf{T}}\right]$. Furthermore, w_S and $\boldsymbol{\phi}_S$ are the displacement and rotation due to the standard element interpolations only, w_E and $\boldsymbol{\phi}_E$ are the displacement and rotation due to an enriched interpolation function, and $\Delta\boldsymbol{\phi}$ is the jump in rotation at the fold Γ_F. The torsional stiffness matrix is defined using:

$$\frac{1}{2}\boldsymbol{u}_E^{\mathsf{T}}\boldsymbol{K}_t\boldsymbol{u}_E = \int_{\Gamma_F} \frac{1}{2}\Delta\boldsymbol{\phi}^{\mathsf{T}}\boldsymbol{K}_T\Delta\boldsymbol{\phi}\,dS_F, \tag{3.25}$$

where $\boldsymbol{K}_F$ as found in Equation 3.19, is defined as a matrix with the same size as the final stiffness matrix $\boldsymbol{K}$, containing mostly zeros, and with $\boldsymbol{K}_t$ assembled in the lower right corner:

$$\boldsymbol{K}_F = \begin{bmatrix} \emptyset & \emptyset \\ \emptyset & \boldsymbol{K}_t \end{bmatrix}. \tag{3.26}$$

Finally, a work equivalent load vector $\boldsymbol{f}$, is defined using:

$$-\boldsymbol{f}^{\intercal}\boldsymbol{u} = -\int_{\Gamma}[F_{\Gamma}w + \boldsymbol{m}_{\Gamma}\boldsymbol{\phi}_{\Gamma}]dS - \int_{\Omega} qwdA, \tag{3.27}$$

where interpolation functions for w and ϕ at Γ, will be introduced in the discretization, allowing for a numerical evaluation of $\int_{\Gamma}[F_{\Gamma}w+\boldsymbol{m}_{\Gamma}\boldsymbol{\phi}_{\Gamma}]dS$, to defined $\boldsymbol{f}$. No interpolation functions for the displacement field $w(x,y)$ on Ω will be introduced, making the derivation of an equivalent load vector for a pressure q cumbersome.

Following the same procedure as in Section 2.2.2, the final stiffness matrix is defined as

$$\boxed{\boldsymbol{K} = \boldsymbol{B}^{\intercal}\boldsymbol{A}^{-1}\boldsymbol{B} + \boldsymbol{K}_{F}.} \tag{3.28}$$

Furthermore, to define the two condensed plate elements, the modified potential energy equation is discretized as:

$$\Pi = -\frac{1}{2}\boldsymbol{\beta}^{\intercal}\boldsymbol{A}\boldsymbol{\beta} - \boldsymbol{\beta}^{\intercal}\boldsymbol{B}_{S}\boldsymbol{u} - \boldsymbol{\beta}^{\intercal}\boldsymbol{B}_{E}\boldsymbol{u}_{E} + \frac{1}{2}\boldsymbol{u}_{E}^{\intercal}\boldsymbol{K}_{t}\boldsymbol{u}_{E} - \boldsymbol{f}^{\intercal}\boldsymbol{u}, \tag{3.29}$$

and following the procedure as in Section 2.5, this will result in the condensed stiffness matrix:

$$\boxed{\boldsymbol{K}^{(c)} = \boldsymbol{B}_{S}^{\intercal}(\boldsymbol{A} + \boldsymbol{B}_{E}\boldsymbol{K}_{t}^{-1}\boldsymbol{B}_{E}^{\intercal})^{-1}\boldsymbol{B}_{S}} \tag{3.30}$$

3.3.2. Triangular element parameterization

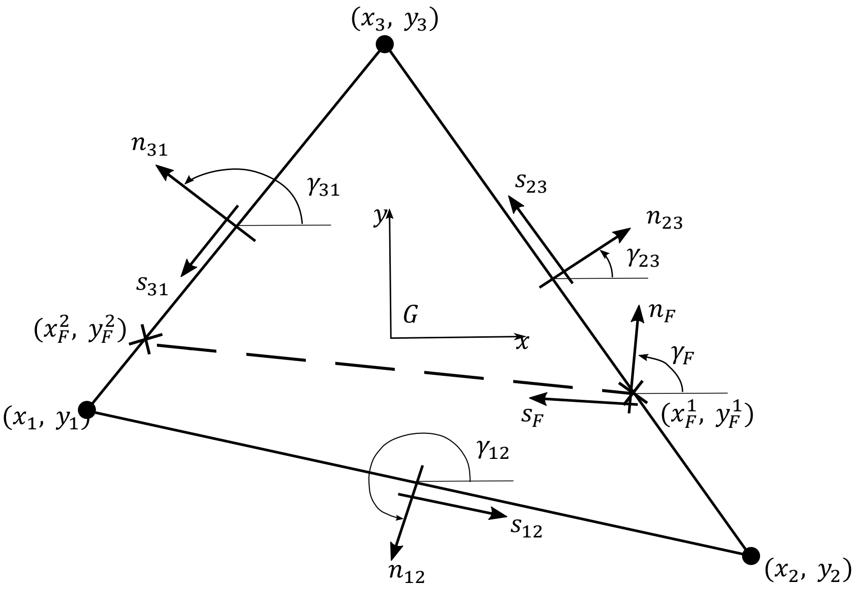

Figure 3.2: The folded reference triangle, with a coordinate system located at its centroid. Besides the standard corner nodes (depicted as dots) two enriched nodes (depicted as cross) are added at the intersection of the fold (the dashed line) and element boundary.

In Figure 3.2, a general triangular element is defined, with the origin of the local coordinate system at its centroid. For each of the three element sides and the fold line, the cosine and sine (C_{ij}, S_{ij}, C_F, and S_F) of the angle between the outward normal $\boldsymbol{n}$, and the x-axis are calculated:

$$C_{ij} = \cos(\gamma_{ij}) = \frac{\Delta y_{ij}}{l_{ij}}, \tag{3.31}$$

$$S_{ij} = \sin(\gamma_{ij}) = -\frac{\Delta x_{ij}}{l_{ij}}, \tag{3.32}$$

$$C_F = \cos(\gamma_F) = \frac{\Delta y_F}{l_F}, \tag{3.33}$$

$$S_F = \sin(\gamma_F) = -\frac{\Delta x_F}{l_F}, \tag{3.34}$$

where:

$$\Delta x_{ij} = x_j - x_i \text{ and } \Delta y_{ij} = y_j - y_i, \tag{3.35}$$

$$\Delta x_F = x_F^2 - x_F^1 \text{ and } \Delta y_F = y_F^2 - y_F^1, \tag{3.36}$$

$$\tag{3.37}$$

and the lengths of the element sides and the fold line are defined as:

$$l_{ij} = \sqrt{\Delta x_{ij}^2 + \Delta y_{ij}^2}, \tag{3.38}$$

$$l_F = \sqrt{\Delta x_F^2 + \Delta y_F^2}. \tag{3.39}$$

$$\tag{3.40}$$

Additionally, the surface area of the element S_a, is calculated:

$$a = \frac{l_{12} + l_{23} + L_{31}}{2}, \tag{3.41}$$

$$S_a = \sqrt{a(a - l_{12})(a - l_{22})(a - l_{31})}. \tag{3.42}$$

Following [37], the cosine and sine are denoted without their subscripts as C and S, respectively. Furthermore, the location of the enriched node on a folded edge s_Γ^i is calculated as:

$$\Delta x_{ij}^\Gamma = x_F^k - x(s_{ij} = 0) \text{ and } \Delta y_{ij}^\Gamma = y_F^k - y(s_{ij} = 0), \tag{3.43}$$

$$s_\Gamma^i = \sqrt{{\Delta x_{ij}^\Gamma}^2 + {\Delta y_{ij}^\Gamma}^2} \text{ for } i, j \in \{1, 2, 3\}. \tag{3.44}$$

Finally, using Figure 3.3, the outward normal $\boldsymbol{n}$, and a transformation between global and local rotations are defined:

$$\boldsymbol{n}^\intercal = \begin{bmatrix} C & S \end{bmatrix} \tag{3.45}$$

$$\boldsymbol{\phi} = \begin{bmatrix} w_{,x} \\ w_{,y} \end{bmatrix} = \begin{bmatrix} C & -S \\ S & C \end{bmatrix} \begin{bmatrix} w_{,n} \\ w_{,s} \end{bmatrix} \tag{3.46}$$

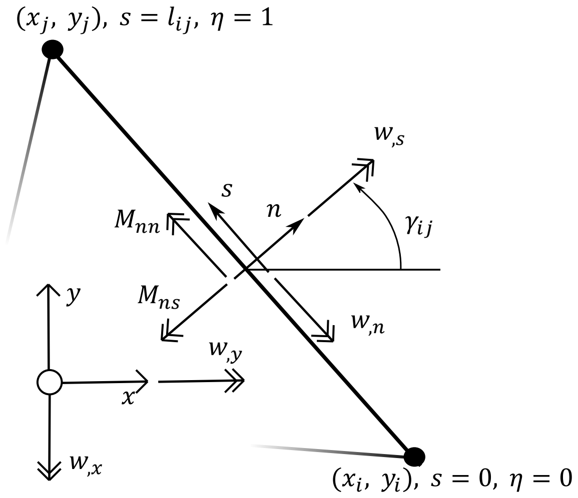

Figure 3.3: One of the three element edges defined in the global coordinate system (x, y) with local edge coordinate s and generalized edge coordinate $\eta = \frac{s}{l_{ij}}$. Each boundary has two local rotations $w_{,n}$ and $w_{,s}$ energetically conjugate to two local reaction moments M_{nn} and M_{ns} respectively.

3.3.3. General B-matrix definition

The main differences between standard and foldable plate elements are contained in the $\boldsymbol{B}$-matrix. For this reason the general $\boldsymbol{B}$-matrix definition requires some extra attention, before particular foldable elements are derived. As explained in Section 3.3.1, the $\boldsymbol{B}$-matrix is split into an enriched and non-enriched part as: $\boldsymbol{B} = [\boldsymbol{B}_S,\ \boldsymbol{B}_E]$.The standard $\boldsymbol{B}$-matrix ($\boldsymbol{B}_S$ is equal to the non folded $\boldsymbol{B}$-matrices in [37, 39]. This matrix is related to the energy consumed by the reaction forces at the element boundaries, and is defined:

$$\begin{aligned}
-\boldsymbol{\beta}^{\mathsf{T}}\boldsymbol{B}_S\boldsymbol{u} &= -\int_\Gamma \{w_S \cdot (\nabla \cdot \boldsymbol{M}) \cdot \boldsymbol{n} - \boldsymbol{\phi}_S \cdot \boldsymbol{M}\boldsymbol{n}\}\, ds \\
&= -\int_\Gamma \left\{ w_S \cdot \begin{bmatrix} \boldsymbol{M}_{xx,x} + \boldsymbol{M}_{xy,x} \\ \boldsymbol{M}_{yy,y} + \boldsymbol{M}_{yx,y} \end{bmatrix} \cdot \begin{bmatrix} C \\ S \end{bmatrix} - \begin{bmatrix} C & -S \\ S & C \end{bmatrix} \begin{bmatrix} w_{S,n} \\ w_{S,s} \end{bmatrix} \cdot \begin{bmatrix} \boldsymbol{M}_{xx} & \boldsymbol{M}_{xy} \\ \boldsymbol{M}_{yx} & \boldsymbol{M}_{yy} \end{bmatrix} \begin{bmatrix} C \\ S \end{bmatrix} \right\} ds \\
&= -\int_\Gamma \left\{ w_S Q_n - w_{,n} M_{nn} - w_{,s} M_{ns} \right\} ds. \qquad (3.47)
\end{aligned}$$

The rotations of an element edge as shown in Figure 3.3, are defined as derivatives of the displacement field, $\phi_n = \partial w/\partial n = w_{,n}$ and $\phi_s = \partial w/\partial s = w_{,s}$. The terms concerning the moment field are simplified to distributed reaction forces and moments defined on the boundary in Figure 3.3 as:

$$Q_n = C(\boldsymbol{M}_{xx,x} + \boldsymbol{M}_{xy,y}) + S(\boldsymbol{M}_{yy,y} + \boldsymbol{M}_{xy,x}), \qquad (3.48)$$

$$M_{nn} = CC\boldsymbol{M}_{xx} + 2CS\boldsymbol{M}_{xy} + SS\boldsymbol{M}_{yy}, \qquad (3.49)$$

$$M_{ns} = -SC\boldsymbol{M}_{xx} + (CC - SS)\boldsymbol{M}_{xy} + SC\boldsymbol{M}_{yy}. \qquad (3.50)$$

Because triangular elements have three straight boundary segments, the standard $\boldsymbol{B}$-matrix is defined by the three sub-matrices $\boldsymbol{B}_{12}$, $\boldsymbol{B}_{23}$, and $\boldsymbol{B}_{31}$, corresponding to each of the three element edges. The sub-matrices $\boldsymbol{B}_{ij}$ can be assembled to form the matrix $\boldsymbol{B}_S$. To define the sub-matrices, Equations 3.48 to 3.50 are written in vector format and gathered in $\boldsymbol{R}_{ij}$, and the standard element shape functions are assembled in $\boldsymbol{L}_{ij}$, as:

$$\begin{bmatrix} Q_n \\ -M_{nn} \\ -M_{ns} \end{bmatrix} = \boldsymbol{R}_{ij}(s)\boldsymbol{\beta}, \tag{3.51}$$

$$\begin{bmatrix} w_S \\ w_{S,n} \\ w_{S,s} \end{bmatrix} = \boldsymbol{L}_{ij}(s)\boldsymbol{u}_{ij}, \tag{3.52}$$

where $\boldsymbol{u}_{ij}$ is a vector containing the standard DOFs attached to the element edge connecting corner nodes i and j. To discretize Equation 3.47, the generalized coordinate $\eta = s/l_{ij}$ is used, and the sub-matrices are defined:

$$\boxed{\boldsymbol{B}_{ij} = l_{ij} \int_0^1 \boldsymbol{R}_{ij}(\eta)^\intercal \boldsymbol{L}_{ij}(\eta) d\eta.} \tag{3.53}$$

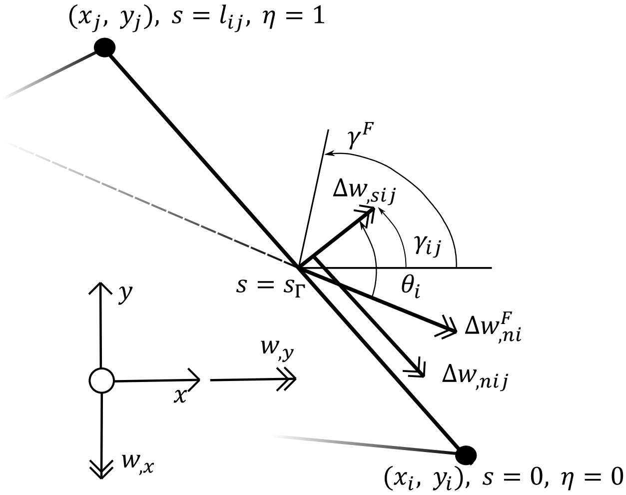

Figure 3.4: A folded boundary of an element, where the jump in rotation along the fold line ($\Delta w^F_{,n}$) is projected on the edge local coordinate system as two jumps in rotation ($\Delta w_{,n}$ and $\Delta w_{,s}$). Expressed in the edge coordinate s, the intersection between element edge and fold line is located at $s = s_\Gamma$.

Besides the standard $\boldsymbol{B}$-matrix, the enriched $\boldsymbol{B}$-matrix ($\boldsymbol{B}_E$) is derived, defined in Equation 3.24 as:

$$\begin{aligned}
-\boldsymbol{\beta}^\intercal \boldsymbol{B}_E \boldsymbol{u} &= -\int_\Gamma \left\{ w_E \cdot (\nabla \cdot \boldsymbol{M}) \cdot \boldsymbol{n}_{1,2} - \boldsymbol{\phi}_E \cdot \boldsymbol{M}\boldsymbol{n} \right\} ds + \int_{\Gamma_F} \Delta\boldsymbol{\phi} \cdot \boldsymbol{M}\boldsymbol{n}_1 ds_F \\
&= -\int_\Gamma \left\{ w_E Q_n - w_{E,n} M_{nn} - w_{E,s} M_{ns} \right\} ds + \int_{\Gamma_F} \begin{bmatrix} C & -S \\ S & C \end{bmatrix} \begin{bmatrix} w^1_{,n} - w^2_{,n} \\ w^1_{,s} - w^2_{,s} \end{bmatrix} \cdot \begin{bmatrix} \boldsymbol{M}_{xx} & \boldsymbol{M}_{xy} \\ \boldsymbol{M}_{yx} & \boldsymbol{M}_{yy} \end{bmatrix} \begin{bmatrix} C \\ S \end{bmatrix} ds_F \\
&= -\int_\Gamma \left\{ w_E Q_n - w_{E,n} M_{nn} - w_{E,s} M_{ns} \right\} ds + \int_{\Gamma_F} \left\{ (w^1_{,n} - w^2_{,n}) M^F_{nn} + (w^1_{,s} - w^2_{,s}) M^F_{ns} \right\} ds_F \\
&= -\int_\Gamma \left\{ w_E Q_n - w_{E,n} M_{nn} - w_{E,s} M_{ns} \right\} ds - \int_{\Gamma_F} \Delta w^F_{,n} M^F_{nn} ds_F,
\end{aligned} \tag{3.54}$$

where the first part in $-\boldsymbol{\beta}^\intercal \boldsymbol{B}_E \boldsymbol{u}$ is defined using only enrichment functions (w_E). Furthermore Q_n, M_{nn}, and M_{ns} are the same terms as used in the $\boldsymbol{B}_S$ definition, found in Equations 3.48 to 3.50. If a jump in rotation perpendicular to the fold would exist, a strong discontinuity would be introduced as: $w^1_\Gamma - w^2_\Gamma = \Delta w = \Delta w_{,s} ds$, hence this jump in rotation is assumed to be zero, $\Delta w_{,s} = 0$. The jump in rotation is thus simplified to a jump in rotation along the fold line only, $\Delta w^F_{,n}$ as shown in Figure 3.4, this jump in rotation is energetically conjugated to a moment along the fold:

$$M^F_{nn} = C_F C_F \boldsymbol{M}_{xx} + 2C_F S_F \boldsymbol{M}_{xy} + S_F S_F \boldsymbol{M}_{yy}. \tag{3.55}$$

Furthermore, the jump in rotation is defined as a valley fold: $\Delta w_{,n} = w^2_{,n} - w^1_{,n}$, causing the change in sign before $\int_{\Gamma_F} \Delta w^F_{,n} M^F_{nn} ds_F$. Using the simplified jump in rotation, the 2D relation between jump in rotation and moment along the fold,

$$\boldsymbol{T}_F = \int_{\Gamma_F} \boldsymbol{K}_T(\boldsymbol{\phi}^1_\Gamma - \boldsymbol{\phi}^2_\Gamma) dS_F = \int_{\Gamma_F} \boldsymbol{K}_T \Delta\boldsymbol{\phi} dS_F, \tag{3.56}$$

can be simplified to a 1D relation:

$$T_F = \int_{\Gamma_F} k_t(w^2_{,n} - w^1_{,n}) dS_F = \int_{\Gamma_F} k_t \Delta w_{,n} dS_F, \tag{3.57}$$

where k_t is the torsional stiffness per unit length of the fold, and T_F the moment along the fold line.

In the fold local coordinate system (s_F, n_F), two enriched DOFs are defined, as shown in Figure 3.5. Since, in Equation 3.54, the first integral to define $\boldsymbol{B}_E$ is evaluated in the edge local coordinate system (s, n), a transformation between (s_F, n_F) and (s, n) is needed. To transform the jump in rotation, $\Delta w^F_{,ni}$ to the edge local coordinate system, the angle θ_i from $\Delta w^F_{,ni}$ to $\Delta w_{,sij}$ as shown in Figure 3.4 is defined as:

$$\theta_i = \frac{\pi}{2} + \gamma_{ij} - \gamma_F. \tag{3.58}$$

The transformation of the jump in rotation is consequently defined as:

$$\begin{bmatrix} \Delta w_{,nij} \\ \Delta w_{,sij} \end{bmatrix} = \begin{bmatrix} \sin(\theta_i) \\ \cos(\theta_i) \end{bmatrix} \Delta w^F_{,ni}, \tag{3.59}$$

where the cosine and sine are defined as:

$$\cos(\theta_i) = \cos(\frac{\pi}{2} + \gamma_{ij} - \gamma_F) = S_F C_{ij} - C_F S_{ij} = C_{\theta i}, \tag{3.60}$$

$$\sin(\theta_i) = \sin(\frac{\pi}{2} + \gamma_{ij} - \gamma_F) = C_F C_{ij} + S_F S_{ij} = S_{\theta i}. \tag{3.61}$$

Since a positive jump in rotation corresponds to a valley fold, the vectors representing the jump in rotation will point outward of the element, as shown in Figure 3.5. This definition causes the calculated angle θ'_i at the second enriched node (θ'_3 in Figure 3.5), to be rotated by π radians with respect to θ_i as: $\theta_3 = \theta'_3 - \pi$. To compensate for this fact the transformation at the second enriched node (where $s_F = l_F$) is multiplied by -1 as:

$$\begin{bmatrix} \Delta w_{,nij} \\ \Delta w_{,sij} \end{bmatrix} = \begin{bmatrix} -S_{\theta i} \\ -C_{\theta i} \end{bmatrix} \Delta w^F_{,ni}, \tag{3.62}$$

where Equations 3.60 and 3.61 are used to calculate $C_{\theta i}$ and $S_{\theta i}$.

The displacement field of an edge intersected by the fold is enriched with a weak enrichment function $\Psi(\eta)$, and the rotation field with its derivative $\Psi(\eta)_{,s}$ as:

$$w(\eta) = w_S + w_E = \boldsymbol{N}_w(\eta)\boldsymbol{u}_{ij} + \Psi(\eta)\Delta w_{,sij}, \tag{3.63}$$

$$w_{,n}(\eta) = w_{S,n} + w_{E,n} = \boldsymbol{N}_{\phi_n}(\eta)\boldsymbol{u}_{ij} + \Psi_{,s}(\eta)\Delta w_{,nij}, \tag{3.64}$$

$$w_{,s}(\eta) = w_{S,s} + w_{E,s} = \boldsymbol{N}_{w,s}(\eta)\boldsymbol{u}_{ij} + \Psi_{,s}(\eta)\Delta w_{,sij}, \tag{3.65}$$

The standard interpolation functions $\boldsymbol{N}_w(\eta)$, $\boldsymbol{N}_{w,s}(\eta)$, and $\boldsymbol{N}_{\phi_n}$, are used only in the standard $\boldsymbol{B}$-matrix formulation in Equation 3.47, and not in the enriched $\boldsymbol{B}$-matrix formulation. In the

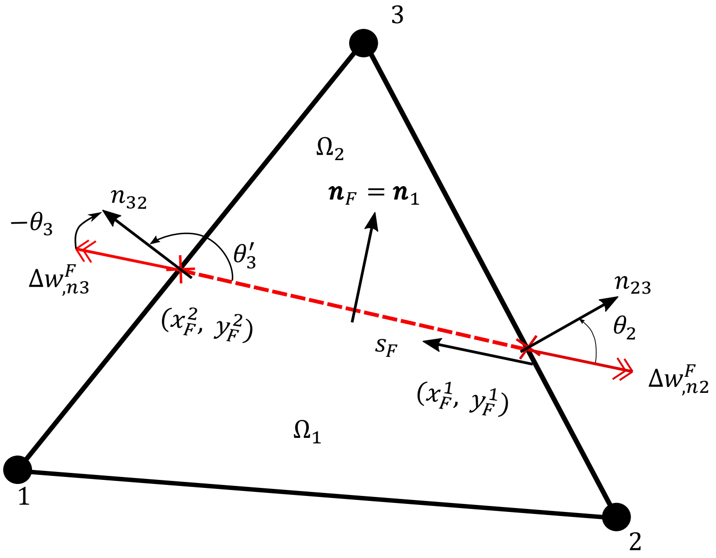

Figure 3.5: An arbitrary triangular plate element with two enriched DOFs representing a jump in rotation added. Since the enriched DOFs represent a valley fold, and integration over the boundary is performed counterclockwise, the vector representing the enriched DOF will always be pointing outward of the element.

enriched $\boldsymbol{B}$-matrix definition, only the weak enrichment of the displacement field is used:

$$w_E(\eta) = \Psi(\eta)\Delta w_{,sij} = \Psi(\eta)\Delta w^F_{,ni} C_{\theta i}, \tag{3.66}$$

$$w_{E,n}(\eta) = \Psi_{,s}(\eta)\Delta w_{,nij} = \Psi_{,\eta}(\eta)\frac{\Delta w^F_{,ni} S_{\theta i}}{l_{ij}}, \tag{3.67}$$

$$w_{E,s}(\eta) = \Psi_{,s}(\eta)\Delta w_{,sij} = \Psi_{,\eta}(\eta)\frac{\Delta w^F_{,ni} C_{\theta i}}{l_{ij}}, \tag{3.68}$$

The further derivation of the enriched $\boldsymbol{B}$-matrix is similar to the standard $\boldsymbol{B}$-matrix derivation. Reaction forces and moments at the boundaries (Q_n, M_{nn}, M_{ns}) are discretized as in Equation 3.51, using $\boldsymbol{R}_{ij}$, and the enriched displacements and its derivatives are discretized in $\boldsymbol{L}^F_{ij}$ as:

$$\begin{bmatrix} w_E \\ w_{E,n} \\ w_{E,s} \end{bmatrix} = \begin{bmatrix} C_{\theta i}\Psi(\eta) \\ \frac{S_{\theta i}\Psi(\eta)_{,\eta}}{l_{ij}} \\ \frac{C_{\theta i}\Psi(\eta)_{,\eta}}{l_{ij}} \end{bmatrix} \Delta w^F_{,ni} = \boldsymbol{L}^F_{ij}\Delta w^F_{,ni}. \tag{3.69}$$

Using these definitions, the enriched $\boldsymbol{B}$-matrix is derived by formulating and assembling three sub-matrices; two matrices related to the enrichments on the element edges $\boldsymbol{B}^i_E$, and one matrix related to an integral over the fold line $\boldsymbol{B}^F_E$. Firstly, the two sub-matrices for the two element edges intersected by the fold are defined. This corresponds to the first part of the enriched $\boldsymbol{B}$-matrix definition in Equation 3.54:

$$\boldsymbol{\beta}^{\mathsf{T}}\boldsymbol{B}^i_E\ \Delta w^F_{,ni} = \int_\Gamma \{w_E Q_n - w_{E,n}M_{nn} - w_{E,s}M_{ns}\}\, ds = \boldsymbol{\beta}^{\mathsf{T}} l_{ij}\int_0^1 \boldsymbol{R}_{ij}(\eta)^{\mathsf{T}}\boldsymbol{L}^F_{ij}(\eta)d\eta\ \Delta w^F_{,ni}, \tag{3.70}$$

resulting in:

$$\boxed{\boldsymbol{B}^i_E = l_{ij}\int_0^1 \boldsymbol{R}_{ij}(\eta)^{\mathsf{T}}\boldsymbol{L}^F_{ij}(\eta)d\eta.} \tag{3.71}$$

The second part of the enriched $\boldsymbol{B}$-matrix definition is constructed from an integral over the fold line. An interpolation for the jump in rotation is introduced as:

$$\Delta w^F_{,n}(\eta) = \boldsymbol{N}_{\Delta\phi}(\eta)\boldsymbol{u}_E, \tag{3.72}$$

where $\boldsymbol{u}_E^\intercal = [\Delta w_{,ni}^F,\ \Delta w_{,nj}^F]$, and a generalized fold coordinate is introduced as $\eta = s_F/l_F$. Furthermore, a transformation from $\boldsymbol{\beta}$ to M_{nn}^F is introduced as:

$$M_{nn}^F = \boldsymbol{R}_F\,(\eta)\,\boldsymbol{\beta}, \tag{3.73}$$

where the relation in Equation 3.55 is represented by $\boldsymbol{R}_F\,(\eta)$. Using these matrices, the second part of the enriched $\boldsymbol{B}$-matrix is defined:

$$\boldsymbol{\beta}^\intercal\boldsymbol{B}_E^F\ \ \boldsymbol{u}_E = \int_{\Gamma_F} \Delta w_{,n}^F M_{nn}^F ds_F = \boldsymbol{\beta}^\intercal l_F \int_0^1 \boldsymbol{R}_F^\intercal\,(\eta)\,\boldsymbol{N}_{\Delta\phi}(\eta) d\eta\ \boldsymbol{u}_E, \tag{3.74}$$

resulting in:

$$\boxed{\boldsymbol{B}_E^F = l_F \int_0^1 \boldsymbol{R}_F^\intercal\,(\eta)\,\boldsymbol{N}_{\Delta\phi}(\eta) d\eta.} \tag{3.75}$$

Consequently, the enriched $\boldsymbol{B}$-matrix ($\boldsymbol{B}_E$) for a foldable element is constructed by assembling the sub-matrices as:

$$\boldsymbol{B}_E = \begin{bmatrix}\boldsymbol{B}_E^i & \boldsymbol{B}_E^j\end{bmatrix} + \boldsymbol{B}_E^F, \tag{3.76}$$

where $\boldsymbol{B}_E^i$ and $\boldsymbol{B}_E^j$ are connected to $\Delta w_{,ni}^F$ and $\Delta w_{,nj}^F$ respectively, and $\boldsymbol{B}_E^F$ is connected to both enriched DOFs. The final $\boldsymbol{B}$-matrix is constructed by combining $\boldsymbol{B}_E$ and $\boldsymbol{B}_S$ as:

$$\boldsymbol{B} = [\boldsymbol{B}_S,\ \boldsymbol{B}_E]. \tag{3.77}$$

Additionally, the work equivalent load vector for a distributed load applied on one element edge, can be defined using the edge displacement interpolations in Equations 3.52 and 3.69. Inserting these displacement definitions in Equation 3.27, we attain:

$$\boldsymbol{f}^\intercal\boldsymbol{u} = \int_\Gamma [F_\Gamma w + \boldsymbol{m}_\Gamma\boldsymbol{\phi}_\Gamma] dS = \int_0^{l_{ij}} \left\{\begin{bmatrix}F_\Gamma & \boldsymbol{m}_\Gamma^\intercal\end{bmatrix}\boldsymbol{L}_{ij}\boldsymbol{u}_{ij} + \begin{bmatrix}F_\Gamma & \boldsymbol{m}_\Gamma^\intercal\end{bmatrix}\boldsymbol{L}_{ij}^F\Delta w_{,ni}^F\right\} ds_{ij}, \tag{3.78}$$

where $\boldsymbol{m}_\Gamma$ are the distributed edge moments, defined in the edge local coordinate system $\boldsymbol{m}_\Gamma^\intercal = [m_{\Gamma nn},\ m_{\Gamma ns}]$, and F_Γ the distributed edge force. Furthermore, the integral is evaluated numerically, and the second term within the integral is only used when a load is applied on one of the enriched edges.

3.3.4. KL0 element enriched with one DOF

In this section, a one DOF enriched foldable $KL0$ element (the $KL0^{(1)}$-element) will be derived. As shown in Figure 3.6, the element has only one enriched DOF, which will result in a constant jump in rotation over the entire fold line. Using Figures 3.4 and 3.5, we have explained how the jumps in rotation ($\Delta w_{,ni}^F$ and $\Delta w_{,nj}^F$) can be projected on the element edges. To project the single jump in rotation on the element edges, we assume: $\Delta w_{,n}^F = \Delta w_{,ni}^F = \Delta w_{,nj}^F$.

Firstly, the $\boldsymbol{A}$-matrix, related to the bending energy of the plate, is derived following [39]. The $\boldsymbol{A}$-matrix does not differ for the foldable and non foldable elements, because the same moment interpolation field can be used in the foldable and non-foldable elements. A constant moment matrix $\boldsymbol{A}_c$, is defined by the shape function:

$$\boldsymbol{m} = I\boldsymbol{\beta}_3, \tag{3.79}$$

where I is a 3×3 identity matrix, $\boldsymbol{m}$ the moment vector, and $\boldsymbol{\beta}_3$ the vector containing the auxiliary DOFs. In the constant moment plate elements, the auxiliary DOFs are thus exactly equal to the moment vector of the plate. Using Equation 3.20, the constant moment $\boldsymbol{A}$-matrix is defined by:

$$-\frac{1}{2}\boldsymbol{\beta}_3^\intercal\boldsymbol{A}_c\boldsymbol{\beta}_3 = -\frac{1}{2}\int_\Omega \boldsymbol{m}^\intercal\boldsymbol{D}^{-1}\boldsymbol{m} dA = -\frac{1}{2}\boldsymbol{\beta}_3^\intercal\int_\Omega \boldsymbol{D}^{-1} dA\boldsymbol{\beta}_3, \tag{3.80}$$

resulting in:

$$\boxed{\boldsymbol{A}_c = S_a\boldsymbol{D}^{-1} \text{ and } \boldsymbol{A}_c^{-1} = \frac{1}{S_a}\boldsymbol{D}.} \tag{3.81}$$

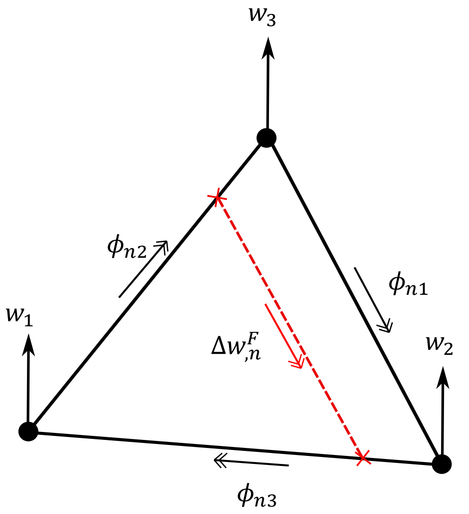

Figure 3.6: The one DOF enriched KL0 element ($KL0^{(1)}$-element). On the fold line, one enriched DOF is added, represented by the red arrow $\Delta w_{,n}$.

In the $KL0^{(1)}$-element, the standard $\boldsymbol{B}$-matrix is denoted $\boldsymbol{B}_{KL0}$, and the enriched $\boldsymbol{B}$-matrix is denoted $\boldsymbol{B}_c^{F(1)}$. Because a constant moment field is used, derivatives of the moment field are zero, resulting in no internal reaction forces at the boundary: $Q_n = 0$. This causes the term wQ_n to drop from the $\boldsymbol{B}$-matrix definition. The transformation between $\boldsymbol{\beta}_3$ and $[M_{nn}, M_{ns}]$ is defined as:

$$\begin{bmatrix} -M_{nn} \\ -M_{ns} \end{bmatrix} = \begin{bmatrix} -CC & -SS & -2CS \\ CS & -CS & -(CC-SS) \end{bmatrix} \boldsymbol{\beta}_3 = \boldsymbol{R}^c_{ij} \boldsymbol{\beta}_3, \tag{3.82}$$

and on the three element edges, a linear interpolation field is used for the displacement:

$$w(\eta) = \begin{bmatrix} 1-\eta & \eta \end{bmatrix} \begin{bmatrix} w_i \\ w_j \end{bmatrix}. \tag{3.83}$$

The rotation perpendicular to the edge is defined as the derivative of the edge displacement:

$$w_{,s} = \frac{1}{l} w_{,\eta}(\eta) = \frac{1}{l} \begin{bmatrix} -1 & 1 \end{bmatrix} \begin{bmatrix} w_i \\ w_j \end{bmatrix}. \tag{3.84}$$

Furthermore, no interpolation function for the rotation along the edge is needed, because it is assumed to be constant, and since wQ_n dropped from the equations, the displacement w does not need to be included in the $\boldsymbol{L}_{ij}$ matrix formulation:

$$\begin{bmatrix} w_{,n} \\ w_{,s} \end{bmatrix} = \begin{bmatrix} 0 & 1 & 0 \\ -\frac{1}{l} & 0 & \frac{1}{l} \end{bmatrix} \begin{bmatrix} w_i \\ \phi_{nk} \\ w_j \end{bmatrix} = \boldsymbol{L}^0_{ij} \boldsymbol{u}_{ij}. \tag{3.85}$$

Combining these matrices using Equation 3.53, results in:

$$\boxed{\boldsymbol{B}^{KL0}_{ij} = l_{ij} \int_0^1 \boldsymbol{R}^{c\,\intercal}_{ij} \boldsymbol{L}^0_{ij} d\eta = \begin{bmatrix} -CS & -l_{ij}CC & CS \\ CS & -l_{ij}SS & -CS \\ (CC-SS) & -l_{ij}2CS & -(CC-SS) \end{bmatrix}}, \tag{3.86}$$

and the standard $\boldsymbol{B}$-matrix $\boldsymbol{B}_{KL0}$, can be constructed by assembling $\boldsymbol{B}^{KL0}_{ij}$.

Since the standard edge displacement uses linear shape functions, a linear enrichment function is defined. To connect the enrichment function $\Psi(\eta)$, to the enriched DOF $\Delta w^F_{,n}$, the function should have a constant jump in derivative at the enriched node. The optimally scaled enrichment function for the foldable beam, found in Appendix C, is such a function, and the edges are thus enriched using:

$$\Psi^{l}(\eta) = l_{ij}\begin{cases} -\eta(1-\eta_\Gamma) & 0 \leq \eta \leq \eta_\Gamma \\ -\eta_\Gamma(1-\eta) & \eta_\Gamma \leq \eta \leq 1 \end{cases}, \tag{3.87}$$

with its derivative forming the strong enrichment for the edge rotation:

$$\Psi^{l}_{,s}(\eta) = \frac{\Psi_{,\eta}(\eta)}{l_{ij}} = \begin{cases} -(1-\eta_\Gamma) & 0 \leq \eta \leq \eta_\Gamma \\ \eta_\Gamma & s_\Gamma \leq \eta \leq 1 \end{cases}, \tag{3.88}$$

where $\eta_\Gamma = s_\Gamma / l_{ij}$ is the fold location expressed in the generalized coordinate. The displacement field enrichment is zero at the standard nodes and has a jump in derivative of 1 at the fold, it thus does not interfere with the standard element DOFs and can be coupled to the enriched DOF. Using the enrichment function, the first part of the enriched $\boldsymbol{B}$-matrix as found in Equation 3.71, is calculated as:

$$\begin{aligned} \boldsymbol{B}^{i}_{E} &= -l_{ij}\int_{0}^{\eta_\Gamma} (M_{nn}S_{\theta i} + M_{ns}C_{\theta i})\,\Psi^{l}_{,s}(\eta)d\eta - l_{ij}\int_{\eta_\Gamma}^{1} (M_{nn}S_{\theta i} + M_{ns}C_{\theta i})\,\Psi^{l}_{,s}(\eta)d\eta \\ &= -l_{ij}\,(M_{nn}S_{\theta i} + M_{ns}C_{\theta i})\,[\Psi^{l}(\eta)]_{0}^{\eta_\Gamma} - l_{ij}\,(M_{nn}S_{\theta i} + M_{ns}C_{\theta i})\,[\Psi^{l}(\eta)]_{\eta_\Gamma}^{1} = 0. \end{aligned} \tag{3.89}$$

Due to the constant moment used in the element, the enrichment on the element edge does not contribute to the element stiffness matrix. Nonetheless, it is still used in post processing the solution to find the enriched node displacement $w_{\Gamma i}$ as:

$$w_{\Gamma i} = \begin{bmatrix} 1-\eta_\Gamma & \eta_\Gamma \end{bmatrix}\begin{bmatrix} w_i \\ w_j \end{bmatrix} + \Psi^{l}(\eta_\Gamma)C_{\theta_i}\Delta w^{F}_{,ni}. \tag{3.90}$$

The second contribution for the enriched $\boldsymbol{B}$-matrix consists of an integral over the fold line, where a constant jump in rotation is used $\Delta w_{,n}(\eta) = \Delta w_{,n}$, and a transformation between the moment field and M^{F}_{nn} is defined as:

$$M^{F}_{nn} = \begin{bmatrix} C_F C_F & S_F S_F & 2C_F S_F \end{bmatrix}\boldsymbol{\beta}_3 = \boldsymbol{R}^{c}_{F}\boldsymbol{\beta}_3. \tag{3.91}$$

Using these functions, the enriched $\boldsymbol{B}$-matrix is defined as:

$$\boldsymbol{\beta}_3^{\intercal}\boldsymbol{B}^{F}_{E}\boldsymbol{u}_E = \int_{\Gamma_F} \Delta w^{F}_{,n} M^{F}_{nn} ds_F = \boldsymbol{\beta}_3^{\intercal} l_F \int_{0}^{1} \boldsymbol{R}^{c^{\intercal}}_{F}\, d\eta\ \Delta w^{F}_{,n}, \tag{3.92}$$

resulting in:

$$\boxed{\boldsymbol{B}^{F(1)}_{c} = \boldsymbol{B}^{F}_{E} = l_F \int_{0}^{1} \begin{bmatrix} C_F C_F \\ S_F S_F \\ 2C_F S_F \end{bmatrix} d\eta = l_F \begin{bmatrix} C_F C_F \\ S_F S_F \\ 2C_F S_F \end{bmatrix}.} \tag{3.93}$$

Furthermore, from the definition of the torsional stiffness matrix:

$$\frac{1}{2}\boldsymbol{u}^{\intercal}_{EF}\boldsymbol{K}^{(1)}_{t}\boldsymbol{u}_E = \int_{\Gamma_F} \frac{1}{2}\Delta w^{F}_{,n}(s_F)k_t \Delta w^{F}_{,n}(s_F) dS_F, \tag{3.94}$$

we find that it is simplified to a torsional stiffness coefficient as:

$$\boxed{K^{(1)}_{t} = l_F k_t.} \tag{3.95}$$

Using the defined matrices, the stiffness matrix is formulated by assembling $\boldsymbol{B}^{KL0}_{ij}$ into $\boldsymbol{B}_{KL0}$, and assembling the final $\boldsymbol{B}$-matrix as:

$$\boldsymbol{B}_{KL0^{(1)}} = \begin{bmatrix} \boldsymbol{B}_{KL0}, & \boldsymbol{B}^{F(1)}_{c} \end{bmatrix}. \tag{3.96}$$

Consequently, the stiffness matrix is formulated as:

$$\boxed{\boldsymbol{K}_{KL0^{(1)}} = \boldsymbol{B}^{\intercal}_{KL0^{(1)}}\boldsymbol{A}_c^{-1}\boldsymbol{B}_{KL0^{(1)}} + \boldsymbol{K}_F^{(1)},} \tag{3.97}$$

where $\boldsymbol{K}_F^{(1)}$ is constructed as a 7×7 matrix containing mostly zeros, but with $K_t^{(1)}$ assembled in the lower right corner, at the diagonal term related to $\Delta w^F_{,n}$.

Finally, a distributed edge load is applied on the element by inserting the standard displacement and rotation as found in Equations 3.83 and 3.84, and enriched interpolations found in Equations 3.87 and 3.88, into Equation 3.78. Since no displacement field is defined on the element domain Ω, the application of a distributed pressure q is a bit more difficult. In the 5 DOF beam formulation, a distributed force was applied via a relatively complex equivalent load vector, as described in Appendix B. To apply a surface pressure in the foldable plate formulation, a similar method would result in an increasingly complex equivalent load vector computation. For this reason a constant surface pressure is applied on the $KL0^{(2)}$-element, using the same load vector as found for its non-enriched counterpart in [39]:

$$\boldsymbol{f}^{\intercal}\boldsymbol{u}_{KL0^{(1)}} = \frac{qS_a}{3}\begin{bmatrix}1 & 0 & 1 & 0 & 1 & 0 & 0\end{bmatrix}\boldsymbol{u}_{KL0^{(1)}}, \tag{3.98}$$

where the displacement vector is assembled as: $\boldsymbol{u}^{\intercal}_{KL0^{(1)}} = [w_1,\ \phi_{n1},\ w_2,\ \phi_{n2},\ w_3,\ \phi_{n3},\ \Delta w^F_{,n}]$.

3.3.5. KL0 element enriched with 2 DOFs

The $KL0$ element is a constant moment element, and thus only requires a constant jump in rotation to capture the potential energy in the fold. However, in that case, enriched DOFs cannot be shared between neighboring elements, which may cause the displacement field across enriched element edges to become discontinuous, since neighboring elements can have different jumps in rotation. To solve this problem, the enriched element in Figure 3.7 (the $KL0^{(2)}$-element) is introduced. This foldable element has two enriched DOFs, resulting in a linear interpolation for the jump in rotation along the fold. Since the two enriched DOFs are located on the enriched nodes, they can be shared between neighboring elements, resulting in a continuous displacement field.

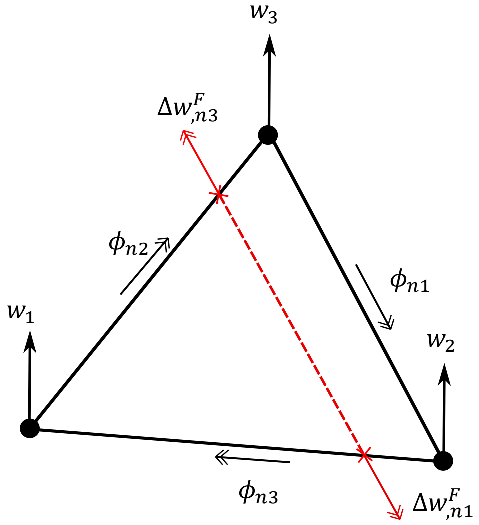

Figure 3.7: The two DOF enriched $KL0$ element ($KL0^{(2)}$-element). On each enriched node (depicted as a cross) one enriched DOF is added, represented by the red arrows $\Delta w^F_{,n1}$ and $\Delta w^F_{,n3}$.

The first part of the $KL0^{(2)}$-element derivation is exactly the same as the $KL0^{(1)}$-element derivation. The derivation diverges from the $KL0^{(1)}$ derivation at Equation 3.92, where the enriched $\boldsymbol{B}$-matrix is defined. Using the two enriched DOFs, a linear interpolation for the jump in rotation is defined as:

$$\Delta w^F_{,n}(\eta) = \boldsymbol{N}_{\Delta\phi}(\eta)\boldsymbol{u}_E = \begin{bmatrix}1-\eta & \eta\end{bmatrix}\begin{bmatrix}\Delta w^F_{,ni}\\ \Delta w^F_{,nj}\end{bmatrix}. \tag{3.99}$$

Since the edge enrichment does not influence the stiffness matrix, the enriched $\boldsymbol{B}$-matrix is defined as:

$$\boxed{\boldsymbol{B}^{F(2)}_c = l_F\int_0^1 \boldsymbol{R}^{c\,\mathsf{T}}_F\boldsymbol{N}_{\Delta\phi}(\eta)d\eta = l_F\int_\Gamma \begin{bmatrix}C_FC_F\\ S_FS_F\\ 2C_FS_F\end{bmatrix}\begin{bmatrix}1-\eta & \eta\end{bmatrix}d\eta = \frac{l_F}{2}\begin{bmatrix}C_FC_F & C_FC_F\\ S_FS_F & S_FS_F\\ 2C_FS_F & 2C_FS_F\end{bmatrix},} \tag{3.100}$$

The torsional stiffness matrix is defined, using the linearly varying jump in rotation:

$$\frac{1}{2}\mathbf{u}^{\mathsf{T}}_E\boldsymbol{K}^{(2)}_t\mathbf{u}_E = \boldsymbol{u}^{\mathsf{T}}_E l_F\int_0^1 \frac{1}{2}\begin{bmatrix}1-\eta\\ \eta\end{bmatrix}k_t\begin{bmatrix}1-\eta & \eta\end{bmatrix}d\eta\,\boldsymbol{u}_E, \tag{3.101}$$

resulting in the 2 × 2 matrix:

$$\boxed{\boldsymbol{K}^{(2)}_t = l_Fk_t\frac{1}{6}\begin{bmatrix}2 & 1\\ 1 & 2\end{bmatrix}.} \tag{3.102}$$

To formulate the $KL0^{(2)}$-element, the $\boldsymbol{B}$-matrix is assembled as:

$$\boldsymbol{B}_{KL0^{(2)}} = \begin{bmatrix}\boldsymbol{B}_{KL0}, & \boldsymbol{B}^{F(2)}_c\end{bmatrix}, \tag{3.103}$$

and the stiffness matrix is defined as:

$$\boxed{\boldsymbol{K}_{KL0^{(2)}} = \boldsymbol{B}^{\mathsf{T}}_{KL0^{(2)}}\boldsymbol{A}^{-1}_c\boldsymbol{B}_{KL0^{(2)}} + \boldsymbol{K}^{(2)}_F,} \tag{3.104}$$

where $\boldsymbol{K}^{(2)}_F$, is constructed as an 8×8 matrix containing mostly zeros, but with $\boldsymbol{K}^{(2)}_t$ assembled in the lower right corner.

Furthermore, an equivalent load vector for distributed edge loads is constructed similarly as in the $KL0^{(1)}$-element, by inserting the standard edge interpolations and enriched interpolation functions into Equation 3.78. Furthermore, a constant surface pressure is applied via a similar load vector as used in the non-enriched $KL0$-element in [39]:

$$\boldsymbol{f}^{\mathsf{T}}\boldsymbol{u}_{KL0^{(2)}} = \frac{qS_a}{3}\begin{bmatrix}1 & 0 & 1 & 0 & 1 & 0 & 0 & 0\end{bmatrix}\boldsymbol{u}_{KL0^{(2)}}, \tag{3.105}$$

where the displacement vector is assembled as: $\boldsymbol{u}^{\mathsf{T}}_{KL0^{(2)}} = [w_1, \phi_{n1}, w_2, \phi_{n2}, w_3, \phi_{n3}, \Delta w^F_{,ni}, \Delta w^F_{,nj}]$.

3.3.6. Enriched KL1 element

A foldable $KL1$ element (the $KL1^{(2)}$-element) is derived using the standard and enriched DOFs as shown in Figure 3.8. The $\boldsymbol{A}$-matrix derivation of the enriched KL1 element is equal to the derivation in [37]. To derive the linear moment $\boldsymbol{A}$-matrix ($\boldsymbol{A}_l$), a linear moment field interpolation field is defined:

$$\boldsymbol{m} = \begin{bmatrix}\boldsymbol{p} & \emptyset & \emptyset\\ \emptyset & \boldsymbol{p} & \emptyset\\ \emptyset & \emptyset & \boldsymbol{p}\end{bmatrix}\boldsymbol{\beta}_9 = \boldsymbol{P}\boldsymbol{\beta}_9, \tag{3.106}$$

where the shape functions are defined using the vector $\boldsymbol{p}$:

$$\boldsymbol{p} = \begin{bmatrix}1 & x & y\end{bmatrix}. \tag{3.107}$$

In the derivation of the constant moment $\boldsymbol{A}$-matrix ($\boldsymbol{A}_c$), three auxiliary DOFs are introduced; in the derivation of $\boldsymbol{A}_l$, nine auxiliary DOFs are introduced in $\boldsymbol{\beta}_9$. Consequently, the linear moment A-matrix is defined using:

$$-\frac{1}{2}\boldsymbol{\beta}^{\mathsf{T}}_9\boldsymbol{A}_l\boldsymbol{\beta}_9 = -\frac{1}{2}\int_\Omega \boldsymbol{m}^{\mathsf{T}}\boldsymbol{D}^{-1}\boldsymbol{m}dA = -\frac{1}{2}\boldsymbol{\beta}^{\mathsf{T}}_9\int_\Omega \boldsymbol{P}^{\mathsf{T}}\boldsymbol{D}^{-1}\boldsymbol{P}dA\boldsymbol{\beta}_9, \tag{3.108}$$

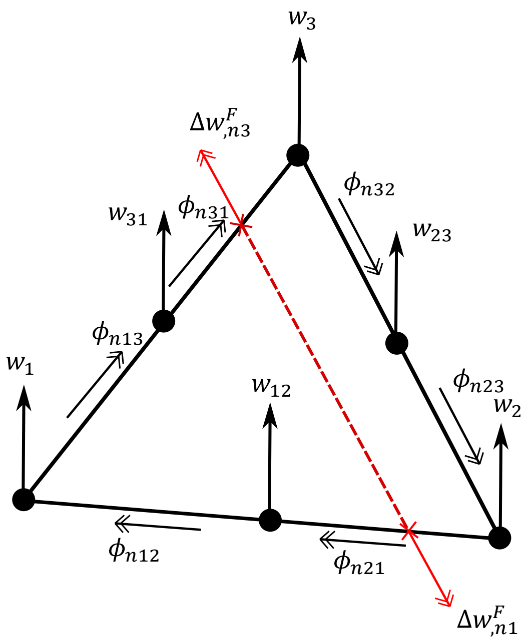

Figure 3.8: The KL1 element with one displacement DOF at each of its six nodes (depicted as dots), two rotational DOFs at each edge, and one enriched DOF at each enriched node (depicted as a cross).

resulting in:

$$\boldsymbol{A}_l = \int_\Omega \boldsymbol{P}^\intercal \boldsymbol{D}^{-1} \boldsymbol{P} dA. \tag{3.109}$$

Due to the diagonal nature of $\boldsymbol{P}$, we can simplify $\boldsymbol{A}_l$ as in [37]:

$$\boldsymbol{A}_l = \begin{bmatrix} c_{11}\boldsymbol{\Phi} & c_{12}\boldsymbol{\Phi} & c_{13}\boldsymbol{\Phi} \\ c_{21}\boldsymbol{\Phi} & c_{22}\boldsymbol{\Phi} & c_{23}\boldsymbol{\Phi} \\ c_{31}\boldsymbol{\Phi} & c_{32}\boldsymbol{\Phi} & c_{33}\boldsymbol{\Phi} \end{bmatrix}, \tag{3.110}$$

where c_{ij} are the components of $\boldsymbol{D}^{-1}$, the inverse material stiffness matrix, and $\boldsymbol{\Phi}$ is defined as:

$$\boldsymbol{\Phi} = \int_\Omega \boldsymbol{p}^\intercal \boldsymbol{p} dA = \int_\Omega \begin{bmatrix} 1 & x & y \\ x & x^2 & xy \\ y & xy & y^2 \end{bmatrix} dA. \tag{3.111}$$

Because the origin of the local coordinate system is located at the centroid of the triangle, $\boldsymbol{\Phi}$ can be simplified using the surface area of the element:

$$\boldsymbol{\Phi} = \begin{bmatrix} S_a & 0 & 0 \\ 0 & \alpha & \psi \\ 0 & \psi & \gamma \end{bmatrix}, \tag{3.112}$$

where α, ψ, and γ are defined as:

$$\alpha = \frac{S_a}{12}(x_1^2 + x_2^2 + x_3^2), \tag{3.113}$$

$$\psi = \frac{S_a}{12}(x_1 y_1 + x_2 y_2 + x_3 y_3), \tag{3.114}$$

$$\gamma = \frac{S_a}{12}(y_1^2 + y_2^2 + y_3^2). \tag{3.115}$$

The element stiffness matrix is calculated using the inverse of $\boldsymbol{A}_l$ [37]:

$$\boxed{\boldsymbol{A}_l^{-1} = \begin{bmatrix} d_{11}\boldsymbol{\Phi}^{-1} & d_{12}\boldsymbol{\Phi}^{-1} & d_{13}\boldsymbol{\Phi}^{-1} \\ d_{21}\boldsymbol{\Phi}^{-1} & d_{22}\boldsymbol{\Phi}^{-1} & d_{23}\boldsymbol{\Phi}^{-1} \\ d_{31}\boldsymbol{\Phi}^{-1} & d_{32}\boldsymbol{\Phi}^{-1} & d_{33}\boldsymbol{\Phi}^{-1} \end{bmatrix},} \tag{3.116}$$

where d_{ij} are the components of $\boldsymbol{D}$, and the matrix $\boldsymbol{\Phi}^{-1}$ is defined as:

$$\boxed{\boldsymbol{\Phi}^{-1} = \frac{1}{S_a(\alpha\gamma - \psi^2)} \begin{bmatrix} \alpha\gamma - \psi^2 & 0 & 0 \\ 0 & S_a\gamma & -S_a\psi \\ 0 & -S_a\psi & S_a\alpha \end{bmatrix}.} \tag{3.117}$$

From Equations 3.48 to 3.50, the transformation between $\boldsymbol{\beta}$ and $[Q_n,\ -M_{nn},\ -M_{ns}]$, can be constructed using the linear moment field interpolation:

$$\begin{bmatrix} Q_n \\ -M_{nn} \\ -M_{ns} \end{bmatrix} = \begin{bmatrix} C\frac{\partial}{\partial x} & S\frac{\partial}{\partial y} & C\frac{\partial}{\partial y} + S\frac{\partial}{\partial x} \\ -CC & -SS & -2CS \\ CS & -CS & SS - CC \end{bmatrix} \boldsymbol{m} = \begin{bmatrix} C\frac{\partial}{\partial x} & S\frac{\partial}{\partial y} & C\frac{\partial}{\partial y} + S\frac{\partial}{\partial x} \\ -CC & -SS & -2CS \\ CS & -CS & SS - CC \end{bmatrix} P\boldsymbol{\beta}_9$$
$$\begin{bmatrix} 0 & C & 0 & 0 & 0 & S & 0 & S & C \\ -CC & -CCx & -CCy & -SS & -SSx & -SSy & -2CS & -2CSx & -2CSy \\ CS & CSx & CSy & -CS & -CSx & -CSy & (SS-CC) & (SS-CC)x & (SS-CC)y \end{bmatrix} \boldsymbol{\beta}_9 = \boldsymbol{R}^l_{ij}\boldsymbol{\beta}_9, \tag{3.118}$$

where the global coordinates on the element edge can be calculated using the generalized coordinate η, as: $x = x_i + \eta\Delta x_{ij}$ and $y = y_i + \eta\Delta y_{ij}$. The standard displacement and rotation interpolation along the edges are defined as in [39]:

$$w(\eta) = \begin{bmatrix} (1-\eta)(1-2\eta) & 4\eta(1-\eta) & \eta(2\eta-1) \end{bmatrix} \begin{bmatrix} w_i \\ w_{ij} \\ w_j \end{bmatrix}, \tag{3.119}$$

$$w_{,s}(\eta) = \frac{1}{l_{ij}} \begin{bmatrix} -3+4\eta & 4-8\eta & -1+4\eta \end{bmatrix} \begin{bmatrix} w_i \\ w_{ij} \\ w_j \end{bmatrix}, \tag{3.120}$$

$$w_{,n}(\eta) = \begin{bmatrix} 1-\eta & \eta \end{bmatrix} \begin{bmatrix} \phi_{n_{ij}} \\ \phi_{n_{ji}} \end{bmatrix}, \tag{3.121}$$

where the displacement is defined in terms of the corner node displacements $(w_i,\ w_j)$ and the mid node displacement (w_{ij}), and the edge rotations $\phi_{n_{ij}}$ and $\phi_{n_{ji}}$, are the rotation of edge ij at nodes i and j respectively. All interpolation functions are assembled in $\boldsymbol{L}^1_{ij}$ as:

$$\begin{bmatrix} w \\ w_{,n} \\ w_{,s} \end{bmatrix} = \begin{bmatrix} (1-\eta)(1-2\eta) & 0 & 4\eta(1-\eta) & 0 & \eta(2\eta-1) \\ 0 & 1-\eta & 0 & \eta & 0 \\ \frac{-3+4\eta}{l_{ij}} & 0 & \frac{4-8\eta}{l_{ij}} & 0 & \frac{-1+4\eta}{l_{ij}} \end{bmatrix} \begin{bmatrix} w_i \\ \phi_{nij} \\ w_{mij} \\ \phi_{nji} \\ w_j \end{bmatrix} = \boldsymbol{L}^1_{ij}\boldsymbol{u}_{ij}, \tag{3.122}$$

and using Equation 3.53, the $\boldsymbol{B}_{ij}$ matrix is formed as:

$$\boxed{\boldsymbol{B}^{KL1}_{ij} = l_{ij} \int_0^1 \boldsymbol{R}^{l\ \mathrm{T}}_{ij} \boldsymbol{L}^1_{ij} d\eta,} \tag{3.123}$$

and the sub-matrices $\boldsymbol{B}_{ij}$ can be assembled to form $\boldsymbol{B}_{KL1}$.

In line with the standard edge displacement in equation 3.119, a quadratic edge enrichment function is defined. At the enriched node, the enrichment function should be C^0-continuous, and have a jump in derivative equal to one. Furthermore, it is not desirable for the enrichment function to interfere with the standard DOFs. At the corner nodes, the enrichment function and its derivative should thus be zero. To formulate an enrichment function which is able to fulfill these requirements, a piecewise quadratic function is defined:

$$\Psi^q(s) = \begin{cases} \Psi^L & 0 \le s \le s_\Gamma \\ \Psi^R & s_\Gamma \le s \le L \end{cases} = \begin{cases} C_1 s^2 + C_2 s + C_3 & 0 \le s \le s_\Gamma \\ C_4 s^2 + C_5 s + C_6 & s_\Gamma \le s \le L \end{cases}, \tag{3.124}$$

and six requirements are defined as:

$$\Psi^L(0) = \Psi^R(L) = 0, \tag{3.125}$$

$$\Psi^L(s_\Gamma) = \Psi^R(s_\Gamma), \tag{3.126}$$

$$\frac{d\Psi^L}{ds}(0) = \frac{d\Psi^R}{ds}(L) = 0, \tag{3.127}$$

$$\frac{d\Psi^R}{ds}(s_\Gamma) - \frac{d\Psi^L}{ds}(s_\Gamma) = 1. \tag{3.128}$$

Lastly, the six parameters C_i, are defined using the six requirements:

$$C_1 = -\frac{l_{ij} - s_\Gamma}{2l_{ij}s_\Gamma},\ C_2 = C_3 = 0, \tag{3.129}$$

$$C_4 = \frac{s_\Gamma}{2l_{ij}(s_\Gamma - l_{ij})},\ C_5 = \frac{s_\Gamma}{l_{ij} - s_\Gamma} \text{ and } C_6 = -\frac{l_{ij}s_\Gamma}{2(l_{ij} - s_\Gamma)}. \tag{3.130}$$

A piecewise linear rotation enrichment as in Figure 3.10, is defined as the derivative of the piecewise quadratic displacement enrichment $\Psi^q_{,s}$. A disadvantage of the displacement enrichment can be found in Figure 3.9, the enrichment is not zero at the mid side node (at $s = 0.5$), and will thus interfere with the mid side displacement w_{ij}. Another property of the enrichment is that when the enriched node approximates the corner nodes ($s_\Gamma \to 0$, $s_\Gamma \to l_{ij}$), the entire displacement enrichment tends to zero $\Psi^q(s) \to 0$. Moreover, the rotation enrichment is bounded as: $-1 \leq \Psi^q_{,s}(s) \leq 1$ for $0 \leq s_\Gamma \leq l_{ij}$.

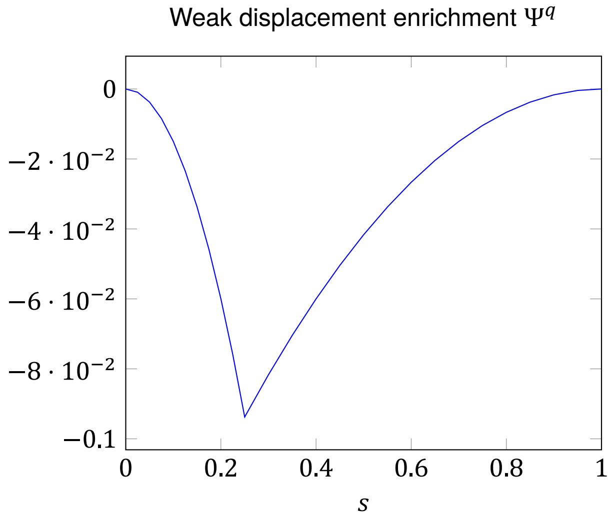

Figure 3.9: The displacement field enrichment for an edge of length 1 with an enriched node at $s_\Gamma = 0.25$.

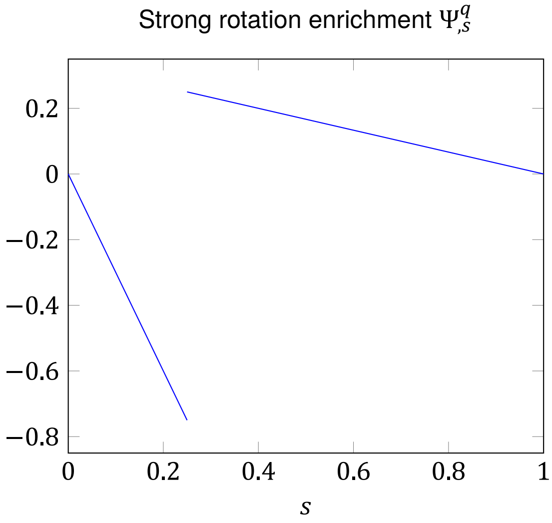

Figure 3.10: The rotational field enrichment for an edge of length 1 with an enriched node at $s_\Gamma = 0.25$.

All the enrichment functions on a boundary segment are assembled into $\boldsymbol{L}^F_{ij}$ as:

$$\begin{bmatrix} w \\ w_{,n} \\ w_{,s} \end{bmatrix} = \begin{bmatrix} C_{\theta i}\Psi^q(s) \\ S_{\theta i}\Psi^q(s)_{,s} \\ C_{\theta i}\Psi^q(s)_{,s} \end{bmatrix} \Delta w^F_{,ni} = \boldsymbol{L}^F_{ij}\Delta w^F_{,ni}, \tag{3.131}$$

and using Equation 3.71, the contribution of the enrichment functions to the enriched $\boldsymbol{B}$-matrix becomes:

$$\boxed{\boldsymbol{B}^i_l = l_{ij}\left\{\int_0^{\eta_\Gamma} \boldsymbol{R}^l_{ij}{}^\intercal \boldsymbol{L}^F_{ij} d\eta + \int_{\eta_\Gamma}^1 \boldsymbol{R}^l_{ij}{}^\intercal \boldsymbol{L}^F_{ij} d\eta\right\},} \tag{3.132}$$

which is evaluated numerically, and where $\boldsymbol{L}^F_{ij}$ and $\boldsymbol{R}^F_{ij}$ are transformed to the local coordinate η. To define the second part of the enriched $\boldsymbol{B}$-matrix, the moment along the fold is defined as:

$$M^F_{nn} = \begin{bmatrix} C_F^2 & C_F^2 x & C_F^2 y & S_F^2 & S_F^2 x & S_F^2 y & 2C_F S_F & 2C_F S_F x & 2C_F S_F y \end{bmatrix} \boldsymbol{\beta}_9 = \boldsymbol{R}^l_F \boldsymbol{\beta}_9, \tag{3.133}$$

and using a linear interpolation for $\Delta w^F_{,n}$, as in Equation 3.99, $\boldsymbol{B}^F_l$ is defined as:

$$\boldsymbol{\beta}^\intercal \boldsymbol{B}^F_l \boldsymbol{u}_E = \int_{\Gamma_F} M_{nn} \Delta w^F_{,n} ds_F = \boldsymbol{\beta}^\intercal l_F \int_0^1 {\boldsymbol{R}^l_F}^\intercal \boldsymbol{N}_{\Delta\phi} d\eta \boldsymbol{u}_E = \boldsymbol{\beta}^\intercal l_F \int_0^1 \begin{bmatrix} C_F^2 \\ C_F^2 x \\ C_F^2 y \\ S_F^2 \\ S_F^2 x \\ S_F^2 y \\ 2C_F S_F \\ 2C_F S_F x \\ 2C_F S_F y \end{bmatrix} \begin{bmatrix} 1-\eta & \eta \end{bmatrix} d\eta \begin{bmatrix} \Delta w^F_{,ni} \\ \Delta w^F_{,nj} \end{bmatrix}, \tag{3.134}$$

resulting in:

$$\boxed{\boldsymbol{B}^F_l = l_F \begin{bmatrix} C_F^2 I \\ S_F^2 I \\ 2C_F S_F I \end{bmatrix} \begin{bmatrix} \frac{1}{2} & \frac{1}{2} \\ \frac{x_1^F}{2} + \frac{\Delta x^F}{6} & \frac{x_1^F}{2} + \frac{\Delta x^F}{3} \\ \frac{y_1^F}{2} + \frac{\Delta y^F}{6} & \frac{y_1^F}{2} + \frac{\Delta y^F}{3} \end{bmatrix}}, \tag{3.135}$$

where I is a 3×3 identity matrix.

The enriched $\boldsymbol{B}$-matrix for the $KL1^{(2)}$ element is formed by assembling the two $\boldsymbol{B}^i_l$-matrices, connected to the two enriched edges, and the $\boldsymbol{B}^F_l$-matrix, connected to the fold line:

$$\boldsymbol{B}_l = \begin{bmatrix} \boldsymbol{B}^i_l & \boldsymbol{B}^j_l \end{bmatrix} + \boldsymbol{B}^F_l, \tag{3.136}$$

where i and j are the indices of the two enriched DOFs. Finally, the $\boldsymbol{B}$-matrix for the foldable KL1 element is assembled as:

$$\boldsymbol{B}_{KL1^{(2)}} = \begin{bmatrix} \boldsymbol{B}_{KL1} & \boldsymbol{B}_l \end{bmatrix}. \tag{3.137}$$

Since the same linear moment interpolation for the jump in rotation ($\Delta w_{,n}(\eta) = \boldsymbol{N}_{\Delta\phi}(\eta)\boldsymbol{u}_E$) is used in the $KL1^{(2)}$ and $KL0^{(2)}$-element derivation, both elements use the same torsional stiffness matrix $\boldsymbol{K}^{(2)}_t$, as defined in Equation 3.102. Using these definitions, the stiffness matrix is formulated as:

$$\boxed{\boldsymbol{K}_{KL1^{(2)}} = \boldsymbol{B}^\intercal_{KL1^{(2)}} \boldsymbol{A}_l^{-1} \boldsymbol{B}_{KL1^{(2)}} + \boldsymbol{K}^{(2)}_F,} \tag{3.138}$$

where $\boldsymbol{K}^{(2)}_F$ is constructed as an 14×14 matrix containing mostly zeros, but with $\boldsymbol{K}^{(2)}_t$ assembled in the lower right corner.

Furthermore, to apply a constant surface pressure on the plate, ta similar load vector as in the non-enriched $KL1$-element in [39] is used:

$$\boldsymbol{f}^\intercal \boldsymbol{u}_{KL1^{(2)}} = \frac{qS_a}{3} \begin{bmatrix} 0 & 1 & 0 & 0 & 0 & 1 & 0 & 0 & 0 & 1 & 0 & 0 & 0 & 0 \end{bmatrix} \boldsymbol{u}_{KL1^{(2)}}, \tag{3.139}$$

where the displacement vector is assembled as:

$$\boldsymbol{u}^\intercal_{KL1^{(2)}} = \begin{bmatrix} w_1 & w_{23} & \phi_{n23} & \phi_{n32} & w_2 & w_{31} & \phi_{n31} & \phi_{n13} & w_3 & w_{12} & \phi_{n12} & \phi_{n21} & \Delta w_{,ni} & \Delta w_{,nj} \end{bmatrix}. \tag{3.140}$$

Moreover, a distributed edge load is again applied by inserting the defined enriched and standard edge interpolations into Equation 3.78.

3.3.7. Enriched HSM element

The HSM element is a linear moment element, similar to the $KL1$ element, it is enriched using the standard and enriched DOFs as shown in Figure 3.11, resulting in the foldable $HSM^{(2)}$-element. Since both the HSM and $KL1$ elements use a linearly varying moment field, a large part of their derivation is similar, and the derivation of the $HSM^{(2)}$-element diverges from the $KL1^{(2)}$ element only in the formulation of the standard $\boldsymbol{B}$-matrix.

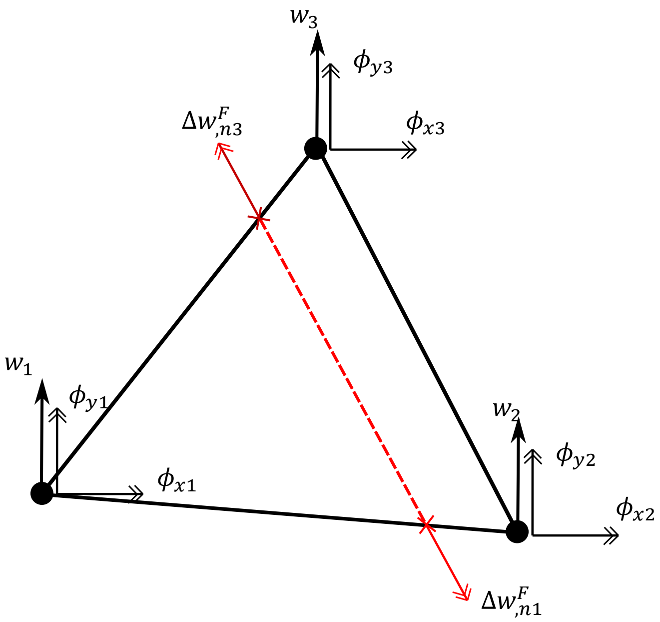

Figure 3.11: The enriched HSM element with one displacement DOF and two rotational DOFs at each standard node (depicted as dots), and one enriched DOF at each enriched node (depicted as a cross).

The main differences between the HSM and $KL1$ element derivation are thus the standard DOFs and shape functions used. The standard HSM-element uses one displacement (w_i) and two rotational DOFs (ϕ_{xi} and ϕ_{yi}) at each corner node, resulting in 9 standard DOFs. The rotational DOFs are defined in the global coordinate system, and are transformed to the edge local coordinate system using Figure 3.12:

$$\begin{bmatrix} w_{,s} \\ w_{,n} \end{bmatrix} = \begin{bmatrix} C & S \\ S & -C \end{bmatrix} \begin{bmatrix} \phi_x \\ \phi_y \end{bmatrix}. \tag{3.141}$$

The standard displacement and rotation interpolation along the edges are defined as [37]:

$$w(\eta) = H_{01} w_i + H_{02} w_j + H_{11} w_{,si} + H_{12} w_{,sj}, \tag{3.142}$$

$$w_{,n}(\eta) = (1-\eta) w_{,ni} + \eta w_{,nj}, \tag{3.143}$$

$$w_{,s}(\eta) = \frac{1}{l_{ij}} (H_{01,\eta} w_i + H_{02,\eta} w_j + H_{11,\eta} w_{,si} + H_{12,\eta} w_{,sj}), \tag{3.144}$$

where the shape functions are defined as:

$$H_{01} = 1 - 3\eta^2 + 2\eta^3, \tag{3.145}$$

$$H_{02} = 3\eta^2 - 2\eta^3, \tag{3.146}$$

$$H_{11} = l_{ij}(\eta - 2\eta^2 + \eta^3), \tag{3.147}$$

$$H_{12} = l_{ij}(-\eta^2 + \eta^3), \tag{3.148}$$

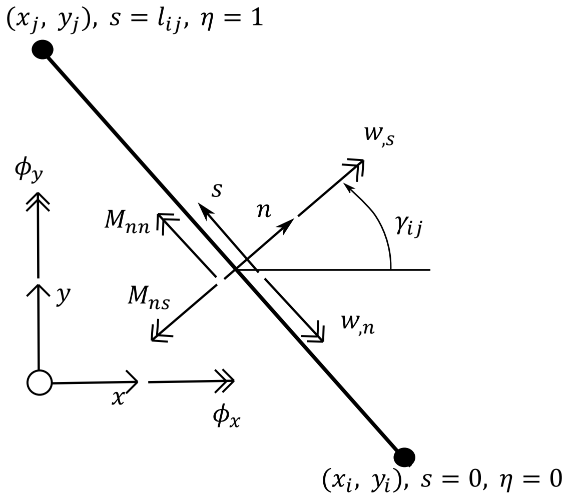

Figure 3.12: One of the three element edges of the HSM element. The rotation defined in the global coordinate system ϕ_x and ϕ_y, are transformed to the local rotations $w_{,n}$ and $w_{,s}$, using the angle γ_{ij}.

and their derivatives as:

$$H_{01,\eta} = -6\eta + 6\eta^2, \tag{3.149}$$

$$H_{02,\eta} = 6\eta - 6\eta^2, \tag{3.150}$$

$$H_{11,\eta} = l_{ij}(1 - 4\eta + 3\eta^2), \tag{3.151}$$

$$H_{12,\eta} = l_{ij}(-2\eta + 3\eta^2). \tag{3.152}$$

$$\tag{3.153}$$

The global rotations are transformed to the edge local rotations using Equation 3.141, and all standard shape functions are assembled as:

$$\begin{bmatrix} w \\ w_{,n} \\ w_{,s} \end{bmatrix} = \begin{bmatrix} H_{01} & CH_{11} & SH_{11} & H_{02} & CH_{12} & SH_{12} \\ 0 & S(1-\eta) & -C(1-\eta) & 0 & S\eta & -C\eta \\ \frac{H_{01,\eta}}{l_{ij}} & \frac{CH_{11,\eta}}{l_{ij}} & \frac{SH_{11,\eta}}{l_{ij}} & \frac{H_{02,\eta}}{l_{ij}} & \frac{CH_{12,\eta}}{l_{ij}} & \frac{SH_{12,\eta}}{l_{ij}} \end{bmatrix} \begin{bmatrix} w_i \\ \phi_{xi} \\ \phi_{yi} \\ w_j \\ \phi_{xj} \\ \phi_{yj} \end{bmatrix} = \boldsymbol{L}_{ij}^{HSM} \boldsymbol{u}_{ij}, \tag{3.154}$$

Finally, the matrices are combined into $\boldsymbol{B}_{ij}^{HSM}$ as:

$$\boxed{\boldsymbol{B}_{ij}^{HSM} = l_{ij} \int_0^1 \boldsymbol{R}_{ij}^{l\ \intercal} \boldsymbol{L}_{ij}^{HSM} d\eta}\ , \tag{3.155}$$

and the standard $\boldsymbol{B}$-matrix ($\boldsymbol{B}_{HSM}$) is formed by assembling the three $\boldsymbol{B}_{ij}^{HSM}$-matrices.

Since the $KL1^{(2)}$ and $HSM^{(2)}$ elements use the same linear moment field, enriched DOFs ($\Delta w_{,ni}^F$), edge enrichment ($\Psi^q(s)$), and interpolation for the jump in rotation ($\boldsymbol{N}_{\Delta\phi}(\eta)$), the exact same enriched $\boldsymbol{B}$-matrix ($\boldsymbol{B}_l$) and torsional stiffness matrix ($\boldsymbol{K}_t^{(2)}$) are used in the $HSM^{(2)}$-element, as in the $KL1^{(2)}$-element. To formulate the stiffness matrix the $\boldsymbol{B}$-matrix is thus assembled as:

$$\boldsymbol{B}_{HSM^{(2)}} = [\boldsymbol{B}_{HSM}, \boldsymbol{B}_l]\,, \tag{3.156}$$

and the stiffness matrix is formulated as:

$$\boxed{\boldsymbol{K}_{HSM^{(2)}} = \boldsymbol{B}_{HSM^{(2)}}^{\intercal} \boldsymbol{A}_l \boldsymbol{B}_{HSM^{(2)}} + \boldsymbol{K}_F^{(2)}}\,, \tag{3.157}$$

where $\boldsymbol{K}_F^{(2)}$ is constructed as an 11×11 matrix containing mostly zeros, with $\boldsymbol{K}_t^{(2)}$ assembled in the lower right corner.

As was done in all previous elements, a constant surface pressure is applied on the plate, via a similar load vector as in the non-enriched HSM-element in [37]:

$$\boldsymbol{f}^{\intercal}\boldsymbol{u}_{HSM^{(2)}} = \frac{qS_a}{3}\begin{bmatrix} 1 & 0 & 0 & 1 & 0 & 0 & 1 & 0 & 0 & 1 & 0 \end{bmatrix}\boldsymbol{u}_{HSM^{(2)}}, \tag{3.158}$$

where the displacement vector is assembled as:

$$\boldsymbol{u}^{\intercal}_{HSM^{(2)}} = \begin{bmatrix} w_1 & \phi_{x1} & \phi_{y1} & w_2 & \phi_{x2} & \phi_{y2} & w_3 & \phi_{x3} & \phi_{y3} & \Delta w_{,ni} & \Delta w_{,nj} \end{bmatrix}. \tag{3.159}$$

Moreover, a distributed edge load can be applied by inserting the enriched and standard interpolation functions into Equation 3.78.

3.3.8. Two condensed foldable plate elements

Two more foldable plate elements are defined, by condensing the foldable $KL0$ and $KL1$ elements locally. Firstly, the $KL0^{(1)}$-element is condensed using Equation 3.30:

$$\boxed{\boldsymbol{K}_{KL0^{(c)}} = \boldsymbol{B}^{\intercal}_{KL0}\left(\boldsymbol{A}_c + \boldsymbol{B}_c^{F(1)}K_t^{(1)^{-1}}\boldsymbol{B}_c^{F(1)\intercal}\right)^{-1}\boldsymbol{B}_{KL0},} \tag{3.160}$$

resulting in a foldable $KL0^{(c)}$-element with the exact same DOFs as the non-enriched $KL0$ element. Investigating the condensed formulation, the only difference between the standard non-foldable $KL0$-element and the $KL0^{(c)}$-element is found in an addition to the $\boldsymbol{A}_c$-matrix of $\boldsymbol{B}_c^{F(1)}K_t^{(1)^{-1}}\boldsymbol{B}_c^{F(1)\intercal}$, where:

$$\boldsymbol{B}_c^{F(1)}K_t^{(1)^{-1}}\boldsymbol{B}_c^{F(1)\intercal} = \frac{l_F}{k_t}\begin{bmatrix} C_F^4 & C_F^2S_F^2 & 2C_F^3S_F \\ C_F^2S_F^2 & S_F^4 & 2C_FS_F^3 \\ 2C_F^3S_F & 2C_FS_F^3 & 4C_F^2S_F^2 \end{bmatrix}. \tag{3.161}$$

If a fold approximates a standard element node, the fold length l_F decreases to zero, and the addition to the $\boldsymbol{A}_c$-matrix will also decrease: $\boldsymbol{B}_c^{F(1)}K_t^{(1)^{-1}}\boldsymbol{B}_c^{F(1)\intercal} \rightarrow \emptyset$, causing the $KL0^{(c)}$-element to converge to a standard non-foldable $KL0$-element. Furthermore, investigating the general condensed formulation in Equation 3.30 and the $KL0^{(c)}$ formulation in Equation 3.160, it is found that the only difference between condensed $KL0^{(1)}$ and $KL0^{(2)}$elements would be in the $\boldsymbol{B}_E\boldsymbol{K}_t^{-1}\boldsymbol{B}_E^{\intercal}$ term, for which it is found that:

$$\boldsymbol{B}_E\boldsymbol{K}_t^{-1}\boldsymbol{B}_E^{\intercal} = \boldsymbol{B}_c^{F(1)}K_t^{(1)^{-1}}\boldsymbol{B}_c^{F(1)\intercal} = \boldsymbol{B}_c^{F(2)}\boldsymbol{K}_t^{(2)^{-1}}\boldsymbol{B}_c^{F(2)\intercal}. \tag{3.162}$$

Condensing the $KL0^{(1)}$ and $KL0^{(2)}$ elements, thus results in the exact same 6 DOF foldable $KL0^{(c)}$-element. Another foldable element is created by local condensation of the $KL1^{(2)}$-element, resulting in the 12 DOF foldable $KL1^{(c)}$-element:

$$\boxed{\boldsymbol{K}_{KL1^{(c)}} = \boldsymbol{B}^{\intercal}_{KL1}\left(\boldsymbol{A}_l + \boldsymbol{B}_l^{\intercal}\boldsymbol{K}_t^{(2)^{-1}}\boldsymbol{B}_l\right)^{-1}\boldsymbol{B}_{KL1}.} \tag{3.163}$$

By condensing the $KL1^{(2)}$-element, enriched DOFs can not be shared between neighboring elements, which may introduce an enriched edge continuity error in the $KL1^{(c)}$-element.

Since the enriched DOFs are condensed out of the elements, the calculation of the enriched node displacement is a bit more difficult. To calculate this displacement, firstly the auxiliary DOFs ar computed as:

$$\boldsymbol{\beta} = -\left(\boldsymbol{A} + \boldsymbol{B}_E\boldsymbol{K}_t^{-1}\boldsymbol{B}_E^{\intercal}\right)^{-1}\boldsymbol{B}_s\boldsymbol{u}_S, \tag{3.164}$$

secondly the enriched DOFs can be computed as:

$$\boldsymbol{u}_E = \boldsymbol{K}_t^{-1}\boldsymbol{B}_E^{\intercal}\boldsymbol{\beta}, \tag{3.165}$$

and the edge displacement is calculated by inserting the enriched DOF into Equation 3.63.

To apply a constant surface pressure on the condensed elements, the exact same load vectors as found in [39] can be used, as the condensed elements contain the exact same DOFs as their non-foldable counterparts. On the $KL0^{(c)}$-element a constant pressure is applied as:

$$\boldsymbol{f}^{\mathsf{T}}\boldsymbol{u}_{KL0^{(c)}} = \frac{qS_a}{3}\begin{bmatrix}1 & 0 & 1 & 0 & 1 & 0\end{bmatrix}\boldsymbol{u}_{KL0^{(c)}}, \tag{3.166}$$

where the displacement vector is assembled as: $\boldsymbol{u}^{\mathsf{T}}_{KL0^{(c)}} = [w_1,\ \phi_{n1},\ w_2,\ \phi_{n2},\ w_3,\ \phi_{n3}]$, and on the $KL1^{(c)}$-element a constant pressure is applied as:

$$\boldsymbol{f}^{\mathsf{T}}\boldsymbol{u}_{KL1^{(c)}} = \frac{qS_a}{3}\begin{bmatrix}0 & 1 & 0 & 0 & 0 & 1 & 0 & 0 & 0 & 1 & 0 & 0\end{bmatrix}\boldsymbol{u}_{KL1^{(c)}}, \tag{3.167}$$

where the displacement vector is assembled as:

$$\boldsymbol{u}^{\mathsf{T}}_{KL1^{(c)}} = \begin{bmatrix} w_1 & w_{23} & \phi_{n23} & \phi_{n32} & w_2 & w_{31} & \phi_{n31} & \phi_{n13} & w_3 & w_{12} & \phi_{n12} & \phi_{n21} \end{bmatrix}. \tag{3.168}$$

Furthermore, since the enriched DOFs are removed from the elements, a distributed edge load is applied by only using the standard displacement and rotation interpolations:

$$\boldsymbol{f}^{\mathsf{T}}\boldsymbol{u} = \int_{\Gamma}[F_{\Gamma}w + \boldsymbol{m}_{\Gamma}\boldsymbol{\phi}_{\Gamma}]dS = \int_{0}^{l_{ij}}\begin{bmatrix}F_{\Gamma} & \boldsymbol{m}^{\mathsf{T}}_{\Gamma}\end{bmatrix}\boldsymbol{L}_{ij}\boldsymbol{u}_{ij}ds_{ij}, \tag{3.169}$$

where in $\boldsymbol{L}_{ij}$ only the standard edge interpolation functions are present.

3.4. Overview of the enriched elements

In this chapter several different foldable elements have been derived. Based on the $KL0$-element the $KL0^{(1)}$, $KL0^{(c)}$, and $KL0^{(2)}$ elements are derived, based on the $KL1$-element the $KL1^{(2)}$ and $KL1^{(c)}$-elements are derived, and based on the HSM-element, the $HSM^{(2)}$-element is derived. An overview of the different matrices used in these elements can be found in Table 3.1. Two different $\boldsymbol{A}$-matrices are defined; the constant moment $\boldsymbol{A}_c$-matrix, used in all foldable $KL0$-elements, and the linear moment $\boldsymbol{A}_l$-matrix, used in the foldable $KL1$ and HSM-elements. Furthermore, two different torsional stiffness matrices are defined; $K_t^{(1)}$ is used when only one enriched DOF is introduced (in the $KL0^{(1)}$ and $KL0^{(c)}$-elements), and $\boldsymbol{K}_t^{(2)}$ is used when two enriched DOFs are introduced (in the $KL0^{(2)}$, $KL1^{(2)}$, $KL1^{(c)}$, and $HSM^{(2)}$-elements). The matrices used to assemble $\boldsymbol{B}_S$ ($\boldsymbol{B}_{ij}$), are dependent only on the base element used to create the foldable element. The foldable $KL0$-elements use two different enriched $\boldsymbol{B}$-matrices dependent on the amount of enriched DOFs; the $KL0^{(1)}$ and $KL0^{(c)}$ elements introduce only one enriched DOF and use $\boldsymbol{B}_c^{F(1)}$, while the $KL0^{(2)}$-element introduces two enriched DOFs and uses $\boldsymbol{B}_c^{F(2)}$. Since the $KL1^{(2)}$, $KL1^{(c)}$, and $HSM^{(2)}$ elements use the exact same moment field interpolation and edge enrichment, all three elements use the same matrices to assemble $\boldsymbol{B}_E$.

	$KL0^{(1)}$	$KL0^{(2)}$	$KL0^{(c)}$	$KL1^{(2)}$	$KL1^{(c)}$	$HSM^{(2)}$
$\boldsymbol{A}$	$\boldsymbol{A}_c$	$\boldsymbol{A}_c$	$\boldsymbol{A}_c$	$\boldsymbol{A}_l$	$\boldsymbol{A}_l$	$\boldsymbol{A}_l$
$\boldsymbol{K}_F$	$K_t^{(1)}$	$\boldsymbol{K}_t^{(2)}$	$K_t^{(1)}$	$\boldsymbol{K}_t^{(2)}$	$\boldsymbol{K}_t^{(2)}$	$\boldsymbol{K}_t^{(2)}$
$\boldsymbol{B}_S$	$\boldsymbol{B}_{ij}^{KL0}$	$\boldsymbol{B}_{ij}^{KL0}$	$\boldsymbol{B}_{ij}^{KL0}$	$\boldsymbol{B}_{ij}^{KL1}$	$\boldsymbol{B}_{ij}^{KL1}$	$\boldsymbol{B}_{ij}^{HSM}$
$\boldsymbol{B}_E$	$\boldsymbol{B}_c^{F(1)}$	$\boldsymbol{B}_c^{F(2)}$	$\boldsymbol{B}_c^{F(1)}$	$\boldsymbol{B}_l^{i}, \boldsymbol{B}_l^{F}$	$\boldsymbol{B}_l^{i}, \boldsymbol{B}_l^{F}$	$\boldsymbol{B}_l^{i}, \boldsymbol{B}_l^{F}$

Table 3.1: The matrices used in defining the six different foldable elements. Several different matrices are defined to use as $\boldsymbol{A}$ and $\boldsymbol{K}_t$-matrices, and several different sub-matrices are defined to be assembled into the $\boldsymbol{B}_S$ and $\boldsymbol{B}_E$-matrices.

An advantage of the non-enriched moment fields, is the relatively easy construction of the $\boldsymbol{B}_S$ and $\boldsymbol{A}$-matrices, which are exactly the same as in the non-foldable element formulations. Furthermore, introducing a weak enrichment in the moment field of the $KL0$-element would have been illogical, since it would increase the order of the constant moment field interpolation to linearly varying interpolation. Introducing a weak moment field enrichment in the linear moment $KL1^{(2)}$, $KL1^{(c)}$, and $HSM^{(2)}$ elements, would presumably lead to the introduction of more enriched DOFs, as was also found in the 6 DOF beam element. Introducing more enriched DOFs may be disadvantageous, since generally the introduction of more enriched DOFs, leads to worse matrix condition numbers [31].

An additional cause of error in the foldable elements may be identified. The $KL0^{(1)}$ and $KL0^{(c)}$-elements introduce only one enriched DOF, and have a constant jump in rotation along the entire internal fold line. Since neighboring enriched elements can have different internal jumps in rotation, the edge enrichment in these neighboring elements, calculated using Equation 3.69, may differ. On the edge between neighboring enriched elements, a local strong discontinuity may thus be present, causing an *enriched edge continuity error* in the $KL0^{(1)}$ and $KL0^{(c)}$-elements. The $KL0^{(2)}$-element solves this problem by adding two enriched DOFs, placing them on the element edges, and sharing these DOFs between neighboring enriched elements. Contrary to the $KL1^{(2)}$-element, enriched DOFs are not shared between neighboring elements in the $KL1^{(c)}$-element, which is expected to introduce an enriched edge continuity error. Furthermore, since the $KL1^{(2)}$, $KL1^{(c)}$, and $HSM^{(2)}$ elements use a higher order moment field, they are expected to achieve lower errors, and higher convergence rates, than the $KL0^{(1)}$, $KL0^{(c)}$, and $KL0^{(2)}$ elements.

In this chapter, C^1-continuous moment interpolations were used, as this was suspected to result in well conditioned stiffness matrices, but investigating the $KL0^{(1)}$-element, a possible source for ill-conditioning of the stiffness matrix is found. The final stiffness matrix of the foldable element is defined as:

$$\begin{aligned}\boldsymbol{K}_{KL0^{(1)}} = \boldsymbol{B}^{\intercal}_{KL0^{(1)}}\boldsymbol{A}_c^{-1}\boldsymbol{B}_{KL0^{(1)}} + \boldsymbol{K}_T^{(1)} &= \begin{bmatrix}\boldsymbol{B}^{\intercal}_{KL0} \\ \boldsymbol{B}_c^{F(1)^{\intercal}}\end{bmatrix}\boldsymbol{A}_c^{-1}\begin{bmatrix}\boldsymbol{B}_{KL0} & \boldsymbol{B}_c^{F(1)}\end{bmatrix} + \boldsymbol{K}_F^{(1)} \\ &= \begin{bmatrix}\boldsymbol{B}^{\intercal}_{KL0}\boldsymbol{A}_c^{-1}\boldsymbol{B}_{KL0} & \boldsymbol{B}^{\intercal}_{KL0}\boldsymbol{A}_c^{-1}\boldsymbol{B}_c^{F(1)} \\ \boldsymbol{B}_c^{F(1)^{\intercal}}\boldsymbol{A}_c^{-1}\boldsymbol{B}_{KL0} & \boldsymbol{B}_c^{F(1)^{\intercal}}\boldsymbol{A}_c^{-1}\boldsymbol{B}_c^{F(1)} + K_t^{(1)}\end{bmatrix}. \qquad (3.170)\end{aligned}$$

When a fold approaches one of the element nodes, the length of the internal fold line decreases $l_F \rightarrow 0$, which also causes $\boldsymbol{B}_c^{F(1)}$ and $K_t^{(1)}$, as defined in Equations 3.93 and 3.95, to decrease, $\boldsymbol{B}_c^{F(1)} \rightarrow \emptyset$ and $K_t^{(1)} \rightarrow 0$. Due to the decrease of these sub-matrices, the stiffness matrix will converge to:

$$\boldsymbol{K}_{KL0^{(1)}} \rightarrow \begin{bmatrix}\boldsymbol{B}^{\intercal}_{KL0}\boldsymbol{A}_c^{-1}\boldsymbol{B}_{KL0} & \emptyset \\ \emptyset & \emptyset\end{bmatrix}, \qquad (3.171)$$

resulting in some of its eigenvalues decreasing to zero, which will result in an ill-conditioned stiffness matrix. The condensed $KL0^{(c)}$-element does not suffer from a similar problem, since when the internal fold length decreases to zero, the condensed element converges to a standard non-foldable $KL0$-element, as explained in Section 3.3.8. Furthermore, inspecting the stiffness matrix definitions of the $KL0^{(2)}$, $KL1^{(2)}$, and $HSM^{(2)}$ elements, they are expected to suffer from a similar problem as the $KL0^{(1)}$-element, when folds approach a standard element node, but the condensed $KL1^{(c)}$ element is expected to remain well conditioned.

4

Numerical Results

To investigate the accuracy of the $KL0^{(1)}$, $KL0^{(2)}$, $KL0^{(c)}$, $KL1^{(2)}$, $KL1^{(c)}$, and $HSM^{(2)}$ elements, their convergence behavior is examined for straight and curved folds. The convergence behavior of the elements is tested using a displacement error norm. Besides the element accuracies, their matrix condition numbers will be examined, as ill-conditioned stiffness matrices are often found in enriched FEM.

In all tests, unless stated otherwise, the material parameters shown in Table 4.1 are used.

4.1. Convergence analysis on a square plate

E $\left[\mathrm{N\,m^{-2}}\right]$	k_t $\left[\mathrm{N\,m\,rad^{-1}\,m^{-1}}\right]$	L [m]	t [m]	ν	F $\left[\mathrm{N\,m^{-1}}\right]$	P $\left[\mathrm{N\,m^{-2}}\right]$
$69 \cdot 10^9$	500	1	0.01	0.33	100	100

Table 4.1: The material parameters used in the square plate calculations throughout this chapter. Either a distributed force F is applied on side C, or a constant pressure P is applied on the entire square plate surface in Figure 4.1

To examine the foldable plate elements, an L × L square plate as shown in Figure 4.1, with material parameters as in Table 4.1, is analyzed. The plate is discretized using a structured mesh defined by N, the number of elements on one of the plate edges, resulting in a mesh with $N \times N \times 2$ triangular elements. In Figure 4.1, we use $N = 3$ to discretize the plate, resulting in $3 \times 3 \times 2 = 18$ triangular elements. Furthermore, a vertical fold is imposed at at $x = x_f$, side A is clamped and the edge rotation of sides B and D is fixed $\phi_n = 0$. Using these boundary conditions, displacements can be calculated using a clamped beam approximation. Two test cases are derived: in the first test case, a distributed force F $\left[\mathrm{N\,m^{-1}}\right]$ is applied on side C, resulting in linear moments throughout the plate. In the second test case, a pressure P $\left[\mathrm{N\,m^{-2}}\right]$ is applied on the plate surface. The convergence behavior is characterized using an error in displacement:

$$\mathbf{e} = \sqrt{\frac{\sum_{i=1}^{I}\left(w_i - w_i^h\right)^2}{\sum_{i=1}^{I} w_i^2}}, \tag{4.1}$$

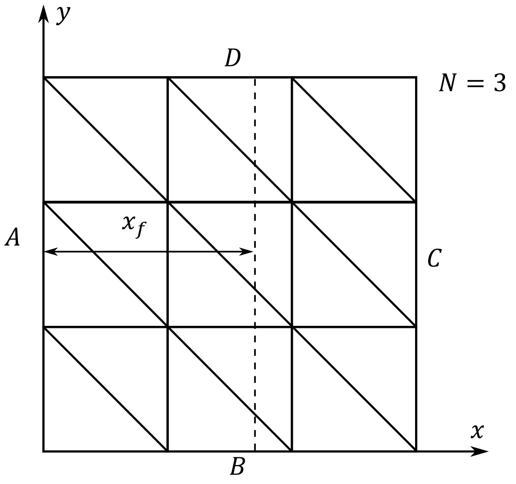

Figure 4.1: An $L \times L$ square plate with a horizontal fold at $x = x_f$ and number of border elements N. side A is clamped constraining both rotation and displacement, either a distributed force is applied on side C or a pressure is applied on its entire surface.

where I is the number of corner nodes, w_i the analytical corner node displacement, and w_i^h the FEM displacement. Because no interpolation field for the displacement in the elements is derived, the error is evaluated at the corner nodes instead of integration points. To investigate the error convergence, the logarithmic slope of the error with respect to the number of DOFs ($\#D$), is calculated as:

$$rc_{log} = \frac{\log(\mathbf{e}_2/\mathbf{e}_1)}{\log(\#D_2/\#D_1)}, \tag{4.2}$$

where $\mathbf{e}_i = \mathbf{e}(\#D_i)$.

Besides the foldable element solutions, a standard FEM solution is constructed, using the hinged $KL0$ elements as found in [13, 45]. This solution is used to analyze the difference between error behavior and condition numbers, of the foldable elements and a standard FEM solution. To implement the hinged $KL0$ elements for arbitrarily located folds, local re-meshing is applied in those elements cut by a fold, as illustrated in Figure 4.2. In this re-meshing procedure, a parent element, intersected by the imposed fold, is divided into three sub-elements on which standard $KL0$ elements are inserted. Comparing a foldable and a hinged $KL0$ solution, only one foldable element needs to be inserted on the parent element, while three $KL0$ elements are inserted on the three partitioned elements, in the hinged $KL0$ solution. Besides the three standard KL0 elements, a hinge element is inserted on the fold line, with stiffness matrix [13]:

$$\boldsymbol{K}_h \boldsymbol{u}_F = k_t \begin{bmatrix} 1 & -1 \\ -1 & 1 \end{bmatrix} \begin{bmatrix} \phi_1^F \\ \phi_2^F \end{bmatrix}, \tag{4.3}$$

where the DOFs (ϕ_1^F, ϕ_2^F) are the standard edge rotations of the $KL0$-element, located on the hinged edge, as shown in Figure 4.2.

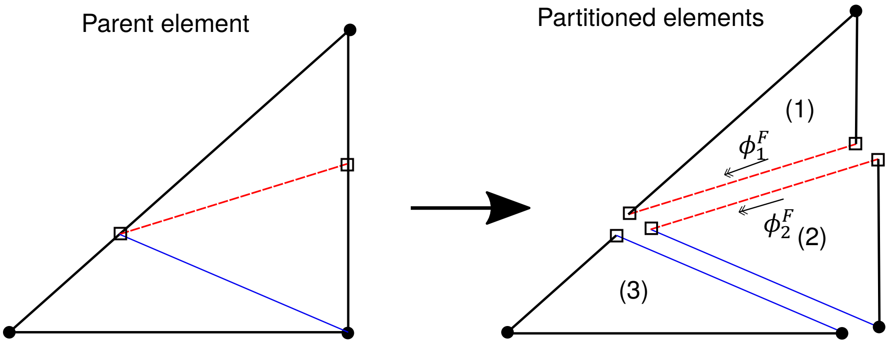

Figure 4.2: To implement the hinged KL0 element, local re-meshing is applied in those elements intersected by the fold, to split a parent element into three partitioned elements. On the parent element with three standard nodes (the round nodes), a fold line is introduced (the red dashed line), which splits the parent element into a triangle and a quadrilateral, and adds two nodes (the square nodes). The quadrilateral is triangulated by adding an element boundary (the blue line), resulting in the final three partitioned elements. On the three partitioned elements standard $KL0$ elements are inserted, furthermore a hinge element is inserted on the hinged boundary created by the fold line, to connect ϕ_1^F and ϕ_2^F.

4.1.1. Distributed edge load

Using a beam approximation, the displacement of the plate, loaded on edge C by a distributed force F, is calculated as:

$$w^{(1)}(x) = \frac{Fx^3}{3D} + \frac{F(L-x)x^2}{2D} + \begin{cases} 0 & 0 \le x \le x_f \\ \frac{F(L-x_f)(x-x_f)}{k_t} & x_f \le x \le L \end{cases}, \tag{4.4}$$

where the material parameter D is defined as:

$$D = \frac{Et^3}{12(1-\nu^2)}. \tag{4.5}$$

In Figure 4.3, the error convergence of the plate folded at $x_f = 0.5$ can be found. Since this problem contains only a linear moment filed, and a linear moment field interpolation is used in the $KL1^{(2)}$-element derivation, it finds exact solutions for this problem. However, the $KL1^{(c)}$-element does not find exact solutions, due to the enriched edge continuity error described in Section 3.4. Furthermore, the $KL1^{(c)}$-element shows a different convergence behavior than the other elements: it initially converges with $rc_{log} \approx -2$, and only towards the end converges with $rc_{log} \approx -1$. The $KL0^{(2)}$-element also has an initially higher convergence rate, but the convergence stabilizes quickly to a rate of $rc_{log} \approx -1$. All other elements have a fairly constant convergence rate of $rc_{log} \approx -1$. Although the $HSM^{(2)}$-element is also derived using linear moments, it does not yield exact solutions, this will be further elaborated on in Section 4.1.3.

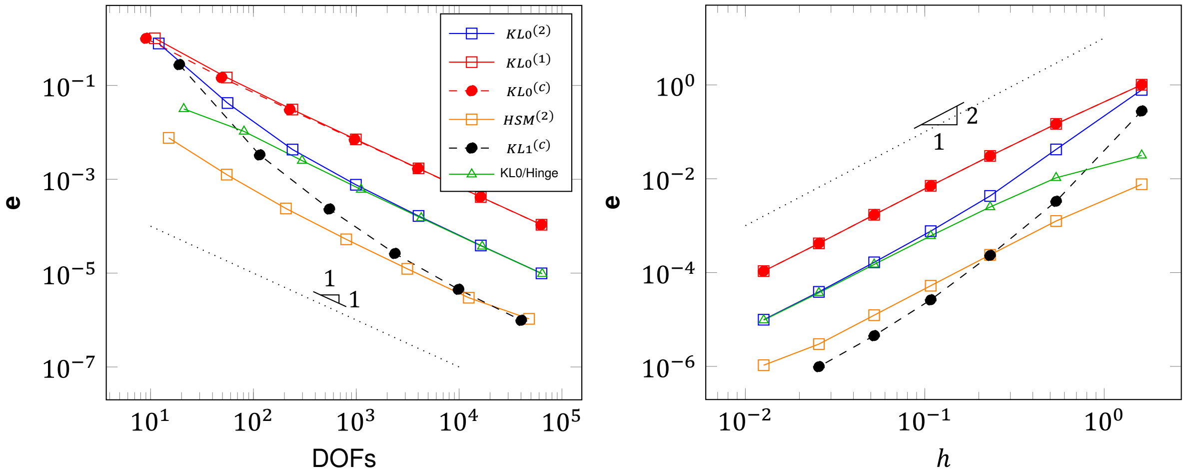

(a) The relation between displacement error and number of DOFs.

(b) The relation between displacement error and mesh size h.

Figure 4.3: The displacement error convergence using the plate in Figure 4.1 with the values in Table 4.1, the plate is simplified to a clamped beam by clamping side A and fixing the rotations of sides B and D as: $\phi_n = 0$. A fold is located at $x_f = \frac{1}{2}$, and a distributed force F $\left[\mathrm{N\,m^{-1}}\right]$ is applied on side C.

4.1.2. Distributed surface pressure

The displacement of the plate under a surface pressure P $\left[\mathrm{N\,m^{-2}}\right]$, is calculated as:

$$w^{(2)}(x) = \frac{PL(L-x)x^3}{3D} + \frac{PL(L-x)^2x^2}{4D} + \frac{Px^4}{8D} + \begin{cases} 0 & 0 \le x \le x_f \\ \frac{P(L-x_f)^2(x-x_f)}{2k_t} & x_f \le x \le L \end{cases}, \tag{4.6}$$

where the material parameter D is calculated as in Equation 4.5. The error convergence of the plate, folded at $x_f = 0.5$, can be found in Figure 4.4, all elements attain a convergence rate of $rc_{log} = -1$. With respect to the number of DOFs used, the elements can be divided into three groups with similar levels of accuracy, ranked from worst to best, they are: the $KL0^{(1)}$ and $KL0^{(c)}$ elements, the hinged $KL0$ and $KL0^{(2)}$ elements, and the $KL1^{(c)}$, $KL1^{(2)}$, and $HSM^{(2)}$ elements. Since the $KL0^{(1)}$ and $KL0^{(c)}$ elements use the same moment field interpolation, and assume a constant jump in rotation, they attain the exact same errors with respect to the element size h. In Figure 4.4a, it seems like these elements attain different errors, but this is due to the fact that the $KL0^{(c)}$-element uses less DOFs than the $KL0^{(1)}$-element.

Even though the foldable $KL1$ and HSM elements use a higher order moment field interpolation than the foldable $KL0$ elements, they attain the same convergence rate of $rc_{log} = -1$. Furthermore, a higher convergence rate is initially observed in the $KL1^{(c)}$-element, as was the case in Figure 4.3, but as the $KL1^{(c)}$-error approaches the $KL1^{(2)}$-error, the convergence rate of the $KL1^{(c)}$-element stabilizes at $rc_{log} = -1$, and the $KL1^{(2)}$ and $KL1^{(c)}$ elements attain similar displacement errors.

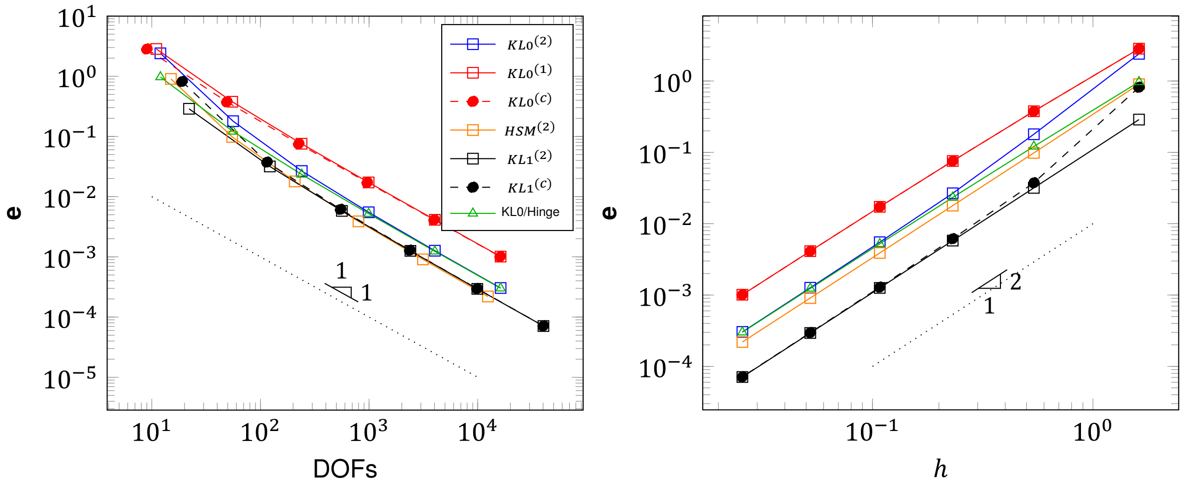

(a) The relation between displacement error and number of DOFs.

(b) The relation between displacement error and mesh size h.

Figure 4.4: The displacement error convergence using the plate in Figure 4.1 with the values in Table 4.1, the plate is simplified to a clamped beam by clamping side A and prescribing the rotations of sides B and D as: $\phi_n = 0$. A fold is located at $x_f = \frac{1}{2}$, and a distributed pressure P $\left[\mathrm{N\,m^{-2}}\right]$ is applied on the plate surface.

4.1.3. $HSM^{(2)}$-element investigation

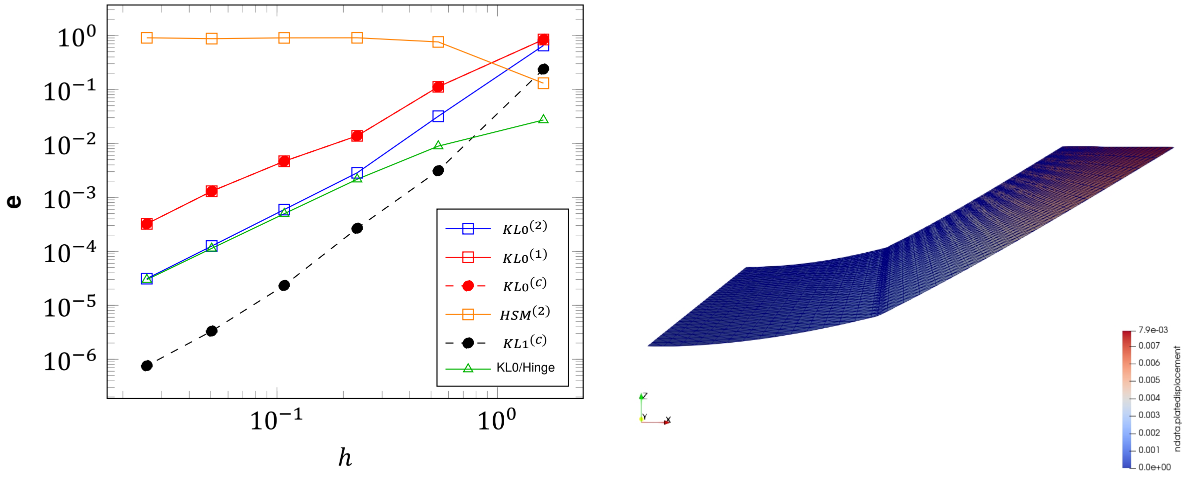

(a) The displacement error covergence for the plate, calculated using the several foladble element formulations. Using the reference solution in Equation 4.4, all elements except the $HSM^{(2)}$-element converge to the exact solution.

(b) The visualized displacement calculated using the $HSM^{(2)}$-element. Almost no folding behavior is observed and the solution is close to the solution of a non-foldable plate.

Figure 4.5: The plate in Figure 4.1, with a fold imposed at $x_f = 0.45$. A distributed force is applied on side C, side A is clamped and the rotation of sides B and D is fixed $\phi_n = 0$.

A linear moment interpolation is used in the $HSM^{(2)}$-element formulation, and only linear moments were present in the test in Section 4.1.1. The $HSM^{(2)}$-element was thus expected to achieve numerical accuracy in this test case, but did not. Furthermore, testing the solution for a fold at almost any other location than $x_f = 0.5$, a different behavior of the $HSM^{(2)}$-element is found. As shown in Figure 4.5a, the $HSM^{(2)}$ solution does not converge to the reference solution for the problem in Section 4.1.1, but with a fold imposed at $x_f = 0.45$. In Figure 4.5b the displacement of the plate, calculated using the $HSM^{(2)}$-element, is visualized; only a relatively small fold angle can be found in the solution. The fold angle, calculated using the $HSM^{(2)}$-element converges to $\Delta w_{,n} \approx 1.1 \cdot 10^{-3}$, while the analytically calculated jump in rotation is:

$$\Delta w_{,n} = \frac{M_\Gamma}{k_t} = \frac{F\left(L - x_f\right)}{k_t} = \frac{100\,(1-0.45)}{500} = 0.11\,[\text{rad}]\,. \tag{4.7}$$

Folding stiffness is thus overestimated in the $HSM^{(2)}$-element.

To further investigate the $HSM^{(2)}$-element, the displacement error is calculated for several fold locations in Figure 4.6. Using Figure 4.1, a plate is constructed using eleven border elements ($N = 11$), folds are imposed between $5/11 < x_f < 6/11$, side A is clamped, and a pressure P $\left[\mathrm{N\,m^{-2}}\right]$ is applied on the plate surface. Only when the fold is located at the center of the plate ($x_f = 0.5$) does the $HSM^{(2)}$-element achieve accurate solutions. The error of the $HSM^{(2)}$-element could be an implementation error, to verify that this is not the case, a non-folded plate is analyzed. The square plate in Figure 4.1 is used to test the non-foldable HSM-element, side A is clamped, the rotations of sides B and D are fixed, and a distributed force F is applied on side C, but no fold is imposed. A non-folded analytical solution is constructed as:

$$w^{(3)}(x) = \frac{Fx^3}{3D} + \frac{F(L-x)x^2}{2D}, \tag{4.8}$$

resulting in the error convergence in Figure 4.7, where the non-foldable standard HSM-element converges as expected. Furthermore, the fault in the $HSM^{(2)}$-element can not be attributed to the enriched implementation, since the $HSM^{(2)}$ and $KL1^{(2)}$ elements use the exact same enriched matrices and implementation, and no large errors are found in the $KL1^{(2)}$-element. It is concluded that the fault in $HSM^{(2)}$-element is not due to a fault in its implementation. For the remainder of this thesis the $HSM^{(2)}$-element will be omitted from the results.

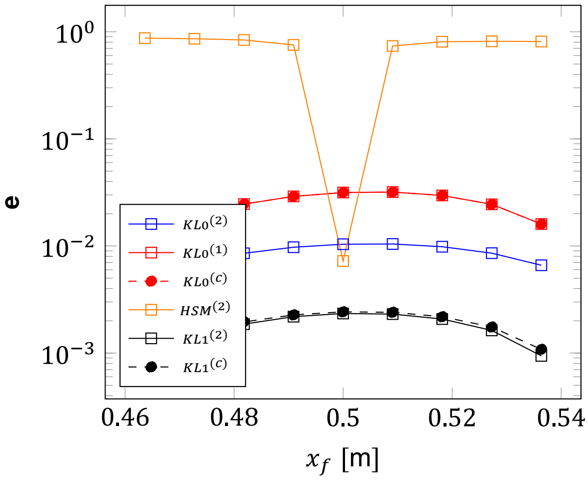

Figure 4.6: The displacement error of the folded plate with a pressure applied on its surface. Using Figure 4.1, a mesh is created with 11 edge elements ($N = 11$), and folds are imposed between $\frac{5}{11} < x_f < \frac{6}{11}$. Only for a fold located at the center of the plate does the $HSM^{(2)}$-element achieve accurate results.

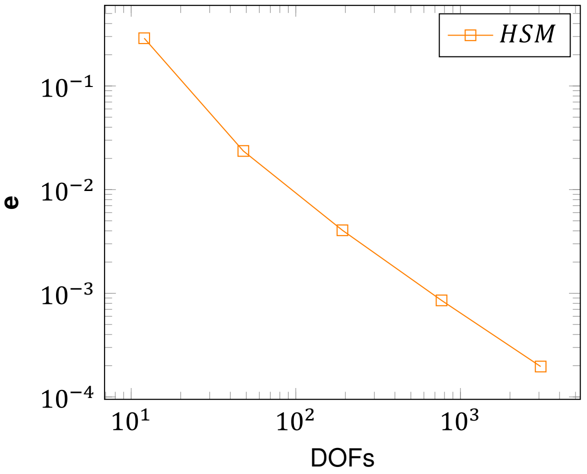

Figure 4.7: The displacement error of the plate in Figure 4.1 with a distributed force F applied on Side C, side A is clamped, and the rotation of sides B and D are fixed $\phi_n = 0$. No fold is implemented in the plate and the convergence is calculated using the non-foldable standard HSM-element.

An explanation for the error in the $HSM^{(2)}$-element is found in [39]; in a non-enriched plate element with linear moments, 9 independent generalized stresses are introduced, represented by the 9 components of $\boldsymbol{\beta}_9$ in the $HSM^{(2)}$ and $KL1^{(2)}$ derivation. The 9 generalized stresses are energetically conjugated to 9 generalized deformations. Adding the three rigid body modes of a plate to the 9 deformations $9 + 3 = 12$ DOFs are needed to accurately model a non-folded linear moment plate. Using less DOFs than deformation modes, may lead to overestimated element stiffness [39]. In the foldable HSM and $KL1$ elements, 2 extra modes of deformation are imposed on the plate; a constant jump in rotation at the fold, and a linearly varying jump in rotation at the fold. To accurately represent a foldable linear moment plate, $9+2+3=14$ DOFs are needed. The $KL1^{(2)}$-element introduces these 14 DOFs, but the $HSM^{(2)}$-element introduces only 11 DOFs. Introducing less DOFs than needed, not all modes of deformation can accurately be represented, and the folding stiffness is overestimated.

4.1.4. Tilted fold convergence

To test problems of a higher complexity, the plate in Figure 4.8 is used, where a tilted fold is imposed on the plate at $x_f = 0.71 - 0.5x$, a distributed force F is applied on side C, but the rotation of sides B and D is not fixed $\phi_n \neq 0$. Poisson effect will be present in the plate, because $\phi_n \neq 0$ on sides B and D, an analytical solution can thus not be made using a beam approximation. Since constructing an analytical solution for a square plate with an imposed tilted fold is a fairly cumbersome process, a reference solution is constructed using hinged $KL0$-elements on a reference mesh. Figure 4.9 illustrates the construction of a reference mesh, and two convergence meshes, such that all corner nodes in the convergence meshes overlap with a corner node in the reference mesh. In the figure, two convergence meshes are defined by $N_c = 1, 2$, and one reference mesh is defined by $N_{ref} = 4$, where N_c and N_{ref} are the amount of elements on one of the square plates edges. By defining the convergence mesh and reference mesh such that $N_{ref} = 2^p N_c$ is always valid for some $p \in \{1, 2, 3, ...\}$, the corner nodes overlap, and the displacement at the corner nodes in the reference mesh can be used as a reference solution (w_i), to compute the displacement error in Equation 4.1.

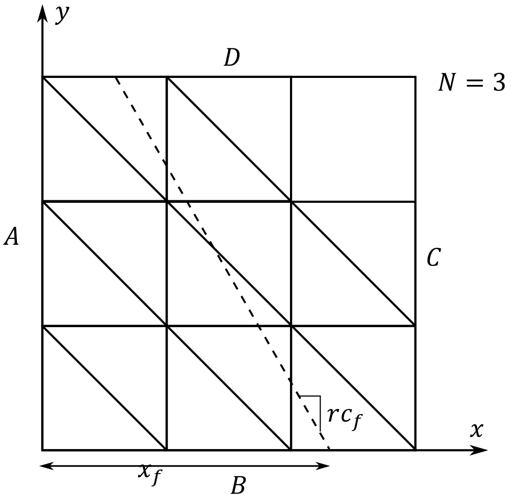

Figure 4.8: A square plate, discretized using N elements on each of its edges, resulting in a total of $N \times N \times 2$ triangular elements. A tilted fold is impose on the plate at $x = x_f - rc_f * x$. Side A is clamped and a distributed force F is applied on side C.

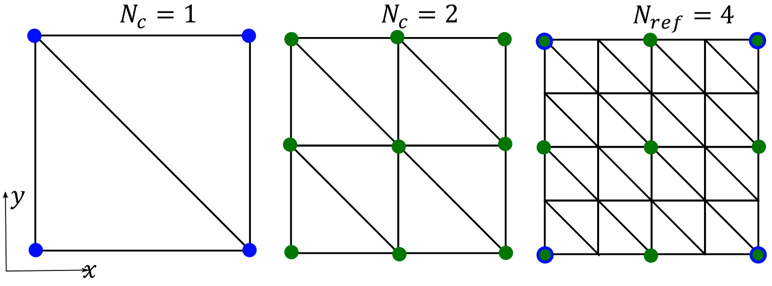

Figure 4.9: An example of the construction of convergence and reference meshes. Two convergence meshes are constructed using $N_c = 1, 2$, and one reference mesh is constructed using $N_{ref} = 4$. All corner nodes of the convergence mesh, constructed using $N_c = 2$ (depicted as green dots), overlap with some of the corner nodes in the reference mesh (depicted as green dots). Furthermore, all corner nodes of the reference mesh constructed using $N_c = 1$ (depicted as blue dots) overlap with some of the corner nodes of the reference mesh (the dots with blue borders).

To test the square plate in Figure 4.8, a reference mesh is defined by $N_{ref} = 256$, and convergence meshes are defined by $N_c = 1, 2, 4, 8, 16, 32, 64, 128$, resulting in Figure 4.10. Although the displacement error of the $KL1^{(2)}$-element remains lower than the error of all other foldable elements, the convergence rate is decreased to $rc_{log} \approx -0.76$. All foldable $KL0$-elements and the $KL1^{(c)}$-element are still found to converge with $rc_{log} \approx -1$. Contrary to the previous tests, the $KL0^{(2)}$ and hinged $KL0$ solutions do not converge to similar errors, as the hinged $KL0$ solution achieves a slightly lower error. A visual representation of the displacement can be found in Figure 4.11, most displacement in the plate is due to the jump in rotation on the fold line. An inaccurate jump in rotation will thus lead to large errors in displacement, and the displacement error is dominated by the calculation of the jump in rotation. In Appendix F, several other test cases are investigated where several other straight folds are imposed on the square plate.

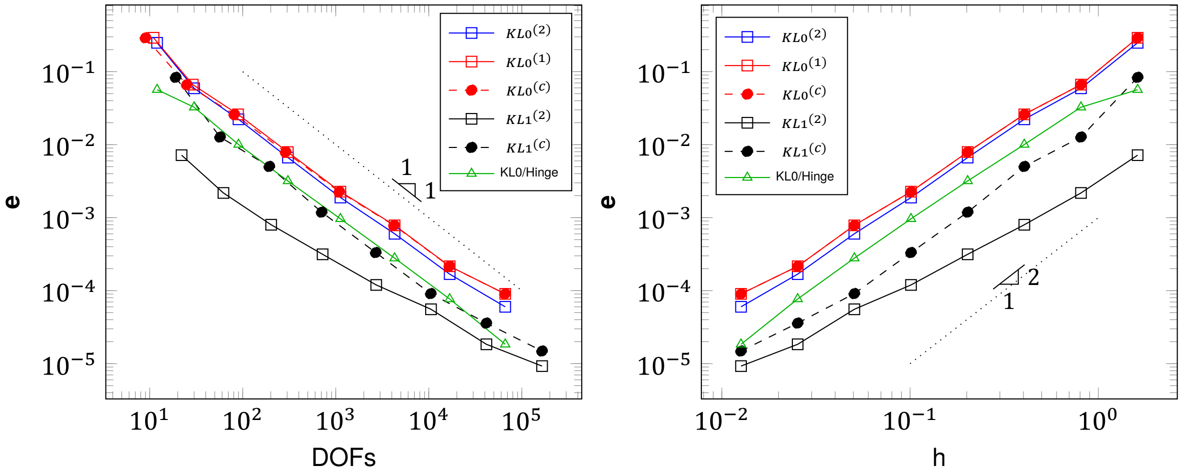

Figure 4.10: The displacement error of the folded plate in Figure 4.8 using a hinged KL0 element with $N_{ref} = 256$ as reference solution. Besides the convergence of the enriched $KL0$ and $KL1$ elements the convergence of the hinged $KL0$-element to its own reference mesh solution is calculated. As test parameters the values in Table 4.1 are used, side A is clamped and the distributed force is applied on side C. The fold is imposed at $x_f = 0.71 - 0.5y$. A visual representation of the displacement can be found in Figure 4.11.

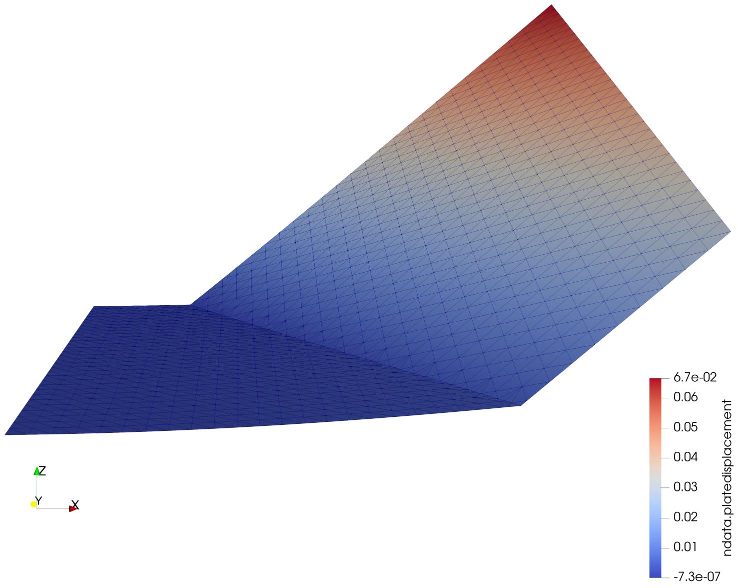

Figure 4.11: The displacement of the plate in Figure 4.1, constructed using $N_c = 32$. A fold is imposed at $x_f = 0.71 - 0.5x$, and a distributed force is applied on the right edge. The fold is modeled using the $KL1^{(2)}$-element.

4.2. 2D matrix condition

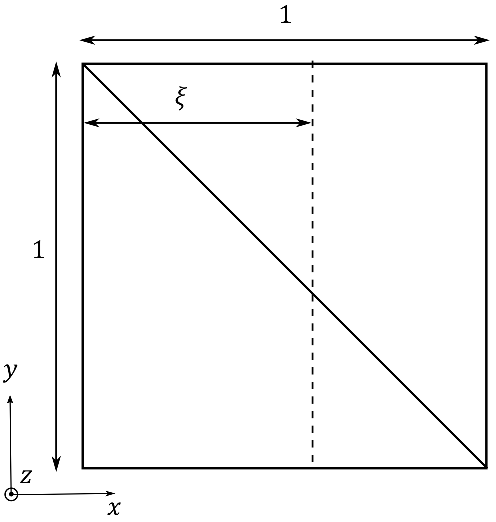

Figure 4.12: Two plate elements, folded by a vertical crease at varying locations ξ.

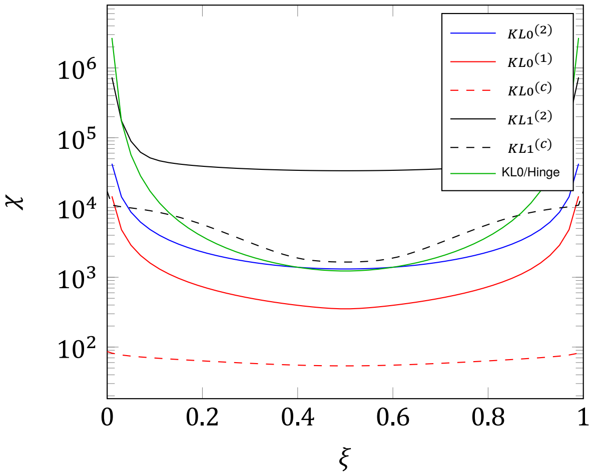

Figure 4.13: The matrix condition for all foldable elements. No precondition matrix is applied to improve condition number. The condition numbers of the condensed systems are bounded and can be evaluated at $\xi = 0$ and $\xi = 1$, the condition of all other foldable elements is unbounded and not evaluated at $\xi = 0$ and $\xi = 1$.

The condition number of the assembled $KL0$ hinge, enriched, and condensed $KL0$ and $KL1$ elements, are evaluated using the problem in Figure 4.12, and the parameters in Table 4.1. The condition number is computed as:

$$\chi = \frac{\lambda_{max}}{\lambda_{min}}, \tag{4.9}$$

where λ_{max} is the highest eigenvalue and λ_{min} the lowest non-zero eigenvalue of the stiffness matrix. As can be seen in Figure 4.13, the matrix condition number of the condensed systems remains fairly constant for folds in the entire element domain. In fact, the condition number of the condensed elements is bounded, and at $\xi = 0$ and $\xi = 1$, the condition numbers of the $KL0^{(c)}$ and $KL1^{(c)}$ elements are 86.3 and 17051 respectively. In all other element formulations, the matrix condition number is unbounded for folds approaching $\xi = 0$ or $\xi = 1$. The $KL1^{(2)}$ element has the highest condition number over the largest part of the element domain, but the condition number for folds close to element boundaries is of main concern, as it is unbounded. Investigating the condition close to $\xi = 0$ the hinged KL0 solution performs worst, followed by the $KL1^{(2)}$, $KL0^{(2)}$, $KL0^{(1)}$, $KL1^{(c)}$ and $KL0^{(c)}$ elements.

The hinged KL0 solution is basically a standard FEM solution, where a fold is imposed on the mesh by partitioning elements into sub-elements, as described in Figure 4.2. Following this procedure, relatively small standard $KL0$ elements will be inserted in the mesh for folds approaching $\xi = 0$ or $\xi = 1$, causing an ill-conditioned stiffness matrix. Furthermore, investigating the cause of ill-conditioning in the $KL1^{(2)}$, $KL0^{(2)}$, and $KL0^{(1)}$ elements, their highest eigenvalues are found to remain fairly constant, while their lowest eigenvalues are found to rapidly decrease, causing the increase in condition number. The decreased eigenvalues may be caused by the enriched $\boldsymbol{B}$-matrices converging to zero $\boldsymbol{B}_E \rightarrow \emptyset$, as anticipated in Section 3.4. Inspecting the enriched $\boldsymbol{B}$-matrix of the two elements in Figure 4.12, it is found that the enriched $\boldsymbol{B}$-matrix of the upper right triangle decreases to zero for $\xi \rightarrow 0$, and the enriched $\boldsymbol{B}$-matrix of the lower left triangle converges to zero for $\xi \rightarrow 1$. In both elements, the enriched $\boldsymbol{B}$-matrix thus decreases when the fold approaches one standard element node, causing an increase in matrix condition number due to a decrease of the lowest non-zero eigenvalue.

To improve the matrix condition of the foldable elements, a preconditioner is used as:

$$\boldsymbol{K}' = \boldsymbol{PKP}, \tag{4.10}$$

where the precondition matrix is defined as:

$$P_{ij} = \frac{\delta_{ij}}{\sqrt{K_{ij}}}. \tag{4.11}$$

Using the this preconditioner, condition numbers are found as in Figure 4.14, the condition of the non-condensed foldable elements is significantly improved. On the non-condensed elements, no preconditioner can be applied for folds crossing standard nodes at $\xi = 0$ or $\xi = 1$. For these folds, diagonal terms related to the enriched DOFs became zero, and the preconditioner could not be computed. The condition number of the condensed elements is also improved, but since the condensed elements already have bounded condition numbers, using a preconditioner is not strictly necessary.

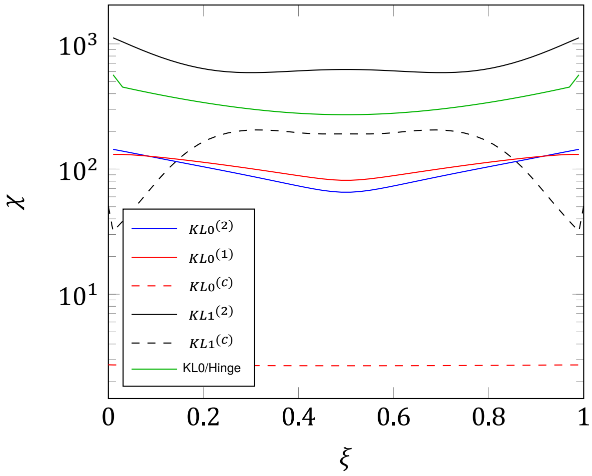

Figure 4.14: The matrix condition calculated using Figure 4.12, improved using the preconditioner in Equation 4.11. The condition number of the condensed systems is bounded and evaluated at $\xi = 0$ and $\xi = 1$, the condition of all other foldable elements is unbounded and could not be evaluated at $\xi = 0$ and $\xi = 1$.

To calculate the condition numbers upon mesh refinement, the plate as shown in Figure 4.1 is used with a fold located at $x_f = 0.5$, where the mesh is refined by increasing N, the number of elements located on an edge. In Figure 4.15, all elements are found to have a fairly constant increase in condition number. In this test, the mesh and fold line are constructed such that the enriched elements achieve their optimal condition number (as found at $\xi = 0.5$ in Figure 4.13), Figure 4.15 is thus used as a base-line for folds causing ill-conditioning.

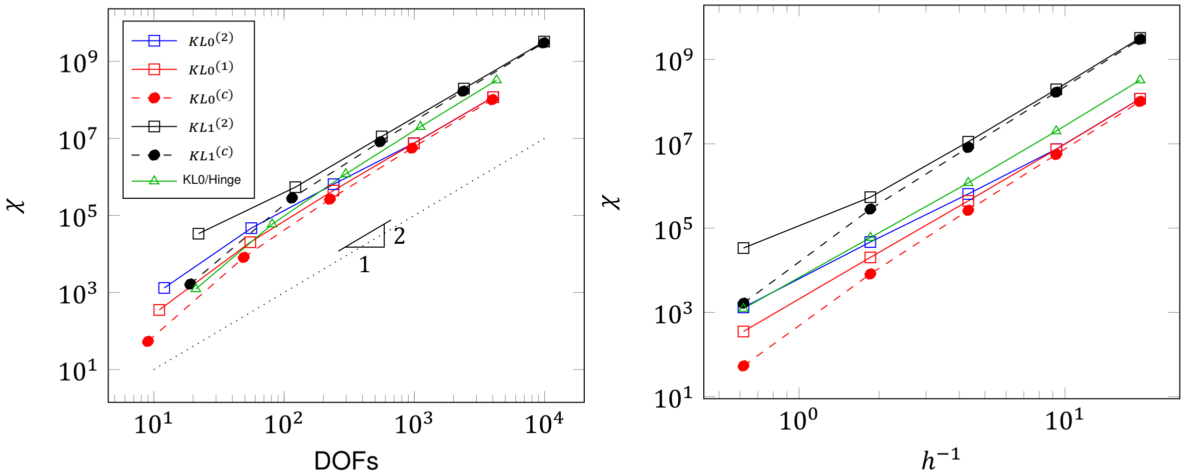

Figure 4.15: The matrix condition upon increasing N, the number of edge elements in the problem in Figure 4.1. A fold is located at $x_f = 0.5$, this causes the fold to intersect all elements at the optimal location for condition number ($\xi = 0.5$ in Figure 4.12). No preconditioner is applied to improve matrix condition.

To introduce ill-conditioned elements to the mesh refinement, the plate in Figure 4.8 is used, where no boundary conditions are applied, and a fold is introduced at:

$$x_f = 0.41 + 0.2y, \tag{4.12}$$

which results in Figure 4.16. Upon mesh refinement, the tilted fold may approximate standard nodes in certain elements, resulting in an ill-conditioned stiffness matrix. The hinged $KL0$ solution is the first to attain a significant increase in condition number with respect to Figure 4.15, while in all foldable elements, only a slight increase of condition number is found.

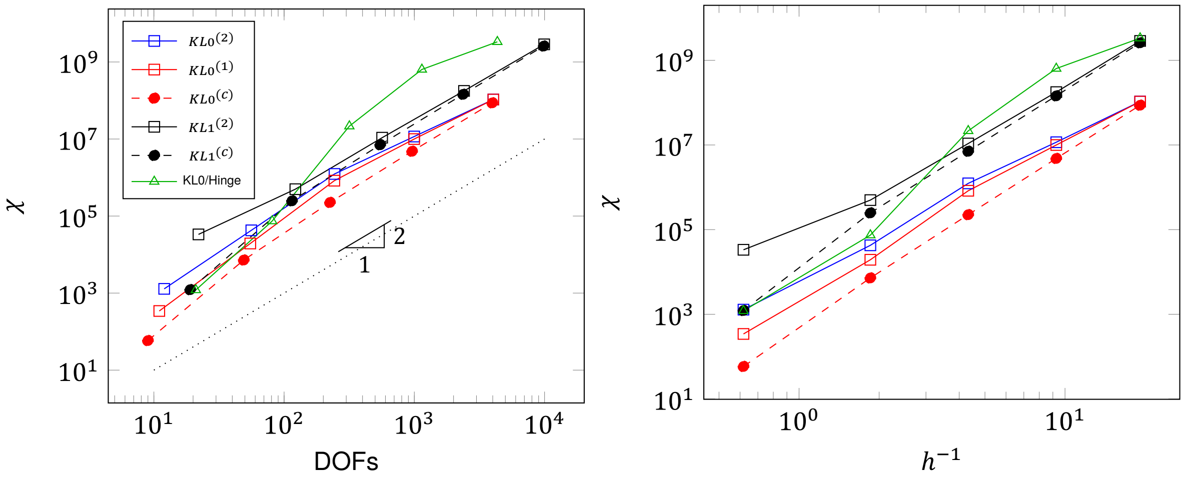

Figure 4.16: The matrix condition upon increasing N, the number of edge elements in the problem in Figure 4.8. The fold is located at $x_f = 0.41 + 0.2y$, and no preconditioner is applied to improve matrix condition.

To introduce a further increase in condition number, on the plate in Figure 4.8, a fold is imposed at:

$$x_f = 0.334 + 0.333y, \tag{4.13}$$

which results in Figure 4.17. Almost all stiffness matrices rapidly become ill-conditioned, and only the condensed elements remain well-conditioned. As expected from Figure 4.13, the hinged $KL0$ solution attains the highest condition numbers.

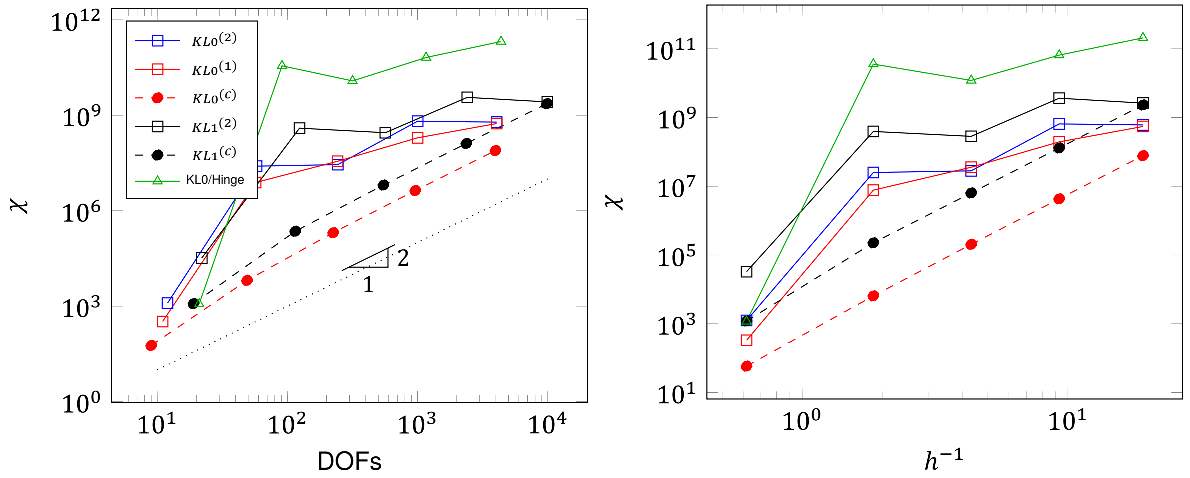

Figure 4.17: The matrix condition upon increasing N, the number of edge elements in the problem in Figure 4.8. The fold is located at $x_f = 0.334 + 0.333y$, and no preconditioner is applied to improve condition numbers.

To improve the condition numbers of the problem in Figure 4.17, the preconditioner as in Equation 4.11 is applied, resulting in Figure 4.18. The condition number of all foldable formulations is improved, and while the largest improvements can be found for the hinged $KL0$, $KL0^{(2)}$, $KL0^{(1)}$, and $KL1^{(2)}$ elements, a slight improvement is also found for the condition numbers of the $KL0^{(c)}$ and $KL1^{(c)}$ elements.

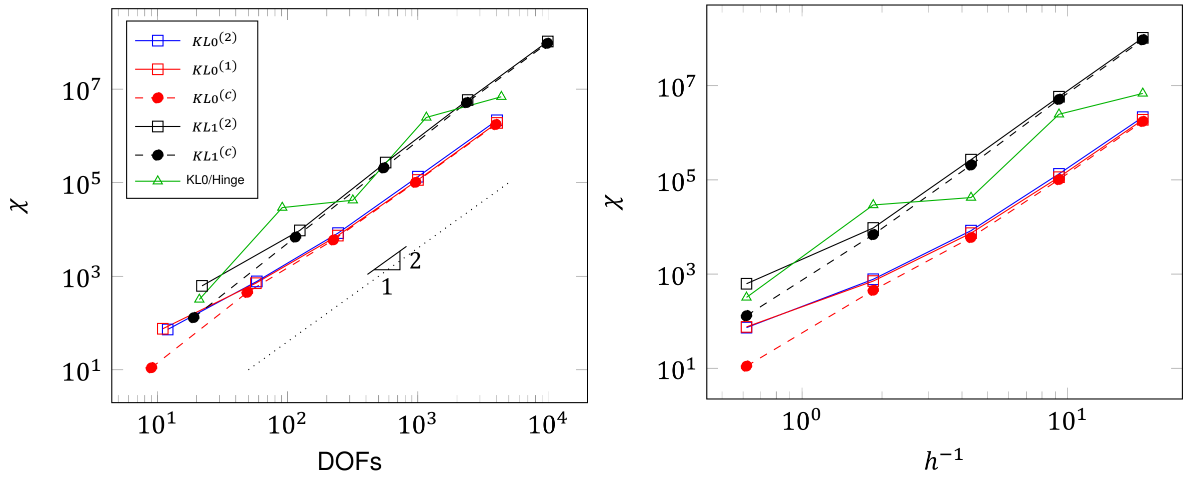

Figure 4.18: The matrix condition upon increasing N, the number of edge elements in the problem in Figure 4.8. The fold is located at $x_f = 0.334 + 0.333y$ and the condition is improved using the preconditioner as defined in Equation 4.11.

4.3. Curved fold convergence

E [N m^{-2}]	k_t [N m rad^{-1} m^{-1}]	h [m]	ν	R [m]	R_F [m]	q [N m^{-2}]
$69 \cdot 10^9$	500	0.01	0.33	2	1.5	-100

Table 4.2: Parameters used for the plate in Figure 4.19, and to derive the analytical solution in Equations 4.14, **??**.

Via a similar approach as in [22], curved folds can be modeled by making piecewise linear approximations of the fold; within each element, a linear fold segment is created between the two enriched nodes, located at the intersections of the element edge and fold. Using no addition to the folded element formulation, it should thus be possible to model curved folds. A test for modeling curved folds is described in Figure 4.19. The test consists of a plate of radius $R = 2$ m, which is clamped at its outer edge, on which a pressure $q = -100$ N m^{-2} is applied, and a circular fold with a radius $R_F = 1.5$ m is imposed.

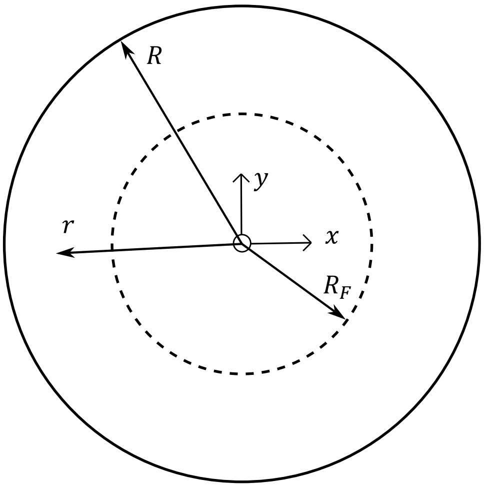

Figure 4.19: A circular plate with radius R on which a circular fold with radius R_F is imposed. The plate is clamped on its outer edge, a pressure is applied on its entire surface, and the material parameters in Table 4.2 are used.

Starting from the equations found in [46], an exact analytical solution is derived in Appendix G. The symbolic expression for the displacement function is quite lengthy, and thus not displayed in this thesis. Using the material parameter in Table 4.2, the exact solution for the displacement field is found as:

$$w^-(r) = \frac{qr^4}{64D} + \frac{0.01057r^2}{4} - 0.00525, \; 0 \le r \le R_F, \tag{4.14}$$

$$w^+(r) = \frac{qr^4}{64D} + \frac{0.00923r^2}{4} + -0.00297 \ln r - 0.00330, \; R_F < r \le R \tag{4.15}$$

Figures 4.20 and 4.21, show the deformed circular plate, in the outer ring, where $R_F < r < R$, relatively small displacement is found. Furthermore, in Figure 4.20, a jump in rotation can clearly be seen at the fold, causing relatively large displacements in the inner folded circle where $r < R_F$.

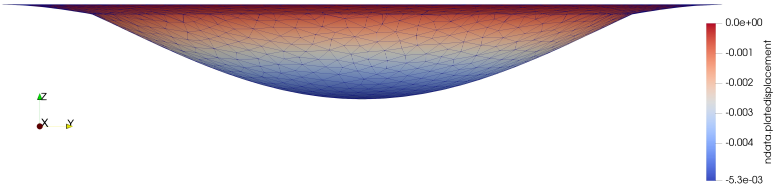

Figure 4.20: The scaled displacement of the circular folded plate in Figure 4.19, calculated using the $KL1^{(2)}$-element on a mesh defined by mesh size $h = 0.125$.

In Figure 4.22, the displacement error convergence for curved folds is shown, the foldable $KL0$ elements perform quite well with a relatively constant convergence rate of $rc_{log} = -1$. Although the foldable $KL1$ elements achieve the lowest error, their convergence rate is not stable; the $KL1^{(c)}$-element initially converges with a rate of $rc_{log} \approx -1$, but the rate slowly decreases when more DOFs are used. Furthermore, the $KL1^{(2)}$-element has an initial slow convergence rate, which increases when the $KL1^{(2)}$-error approaches the $KL1^{(c)}$-error, but decreases again when more DOFs are used.

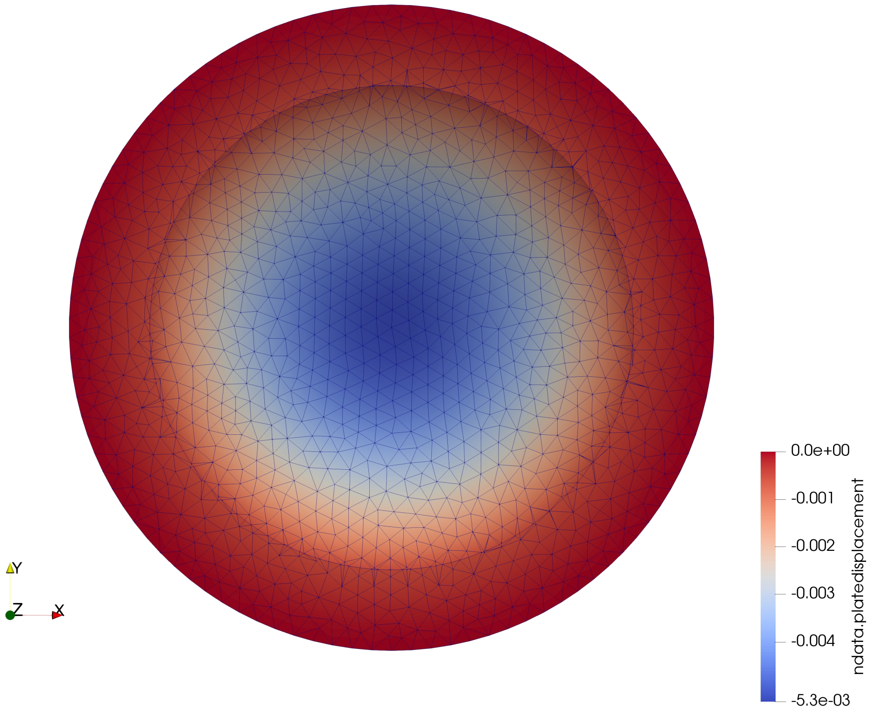

Figure 4.21: The displacement of the circular folded plate in Figure 4.19, calculated using the $KL1^{(2)}$-element on a mesh defined by mesh size $h = 0.125$.

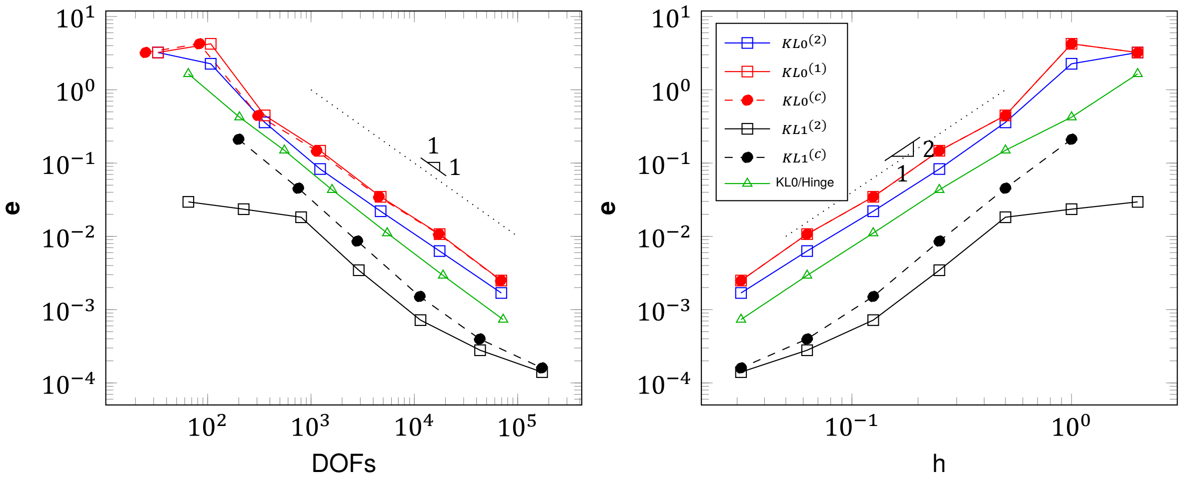

Figure 4.22: The displacement error of the circular plate in Figure 4.2 with the material parameters in Table 4.2, the foldable $KL0$ elements achieve relatively stable convergence rates, while the convergence rate of the foldable $KL1$ elements slowly decreases.

An explanation for the convergence behavior of the foldable $KL1$ elements, is found using Figure 4.23, where: a curved fold, the linear approximation of the curved fold, the vectors representing the enriched DOFs ($\Delta w_{,n}^{F(1)}$, $\Delta w_{,n}^{F(2)}$) and their orientation ($\theta^{(1)}$, $\theta^{(2)}$), and the actual jump in rotation $\Delta w_{,n}^{F}$ are displayed. Since the linear fold segments are not aligned, the enriched DOFs ($\Delta w_{,n}^{F(1)}$, $\Delta w_{,n}^{F(2)}$) are not aligned with the actual jump in rotation $\Delta w_{,n}^{F}$, which introduces an enriched edge continuity error. When the two elements are assembled, we impose $\Delta w_{,n}^{(1)} = \Delta w_{,n}^{(2)} = \Delta w_{,n}^{(A)}$, and the edge enrichment in the two neighboring elements is calculated as:

$$w_E^{(1)}(\eta) = \Delta w_{,n}^{(A)} \cos\left(\theta^{(1)}\right) \Psi(\eta) \neq \Delta w_{,n}^{(A)} \cos\left(\theta^{(2)}\right) \Psi(\eta) = w_E^{(2)}(\eta). \tag{4.16}$$

Due to the two different orientation of the linear fold segments ($\theta^{(1)} \neq \theta^{(2)}$), the displacement enrichment of the two neighboring elements is not equal, causing an additional continuity error. Furthermore, since there is no contribution of the edge enrichment to the stiffness matrix in the foldable $KL0$-element formulations, they are not influenced by this error.

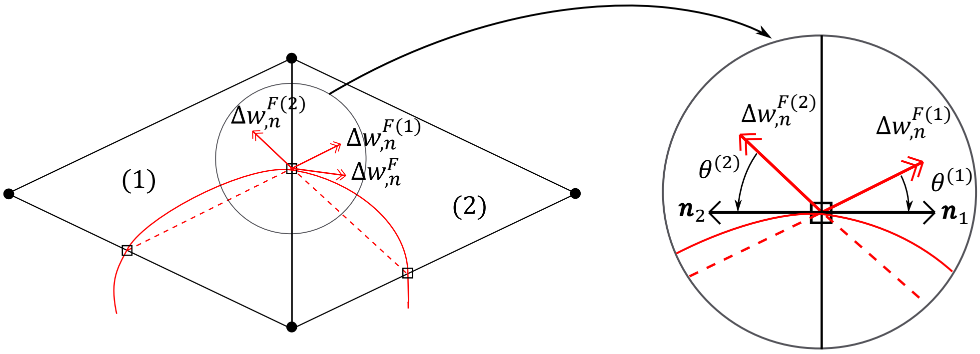

Figure 4.23: Two triangular elements cut by a curved fold (red) which is interpolated as two linear fold segments (dashed). At the shared boundary of the two elements, the DOFs representing the jump in rotation in the two elements ($\Delta w_{,n}^{F(1)}$, $\Delta w_{,n}^{F(2)}$) are not aligned with the real tangential vector representing the jump in rotation ($\Delta w_{,n}^{F}$).

5

Discussion and conclusions

This thesis was aimed at developing methods for accurate and flexible origami modeling. Adopting an enriched mixed/hybrid formulation, interpolation functions for the moment field were used, which imposed less continuity constraints in Kirchhoff-Love plate elements. Six foldable plate elements were derived; three foldable constant moment elements ($KL0^{(1)}$, $KL0^{(c)}$, $KL0^{(2)}$), and three foldable linear moment elements ($KL1^{(2)}$, $KL1^{(c)}$, $HSM^{(2)}$). This work should be seen as a first step towards enriched origami modeling. However, in realistic origami problems, changes in director field and membrane stresses will be present. Since the foldable elements, derived in this thesis, do not take these effects into account, they are not yet suited for origami modeling.

5.1. Discussion

5.1.1. Foldable beam derivation

In Chapter 2, enriched mixed/hybrid FEM was investigated in the context of origami modeling, by deriving foldable beam elements. A modified potential energy equation was formulated, where kinematic equations were imposed on a potential energy equation via Lagrange multipliers. Subsequently, the Lagrange multipliers were interpreted via virtual variations of the potential energy equation. Besides the standard Euler-Bernoulli kinematic relations, imposed on the subdomains of the beam, kinematic relations were imposed on the fold to guarantee C^0-continuity. In the derivation, either an externally applied force at the fold F_Γ could be introduced, resulting in an enriched C^0 continuous moment field, or F_Γ could be excluded from the derivation, resulting in an unenriched C^1-continuous moment field. Implementing a weak moment field enrichment in the discretization, a DOF representing the displacement at the fold w_Γ needed to be added to the foldable element. Two foldable beam elements were thus derived; the 6 DOF beam, including w_Γ and an enriched moment field, and the 5 DOF beam, excluding w_Γ and using no moment field enrichment.

Both the 5 and 6 DOF beam elements achieved exact results for a linear reference solution. Furthermore, the 6 DOF beam was found to have significantly worse condition numbers than the 5 DOF beam. Whereas the 5 DOF beam achieved relatively constant and bounded condition numbers, the condition numbers for the 6 DOF beam were unbounded for folds approaching standard element nodes. Following the IGFEM procedure to improve matrix condition [11], a scaling parameter was introduced to the moment field enrichment in the 6 DOF beam element. Unfortunately, this did not change matrix condition numbers. Implementing a Jacobi preconditioner, the 6 DOF beam condition numbers could be significantly improved, and similar condition numbers as in the 5 DOF beam element were observed. To reduce the amount of DOFs and further improve matrix condition of the 5 DOF foldable beam, it was condensed to a 4 DOF foldable beam; the condensation may be seen as an extension of the mixed/hybrid formulation where, besides a moment field, a folded rotational field is imposed on the system. The 4DOF beam had better condition numbers than the 5 DOF beam, and the 5 DOF beam had better condition numbers than the 6 DOF beam, which indicates that using less enriched DOFs may cause improved condition numbers, as also found for the cracked plates in [31].

An advantage of the 6 DOF beam over the 5 DOF beam, was the fact that using the 6 DOF beam a force F_Γ could easily be applied at the fold, while this was more challenging in the 5 DOF beam. F_Γ was applied on the 5 DOF beam via the relatively complex work-equivalent load vector, derived in Appendix B, and both the 5 and 6 DOF foldable elements, were found to achieve accurate results, when loaded by a force at the fold. An advantage of the 5 DOF beam over the 6 DOF beam, is its ability to accurately model problems where a fold is located exactly at a standard element node, whereas in the 6 DOF beam, certain terms of the stiffness matrix grow to infinity for these folds, and the stiffness matrix becomes uninvertible. As the 5 DOF beam element used less DOFs and had excellent condition numbers, it was chosen to derive the foldable plate elements using a C^1-continuous non-enriched moment field interpolation, by foregoing the application of a force on the fold in the modified potential energy derivation.

5.1.2. Constant moment plates

Firstly, two non-condensed foldable elements were defined; the $KL0^{(1)}$-element, which adds only one enriched DOF, and the $KL0^{(2)}$-element, which adds two enriched DOFs. Since a constant moment field was used, the bending energy in the fold could be evaluated using a constant jump in rotation, resulting in only one enriched DOF located at the center of the internal fold line. However, this DOF could not be shared between neighboring enriched elements, causing a difference of the jump in rotation on the shared folded element edges, and thus an enriched edge continuity error. To fix the enriched edge continuity error, the $KL0^{(2)}$-element was derived which adds two DOFs to the $KL0$-element, one per enriched node, such that enriched DOFs could be shared between neighboring elements. Although an enrichment function for the displacement field was defined on the element edge of both elements, it did not contribute to the stiffness matrix, due to the constant moment in the plate. To improve matrix condition number, the $KL0^{(1)}$-element was condensed locally, before assembly into the global stiffness matrix, resulting in the $KL0^{(c)}$-element. Since the $KL0^{(1)}$-element contained the enriched edge continuity error, it is assumed that the $KL0^{(c)}$-element would also contain this error. Moreover, as condensing the $KL0^{(2)}$ and $KL0^{(1)}$ elements resulted in the same $KL0^{(c)}$-element, local condensation thus introduced an enriched edge continuity error, when applied on the $KL0^{(2)}$-element. To allow a comparison with a standard FEM solution, the hinged $KL0$ solution was constructed by local re-meshing of parent elements into sub-elements, and implementing hinged $KL0$ elements as in [13, 45].

As shown in Chapter 4, all foldable $KL0$ elements, and the hinged $KL0$ solution, were found to achieve an error convergence of $rc_{log} = -1$, for all tests including straight or curved folds. The $KL0^{(1)}$ and $KL0^{(c)}$ elements achieved the exact same errors with respect to the mesh size, due to both elements having an enriched edge continuity error. Since the $KL0^2$-element does not contain this error, it achieved slightly lower errors. In the simple test cases in Sections 4.1.1 and 4.1.2, where a beam approximation could be used as a reference solution, the $KL0^{(2)}$-element converged to similar errors as the hinged $KL0$ solution. However, in the more complex test cases for a tilted fold in Section 4.1.4 and for a curved fold in Section 4.1.4, the hinged $KL0$ solution achieved slightly lower errors than the $KL0^{(2)}$ solution. Since the hinged $KL0$ solution implemented three partitioned elements, with separate moment fields, around the fold, it was able to accurately capture the complex moment field around the fold. Contrarily, the foldable $KL0$ solutions only implemented one element with one constant moment on the fold, and could thus less accurately capture the moment field around the fold, resulting in a slightly higher error.

Whereas, in terms of error, the hinged $KL0$ solution performed best of all constant moment elements, it attained the highest and unbounded condition numbers, as shown in Figure 4.13. The $KL0^{(1)}$ and $KL0^{(2)}$ elements performed better in terms of condition, but also had unbounded condition numbers. A great improvement in condition number was found in the $KL0^{(c)}$-element, which had the lowest and bounded condition numbers. As explained in Section 3.3.8, the only change in the $KL0^{(c)}$-element with respect to the standard $KL0$ element, is an addition to the $\boldsymbol{A}$-matrix. Furthermore, when a fold approximated one standard node, this addition converged to zero, and the condensed element became a standard well conditioned non-foldable $KL0$-element, resulting in the bounded condition numbers of the $KL0^{(c)}$-element. Using a simple Jacobi precondition matrix, the condition numbers of the hinged $KL0$ solution, the $KL0^{(1)}$, and the $KL0^{(2)}$ elements could be greatly improved, as shown in Figure 4.14. The condition numbers of the $KL0^{(c)}$-element were also improved by applying the precondition matrix, but as the element already achieved low and bounded condition numbers, an improvement is not necessary.

5.1.3. Linear moment plates

Besides the three foldable constant moment elements, three foldable linear moment elements have been derived: the $KL1^{(2)}$, $KL1^{(c)}$, and $HSM^{(2)}$ elements. An enrichment function for the displacement field on the element boundaries was constructed, such that it contained a constant jump in derivative at the discontinuity. Due to the linear moment field used in these elements, the displacement field enrichment did contribute to the stiffness matrix. The $KL1^{(c)}$-element was constructed by local condensation of the $KL1^{(2)}$-element, which introduced an enriched edge continuity error in the $KL1^{(c)}$-element, as enriched DOFs could not be shared between neighboring elements. The enrichment procedure was mostly dependent on the moment field interpolation, and since the standard $KL1$ and HSM elements used the same moment field interpolations, the enrichment procedures of the $KL1$ and HSM elements were exactly the same.

It was expected that the linear moment elements would have better convergence behavior than the constant moment elements. However, this was not the case. When a distributed pressure was applied on the plate in Section 4.1.2, the displacement error of all foldable linear moment elements was found to converge with the same rate as the constant moment elements. After close investigation of the $HSM^{(2)}$-element in Section 4.1.3, it was found to be completely inaccurate, because it overestimated fold stiffness, as it did not contain enough DOFs to accurately capture all modes of deformation. Since most displacement in a folded plate is due to its folding deformation, the error in fold angle caused a large error in displacement field. Furthermore, the error in $HSM^{(2)}$-element could already be found in the standard element; in Figure 4.7, the standard HSM-element was found to have a relatively small displacement error in a test were only a linear moment field would be present, and the linear moment HSM-element could be expected to achieve exact results. The small error in the standard HSM-element is thus magnified when folding deformations are introduced, and the $HSM^{(2)}$-element was not further investigated.

The $KL1^{(c)}$-element was found to attain higher errors than the $KL1^{(2)}$-element, due to the enriched edge continuity error, introduced by the local condensation. When the mesh increased and element size decreased, the enriched edge length also decreased, generally causing the enriched edge continuity error to decrease, and the $KL1^{(c)}$-error to approximate the $KL1^{(2)}$-error. Furthermore, the foldable $KL1$ elements were found to have unstable convergence behavior; when a tilted straight fold was imposed on a square plate in Section 4.1.4, the convergence rate of the elements decreased. An explanation for the lowered convergence rate could be over-constraining of the moment field. Since the enriched DOF $\Delta w_{,n}$ is directly coupled to the moment field at the fold, sharing enriched DOFs between elements may cause C^0 moment continuity to be imposed between enriched elements, and due to this extra constraint the elements may be less good at describing the complex moment field around the fold. Besides the lowered convergence rate for tilted straight folds, the convergence rate of the $KL1^{(2)}$-element was found to be unstable and to decrease for curved folds in Section 4.3. Due to the linear approximation of a curved fold, a mismatch is introduced in the mapping of the enriched DOF on the enriched edges of neighboring elements. The mismatch in mapping caused an enriched edge displacement field discontinuity, and introduced an extra error in the $KL1^{(2)}$-element.

Investigating the matrix condition numbers of the $KL1^{(2)}$ and $KL1^{(c)}$ elements, similar results as for the constant moment elements were found. The $KL1^{(2)}$-element had relatively bad unbounded condition numbers, while the $KL1^{(c)}$-element attained bounded condition numbers. As seen in Figure 4.13, the condition numbers of the foldable $KL1$ element were generally worse than those of the foldable $KL0$-elements. As shown in Figure 4.14, the condition numbers could again be greatly improved using a Jacobi preconditioner.

5.1.4. Achievements and limitations

Whereas most existing numerical origami modeling techniques are either flexible or able to accurately calculate facet deformations, as described in Section 1.1, the methods presented in this thesis combined flexibility and accuracy. Even though folded origami structures can not yet be modeled with the foldable plate elements in this thesis, the methods presented may be expanded to create folded shell elements suited for modeling origami structures. In comparison to the enriched plate elements, described in Section 1.3, the advantage of the mixed/hybrid formulation with a C^1-continuous moment field was that no enrichment needed to be defined on the element domain Ω, which simplified the formulation of enrichment functions and integration elements. Only on the boundary segments intersected by the fold, enrichment functions were defined, and 1D integration elements were created. By implementing a displacement enrichment defined by a constant jump in derivative, as proposed in [33], no scaling of the displacement enrichment function is needed as it naturally decreases to zero for folds approximating standard nodes, and the rotational enrichment is bounded by ± 1.

In [26], known locking-free elements were used to create cracked plate elements, but after enrichment of the elements, some locking behavior was again observed. Similarly, the $KL1$ element showed decreased convergence rates, after an enrichment was applied, while the foldable $KL0$ elements did not show decreased convergence rates. Since the main difference between the $KL0$ and $KL1$ enrichment procedure, is the contribution of an edge enrichment function to the element, the decreased convergence rates may be caused by introducing these enrichment functions.

	$KL0^{(2)}$	$KL0^{(1)}$	$KL0^{(c)}$	$KL1^{(2)}$	$KL1^{(c)}$	hinged $KL0$
Condition number	++	++	+++	+	+++	+
Error convergence	+++	+++	+++	++	+	+++
Absolute error	+	+	+	+++	+++	++
Enriched edge continuity	✓	✗	✗	✓	✗	✓

Table 5.1: The six different foldable element formulations rated in their condition number, error convergence, and absolute error. Additionally their insurance of enriched-edge continuity is summarized, and a relation between error, condition numbers, and enriched-edge continuity can be found.

Between all elements, the $KL0^{(c)}$-element achieved the best overall results, as it had: convergence behavior similar to the standard FEM hinged $KL0$ solution, bounded condition numbers, and no enriched DOFs. In [21], a GFEM is a Stable GFEM (SGFEM), if it yields *optimal order of convergence* and the conditioning of the GFEM is not worse than that of the standard FEM, *i.e.* there exists a constant $L > 0$, independent of the mesh, such that:

$$\frac{\chi_{GFEM}}{\chi_{FEM}} \leq L < \infty. \tag{5.1}$$

where χ_{GFEM} and χ_{FEM} are the condition numbers of the enriched part of the stiffness matrix and standard standard part of the stiffness matrix respectively. Following this definition, the $KL0^{(c)}$-element can be said to be a stable enriched element. The $KL1^{(c)}$-element can not be said to be stable, as it does not yield optimal order of convergence. The condition numbers of all other elements were not bounded, but could be greatly improved using a Jacobi preconditioner. In Table 5.1, all elements are compared in convergence behavior, condition number, and enriched edge continuity. Generally, elements which do not ensure enriched edge continuity, attain worse errors but better condition numbers, than elements which do ensure enriched-edge continuity. For example, condensing the elements introduces the enriched edge continuity error, and the condensed elements thus attain better condition numbers, but worse errors than their uncondensed counterparts. Furthermore, the lower order $KL0^{(1)}$ and $KL0^{(2)}$ elements attain worse absolute errors and better condition numbers, than the higher order $KL1^{(2)}$-element.

5.2. Conclusion

In this thesis a mixed/hybrid formulation was successfully used to create foldable Kirchhoff-Love plate elements. Furthermore, all three sub-questions in Section 1 have been answered:

1. A modified potential energy equation in a foldable plate can be formulated in terms of the moment field, by imposing kinematic relations particular to a foldable structure on a potential energy equation via Lagrange multipliers.

2. To accurately model foldable plate elements, no enrichment for the moment field is required. In foldable linear moment plate elements, displacement enrichments are required on folded element edges, while in constant moment plate elements, the edge enrichment functions do not contribute to the stiffness matrix. By defining a displacement enrichment, such that it has a constant jump in derivative at the fold, the enriched DOF is connected to the jump in rotation, rather than the displacement at the fold.

3. Matrix condition numbers of non-condensed foldable elements are unbounded for folds approximating standard element nodes, due to the enriched $\boldsymbol{B}$-matrix converging to a null matrix, causing enriched parts of the global stiffness matrix to also converge to a null matrix. Furthermore, linear moment elements attain worse condition numbers, than constant moment elements. The matrix condition can be improved using two methods; either a Jacobi preconditioner, or a local element condensation can be used.

Even though folded shell elements have not yet been defined, this thesis proves that using a mixed/hybrid formulation, discontinuities can be modeled in plate elements, and advancing on the elements in this thesis, folded shell elements may be formulated. Additionally, many more discontinuous problems, such as elements containing cracks or material interfaces, may be modeled using similar methods as the mixed/hybrid enriched formulation presented in this thesis.

5.3. Outlook and recommendations

Several recommendations for the advancement of the presented foldable plate elements, and further development of the enriched mixed/hybrid methods used can be made:

- Some challenges were encountered in the foldable $KL1$ elements, as they did not achieve optimal convergence. Furthermore, convergence rates decreased, due to an error in the mapping of enriched DOFs, when curved folds were analyzed. As illustrated in Figure 4.23, the linear approximation of the curved fold resulted in an enriched edge continuity error. To remove this error, instead of using the orientation of the linear approximations of the fold, the orientation of the actual curved fold (θ in Figure 5.1) could be computed, and used to project the enriched DOF on the enriched edge of neighboring elements. Using these globally defined angles, should result in enriched edge continuity and remove the error. Furthermore, the foldable $KL1$ elements were found to converge with lower rates than the non-foldable $KL1$ element. Since no concrete cause for this behavior was found, further research is required into the causes and solutions for the lowered convergence rate.

- In this thesis, only elements containing a single fold were examined, since origami structures often contain many intersecting folds, future work could extend the elements to multiple folds. Multiple non-intersecting folds, may be introduced in an element by introducing multiple enriched $\boldsymbol{B}$-matrices as: $\boldsymbol{B} = [\boldsymbol{B}_S, \boldsymbol{B}_{E1}, \boldsymbol{B}_{E2}]$, and multiple $\boldsymbol{K}_t$-matrices, without changing any of the sub-matrix definitions. Elements containing intersecting folds may require more attention; on vertices where folds intersect, a fold can change from a ridge to a valley fold, creating a strong discontinuity in fold angle. This problem may be addressed by introducing constraint equations, as in rigid foldability analysis [12], around the fold vertex. These constraints may be added into the modified potential energy equation via Lagrange multipliers, and the fold can be enriched using a strong enrichment inspired by DE-FEM [10].

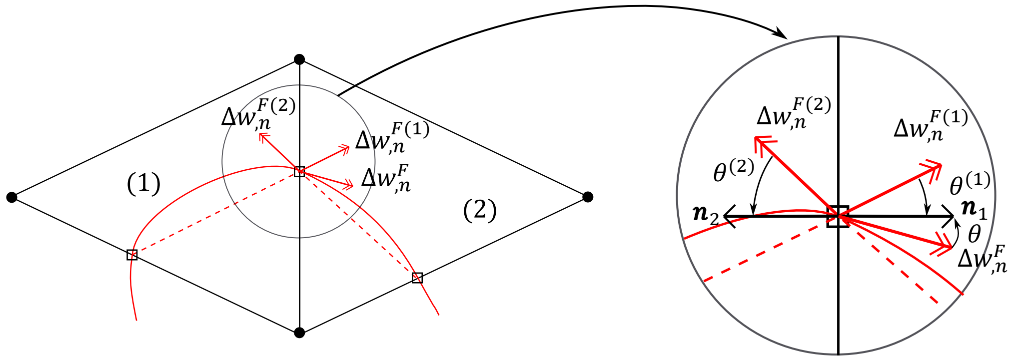

Figure 5.1: Two triangular elements cut by a curved fold (red) which is interpolated as two linear fold segments (dashed). At the shared boundary of the two elements, the DOFs representing the jump in rotation in the two elements ($\Delta w_{,n}^{F(1)}$, $\Delta w_{,n}^{F(2)}$) are not aligned with the real tangential vector representing the jump in rotation ($\Delta w_{,n}^{F}$). Instead of using the orientation of the linear approximation of the fold line ($\theta^{(1)}$ and $\theta^{(1)}$) the actual orientation of the fold line θ may be used to project the jump in rotation on the element edge, removing the enriched edge continuity error.

- Another limitation of the current work is that only foldable plate elements were derived; elements which form ridge-like structures from a flat configuration. This formulation only allows for structures developing small fold angles to be modeled. In [33], a foldable shell derivation in a mesh free setting is used to model folded structures, by incrementally increasing the fold angle via a non-linear analysis. Shell elements are needed, as in these folded structures membrane stresses are present. Extending the formulation in this thesis to shell elements, this method could also be used in combination with the presented methods to model small fold angles, in foldable origami structures.

- Future work may be done on developing folded shell elements, in which the folds contain large fold angles *a priori* of deformation, such that the deformation of complicated folded origami structures could be precisely examined. In these folded elements, weak discontinuities in the moment field may be introduced across the fold line. Adding weak enrichments to the moment field of a constant moment element would be illogical, as adding a weak enrichment would increase the order of the moment interpolation. Although no moment field enrichment may be needed in these elements, the *a priori* fold angle would still cause a discontinuity in director field. A director field discontinuity, may be introduced via a director field enrichment, coupled to the fold angle, using similar methods as in the cracked plate in [27]. In a linear moment element, a weak moment field enrichment may be needed. Furthermore, in an *a priori* folded element, the weak discontinuity may depend on the fold angle and force applied on the element only. If shell elements are used to model the folded structure, auxiliary DOFs concerning membrane stresses/forces may be introduced, when the elements are derived via a mixed/hybrid formulation. Since the *a priori* fold angle and stresses/forces in the system may be known, a weak moment enrichment could be formulated, without adding enriched auxiliary DOFs, but using the auxiliary DOFs concerning the membrane stresses/forces. The suggestion is thus to extract a weak moment field enrichment from the *a priori* known fold angle in the element, instead of introducing it using extra auxiliary DOFs.

- Another future research direction could be the more general application of the mixed/hybrid enriched methods, presented in this thesis. Via these methods, the minimum amount of enriched DOFs may be introduced in problems containing discontinuities. Furthermore, local condensation may be used to greatly improve matrix condition and decrease the size of the enriched stiffness matrix, although this may come at the cost of a loss of accuracy. A possible application could be the enrichment of constant stress/strain triangles including weak discontinuities, due to a material interface. In such an element, a weak discontinuity in displacement field would lead to a strong discontinuity in strain field, but when a stress field interpolation is used in combination with a mixed/hybrid formulation, no strong discontinuity may be added, as this would result in a loss of equilibrium at the material interface. Even if no stress field enrichment would be needed, additional terms may be required to account for energy consumed on the discontinuity, or a weak displacement enrichment located on the element boundary.

Bibliography

[1] K. Hatori, *Origami 5: Fifth Inter Inational Meeting of Origami Science, Mathematics, and Education*, ch. Origami, History, Art, and Design. CRC Press, 2011.

[2] S. Zirbel, B. Traese, S. Magleby, and L. Howell, "Deployment methods for an origami-inspired rigid-foldable array," *The 40th Aerospace Mechanisms Symposium*, pp. 189–194, 2014.

[3] X. Liu, S. Yao, S. V. Georgakopoulos, *et al.*, "Reconfigurable helical antenna based on an origami structure for wireless communication system," *International Microwave Symposium (IMS2014)*, 2014.

[4] R. Harne and D. Lynd, "Origami acoustics: Using principle of folding structural acoustics for simple and large focusing of sound energy," *Smart Materials and Structures*, vol. 25, 2016.

[5] S. Miyashita, S. Guitron, M. Ludersdorfer, *et al.*, "An untethered miniature origami robot that self-folds, walks, swims, and degrades," *International Conference on Robotics and Automation (ICRA)*, pp. 1490–1496, 2015.

[6] J. Silverberg, A. Evans, L. McLeod, *et al.*, "Using origami design principles to fold reprogrammable mechanical metamaterials," *Science*, vol. 345, pp. 647–650, 2014.

[7] F. Martinex and A. Thrall, "Honeycomb core sandwich panels for origami-inspired shelters: Multi-objective optimization for minimum weight and maximum energy efficiency," *Engineering Structures*, vol. 69, pp. 158–167, 2014.

[8] T. Tachi, *Origami 4: Fourth International Meeting of Origami Science, Mathematics, and Education*, ch. Simulation of Rigid Origami, pp. 175–187. CRC Press, 2009.

[9] M. Schenk and S. Guest, *Origami 5: Fifth International Meeting of Origami Science, Mathematics, and Education*, ch. Origami folding: A structural engineering approach, pp. 291–303. CRC Press, 2011.

[10] A. Aragón and A. Simone, "The discontinuity-enriched finite element method," *International Journal for Numerical Methods in Engineering*, vol. 112, pp. 1589–1613, 2017.

[11] S. Soghrati, A. Aragón, C. Duarte, and P. Geubelle., "An interface-enriched generalized fem for problems with discontinuous gradient fields," *International Journal for Numerical Methods in Engineering*, vol. 89, pp. 991 – 1008, 2012.

[12] S. Belcasto. and T. Hull., "Modelling the folding of paper into three dimensions using affine transformations," *Linear Algebra and Its Applications*, vol. 348, pp. 273–282, 2002.

[13] T. Smit., "Finite element modeling of non-rigid origami," Master's thesis, Delft University of Technology, July 2017.

[14] E. Peraza, Hernandez, D. Hertl, E. Akleman, and D. Lagoudas, "Modeling and analysis of origami structures with smooth folds," *Computer-Aided Design*, vol. 78, pp. 93–106, 2016.

[15] T. Strouboulis, I. Babuška, and K. Copps, "The design and analysis of the generalized finite element method," *Computational methods in applied mechanics and engineering*, vol. 181, pp. 43–69, 2000.

[16] N. Moes, J. Dolbow, and T. Belytschko, “A finite element method for crack growth without remeshing,” *International Journal for Numerical Methods in Engineering*, vol. 46, pp. 131–150, 1999.

[17] T. Belytschko, R. Gracie, and G. Ventura., “A review of extended/generalized finite element methods for material modeling,” *Modelling and Simulations in Materials Science and Engineering*, vol. 17, 2009.

[18] I. Bubuška and U. Banerjee, “Stable generalized finite element method (SGFEM),” *Computational Methods in Applied Mechanics and Engineering*, vol. 201-204, pp. 91–111, 2012.

[19] C. Lang, D. Makhija, A. Doostan, and K. Maute, “A simple and efficient preconditioning scheme for heaviside enriched XFEM,” *Computational Mechanics*, vol. 54, pp. 1357–1374, 2014.

[20] V. Gupta, C. Duarte, I. Babuška, and U. Banerjee, “A stable and optimally convergent generalized fem (SGFEM) for linear elastic fracture mechanics.,” *Computational Methods in Applied Mechanics and Engineering.*

[21] Q. Zhang, U. Banerjee, and I. Babuška, “Strongly stable generalized finite element method (SSGFEM) for a non-smooth interface problem,” *Computational methods in applied mechanics and engineering*, vol. 344, pp. 538–568, 2019.

[22] S. Soghrati, C. Duarte, and P. Geubelle, “An adaptive interface-enriched generalized fem for the treatment of problems with curved interfaces,” *International Journal For Numerical Methods In Engineering*, vol. 102, pp. 1352–1370, 2015.

[23] S. Soghrati, “Hierarchical interface-enriched finite element method: An automated technique for mesh-independent simulations,” *Journal of Computational Physics*, vol. 275, pp. 41–52, 2014.

[24] S. Soghrati and P. Geubelle, “A 3D interface-enriched generalized finite element method for weakly discontinuous problems with complex internal geometries,” *Computational Methods in Applied Mechanics and Engineering*, vol. 217-220, pp. 46–57, 2012.

[25] S. Soghrati and H. Ahmadian, “3D hierarchical interface-enriched finite element methods: Implementation and applications,” *Journal of Computational Physics*, vol. 299, pp. 45–55, 2015.

[26] J. Dolbow, N. Moës, and T. Belytschko, “Modeling fracture in mindlin-reissner plates with the extended finite element method,” *International Journal of Solids and Structures*, vol. 37, pp. 7161–7183, 2000.

[27] P. Areias and T. Belytschko, “Non-linear analysis of shells with arbitrary evolving cracks using XFEM,” *International Journal For Numerical Methods In Engineering*, vol. 62, pp. 384–415, 2005.

[28] H. Bayesteh and S. Mohammadi, “XFEM fracture analysis of shells: The effect of crack tip enrichments,” *Computational Materials Science*, vol. 50, pp. 2793–2813, 2011.

[29] A. Peano, “Hierarchies of conforming finite elements for plane elasticity and plate bending,” *Computers Mathematics with Applications*, vol. 2, pp. 211–224, 1976.

[30] J. Lasry, J. Pommier, Y. Renard, and M. Salaün, “eXtended finite element methods for thin cracked plates with kirchhoff-love theory,” *International Journal for Numerical Methods in Engineering*, vol. 84, pp. 1115–1138, 2010.

[31] P. Laborde, J. Pommier, Y. Renard, and M. Salaün, “High-order extended finite element method for cracked domains,” *International Journal for Numerical Methods in Engineering*, vol. 64, pp. 354–381, 2005.

[32] P. Areias, J. Song, and T. Belytschko, “Analysis of fracture in thin shells by overlapping paired elements,” *Computational methods in applied mechanics and engineering*, vol. 195, pp. 5343–5360, 2006.

[33] E. Barbieri, L. Ventura, D. Grignoli, and E. Bilotti, “A meshless method for the nonlinear von kármán plate with multiple folds of complex shape,” *Computational Mechanics*, 2019.

[34] W. Liu, S. Jun, and Y. Zhang, “Reproducing kernel particle methods,” *International Journal for Numerical Methods in Fluids*, vol. 20, pp. 1081–1106, 1995.

[35] T. Pian., “State-of-the-art development of hybrid/mixed finite element method,” *Finite Elements an Analysis and Design*, vol. 21, pp. 5–20, 1995.

[36] S. Lee and S. Wong, “Mixed formulation finite elements for mindlin theory plate bending,” *International Journal for Numerical Methods in Engineering*, vol. 18, pp. 1297–1311, 1982.

[37] K. Bathe and L. Ho, “A study of three-node triangular plate bending elements,” *International Journal for Numerical Methods in Engineering*, vol. 15, pp. 1771–1812, 1980.

[38] T. Pain and P. Tong, “Basis of finite element methods for solid continua,” *International Journal for Numerical Methods in Engineering*, vol. 1, pp. 3–28, 1969.

[39] F. van and Keulen, *On refined triangular plate and shell elements.* PhD thesis, Delft University of Technology, January 1993.

[40] M. Toolabi, A. Fallah, P. Baiz, and L. Louca, “Enhanced mixed interpolation XFEM formulations for discontinuous timoshenko beam and mindlin-reissner plate,” *International Journal for Numerical Methods in Engineering*, vol. 115, pp. 714–737, 2018.

[41] N. Moës, M. Cloirec, P. Cartraud, and J. Remacle, “A computational approach to handle complex microstructure geometries,” *Computational methods in applied mechanics and engineering*, vol. 192, pp. 3163–3177, 2003.

[42] A. Zilian and T. Fries, “A localized mixed-hybrid method for imposing interfacial constraints in the extended finite element method (XFEM),” *International Journal for Numerical Methods in Engineering*, vol. 79, pp. 733–752, 2009.

[43] G. Wells, “The finite element method: An introduction,” *University of Cambridge and Delft University of Technology*, 2009.

[44] E. Wilson, “The static condensation algorithm,” *International Journal For Numerical Methods In Engineering*, vol. 8, pp. 198–203, 1974.

[45] K. Markestein, “Finite element based analysis and validation for nonlinear structural dynamics,” Master’s thesis, Delft University of Technology, November 2018.

[46] S. Timoshenko and S. W. Woinowsky-Krieger, *Theory of plates and shells, 2nd edition.* McGraw-Hill book company, 1959.

A

Potential energy formulation for a folded beam

In this appendix, the full potential energy derivation for a folded beam will be discussed. We use the conventions used in Section 2.1. In the potential energy function we include the bending stiffness of the beam, the torsional stiffness of the fold, and potential energy of the loads. It is assumed no external moments are applied at the fold, resulting in the following potential energy equation:

$$\Pi = \int_{0}^{x_\Gamma^-} \left\{ \frac{1}{2} EI\kappa^2 - q(x)w \right\} dx + \frac{1}{2} k_t \Delta\phi^2 + \int_{x_\Gamma^+}^{L} \left\{ \frac{1}{2} EI\kappa^2 - q(x)w \right\} dx + W, \tag{A.1}$$

where W, the potential energy due to the loading of the beam, is defined as:

$$W = F_1 w_1 + M_1 \phi_1 - F_2 w_2 - M_2 \phi_2 - F_\Gamma w_\Gamma. \tag{A.2}$$

In Equation A.1 there is an opportunity to introduce different Young's moduli or moment of inertia for both subdomains. It is chosen to keep both values constant since most origami structures are made from a single sheet of material and will have constant Young's modulus and moment of inertia. Because we will be looking at different fields for $u(x)$, $\phi(x)$, and $\kappa(x)$ their kinematic relations are enforced via Lagrange multipliers, as will the relation between w_Γ^-, w_Γ^+ and w_Γ:

$$\begin{aligned}\Pi = \int_{0}^{x_\Gamma^-} \left\{ \frac{1}{2} EI\kappa^2 + \lambda_1 (\phi - \frac{\partial w}{\partial x}) + \lambda_2 (\kappa - \frac{\partial \phi}{\partial x}) - q(x)w \right\} dx + \frac{1}{2} k_t \Delta\phi^2 + \lambda_3 (w_\Gamma - w_\Gamma^-) + \\ \lambda_4 (w_\Gamma^+ - w_\Gamma) + \int_{x_\Gamma^+}^{L} \left\{ \frac{1}{2} EI\kappa^2 + \lambda_5 (\phi - \frac{\partial w}{\partial x}) + \lambda_6 (\kappa - \frac{\partial \phi}{\partial x}) - q(x)w \right\} dx + W.\end{aligned} \tag{A.3}$$

A.1. Interpretation of Lagrange multipliers

Physical meaning is given to the six Lagrange multipliers by means of virtual variations. First, the modified potential energy function is varied with respect to κ as:

$$\partial\Pi = \frac{\partial\Pi}{\partial\kappa}\delta\kappa = \int_{0}^{x_\Gamma^-} \{EI\kappa \ + \lambda_2\} \delta\kappa dx + \int_{x_\Gamma^+}^{L} \{EI\kappa \ + \lambda_6\} \delta\kappa dx = 0, \tag{A.4}$$

resulting in,

$$\lambda_2 = -EI\kappa = -M \ on \ \Omega_1, \tag{A.5}$$

$$\lambda_6 = -EI\kappa = -M \ on \ \Omega_2. \tag{A.6}$$

Inserting Equations A.5, A.6, and the relation between moment and curvature in Equation 2.6, into Equation A.3, results in a new modified potential energy function, where κ, λ_2 and λ_6 are removed:

$$\Pi = \int_0^{x_\Gamma^-} \left\{ -\frac{1}{2EI}M^2 + M\frac{\partial \phi}{\partial x} + \lambda_1(\phi - \frac{\partial w}{\partial x}) - q(x)w \right\} dx + \frac{1}{2}k_t\Delta\phi^2 + \lambda_3(w_\Gamma - w_\Gamma^-) +$$
$$\lambda_4(w_\Gamma^+ - w_\Gamma) + \int_{x_\Gamma^+}^{L} \left\{ -\frac{1}{2EI}M^2 + M\frac{\partial \phi}{\partial x} + \lambda_5(\phi - \frac{\partial w}{\partial x}) - q(x)w \right\} dx + W. \tag{A.7}$$

Secondly, the new modified potential energy function is now varied with respect to ϕ:

$$\partial\Pi = \frac{\partial \Pi}{\partial \phi}\delta\phi = \int_0^{x_\Gamma^-} \left\{ M\frac{\partial}{\partial x} + \lambda_1 \right\} \delta\phi dx + k_t(\phi_\Gamma^+ - \phi_\Gamma^-)(\delta\phi_\Gamma^+ - \delta\phi_\Gamma^-)$$
$$+ \int_{x_\Gamma^+}^{L} \left\{ M\frac{\partial}{\partial x} + \lambda_5 \right\} \delta\phi dx + M_1\delta\phi_1 - M_2\delta\phi_2 = 0. \tag{A.8}$$

The moments applied at the ends of the beam, entered into the equation. To eliminate these terms, the moment field is moved from the domain integrals to boundary evaluations, using:

$$M\frac{\partial \delta\phi}{\partial x} = \frac{d}{dx}(M\delta\phi) - \frac{\partial M}{\partial x}\delta\phi. \tag{A.9}$$

Inserting this into the varied functional results in:

$$\partial\Pi = \int_0^{x_\Gamma^-} \left\{ \lambda_1 - \frac{\partial M}{\partial x} \right\} \delta\phi dx + [M\delta\phi]_{x=0}^{x=x_\Gamma^-} + k_t(\phi_\Gamma^+ - \phi_\Gamma^-)(\delta\phi_\Gamma^+ - \delta\phi_\Gamma^-)$$
$$+ \int_{x_\Gamma^+}^{L} \left\{ \lambda_5 - \frac{\partial M}{\partial x} \right\} \delta\phi dx + [M\delta\phi]_{x=x_\Gamma^+}^{x=L} + M_1\delta\phi_1 - M_2\delta\phi_2 = 0, \tag{A.10}$$

and we conclude for the Lagrange multipliers that:

$$\lambda_1 = \frac{\partial M}{\partial x} \text{ on } \Omega_1, \tag{A.11}$$

$$\lambda_5 = \frac{\partial M}{\partial x} \text{ on } \Omega_2. \tag{A.12}$$

Only the terms within the integral in Equation A.10 are interpreted. To interpret the other results, they are grouped together as:

$$[M\delta\phi]_{x=0}^{x=x_\Gamma^-} + k_t(\phi_\Gamma^+ - \phi_\Gamma^-)(\delta\phi_\Gamma^+ - \delta\phi_\Gamma^-) + [M\delta\phi]_{x=x_\Gamma^+}^{x=L} + M_1\delta\phi_1 - M_2\delta\phi_2 = (M|_{x_\Gamma^-} - k_t(\phi_\Gamma^+ - \phi_\Gamma^-))\delta\phi_\Gamma^- +$$
$$(M_1 - M|_0)\delta\phi_1 + (M|_L - M_2)\delta\phi_2 + (k_t(\phi_\Gamma^+ - \phi_\Gamma^-) - M|_{x_\Gamma^+})\delta\phi_\Gamma^+ = 0. \tag{A.13}$$

Rewriting the equations, moment continuity within the element is achieved as:

$$M|_{x_\Gamma^-} = M|_{x_\Gamma^+} = k_t(\phi_\Gamma^+ - \phi_\Gamma^-) = k_t\Delta\phi = M_\Gamma. \tag{A.14}$$

Back-substituting the Lagrange multipliers into the modified potential energy equation only two multipliers remain:

$$\begin{aligned}\Pi = \int_0^{x_\Gamma^-} \left\{ -\frac{1}{2EI}M^2 + M\frac{\partial \phi}{\partial x} + \frac{\partial M}{\partial x}\phi - \frac{\partial M}{\partial x}\frac{\partial w}{\partial x} - q(x)w \right\} dx \\ + \frac{1}{2}k_t\Delta\phi^2 + \lambda_3(w_\Gamma - w_\Gamma^-) + \lambda_4(w_\Gamma^+ - w_\Gamma) \\ + \int_{x_\Gamma^+}^{L} \left\{ -\frac{1}{2EI}M^2 + M\frac{\partial \phi}{\partial x} + \frac{\partial M}{\partial x}\phi - \frac{\partial M}{\partial x}\frac{\partial w}{\partial x} - q(x)w \right\} dx + W.\end{aligned} \tag{A.15}$$

The last Lagrange multipliers are given physical meaning by varying with respect to w as:

$$\begin{aligned}\partial\Pi = \frac{\partial \Pi}{\partial w}\delta w = \int_0^{x_\Gamma^-} \left\{ -q(x) - \frac{\partial M}{\partial x}\frac{\partial}{\partial x} \right\} \delta w dx + \lambda_3(\delta w_\Gamma - \delta w_\Gamma^-) \\ + \lambda_4(\delta w_\Gamma^+ - \delta w_\Gamma) + \int_{x_\Gamma^+}^{L} \left\{ -q(x) - \frac{\partial M}{\partial x}\frac{\partial}{\partial x} \right\} \delta w dx \\ + F_1\delta w_1 - F_2\delta w_2 - F_\Gamma\delta w_\Gamma.\end{aligned} \tag{A.16}$$

The term within the integral is simplified using:

$$\frac{\partial M}{\partial x}\frac{\delta w}{\partial x} = \frac{d}{dx}\left(\frac{\partial M}{\partial x}\delta w\right) - \frac{\partial^2 M}{\partial x^2}\delta w, \tag{A.17}$$

resulting in the varied functional:

$$\begin{aligned}\int_0^{x_\Gamma^-} \left\{ -f(x) + \frac{\partial^2 M}{\partial^2 x} \right\} \delta w dx - \left[\frac{\partial M}{\partial x}\delta w\right]_{x=0}^{x=x_\Gamma^-} + \lambda_3(\delta w_\Gamma - \delta w_\Gamma^-) + \\ \lambda_4(\delta w_\Gamma^+ - \delta w_\Gamma) + \int_{x_\Gamma^+}^{L} \left\{ -f(x) + \frac{\partial^2 M}{\partial^2 x} \right\} \delta w dx - \left[\frac{\partial M}{\partial x}\delta w\right]_{x=x_\Gamma^+}^{x=L} + F_1\delta w_1 - F_2\delta w_2 - F_\Gamma\delta w_\Gamma.\end{aligned} \tag{A.18}$$

The functional is simplified and relevant terms are grouped together as:

$$\begin{aligned}\int_0^{x_\Gamma^-} \left\{ \frac{\partial^2 M}{\partial^2 x} - f(x) \right\} \delta w dx + \int_{x_\Gamma^+}^{L} \left\{ \frac{\partial^2 M}{\partial^2 x} - f(x) \right\} \delta w dx + \left(\left.\frac{\partial M}{\partial x}\right|_0 + F_1 \right) \delta w_1 \\ - \left(\left.\frac{\partial M}{\partial x}\right|_L + F_2 \right) \delta w_2 + (\lambda_3 - \lambda_4 - F_\Gamma)\delta w_\Gamma - \left(\left.\frac{\partial M}{\partial x}\right|_{x_\Gamma^-} + \lambda_3 \right) \delta w_\Gamma^- \\ + \left(\left.\frac{\partial M}{\partial x}\right|_{x_\Gamma^+} + \lambda_4 \right) \delta w_\Gamma^+.\end{aligned} \tag{A.19}$$

From these equations, we conclude for the Lagrange multipliers that:

$$\lambda_3 = -\left.\frac{\partial M}{\partial x}\right|_{x_\Gamma^-}, \tag{A.20}$$

$$\lambda_4 = -\left.\frac{\partial M}{\partial x}\right|_{x_\Gamma^+}. \tag{A.21}$$

Furthermore, we retrieve that:

$$F_1 = -\left.\frac{\partial M}{\partial x}\right|_0, \tag{A.22}$$

$$F_2 = -\left.\frac{\partial M}{\partial x}\right|_L. \tag{A.23}$$

Looking at the leftover terms within the integrals, we can conclude in a weak sense for both subdomains Ω_1 and Ω_2 that:

$$\int \left\{\frac{\partial^2 M}{\partial^2 x} - q(x)\right\} dx = 0. \tag{A.24}$$

In a strong sense this implies that:

$$q(x) = \frac{\partial^2 M}{\partial^2 x} \text{ and,} \tag{A.25}$$

$$Q(x) = \frac{\partial M}{\partial x}. \tag{A.26}$$

Equation A.22, A.23, and A.26 contain the generally known equilibrium condition for beams where:

$$-Q(x) = F(x) = -\frac{\partial M}{\partial x}, \tag{A.27}$$

A final conclusion which can be drawn from the variation with respect to w is,

$$\lambda_3 - \lambda_4 = \left.\frac{\partial M}{\partial x}\right|_{x_\Gamma^+} - \left.\frac{\partial M}{\partial x}\right|_{x_\Gamma^-} = F_\Gamma. \tag{A.28}$$

If no force would be applied at the fold this would mean that $\lambda_3 = \lambda_4$, resulting in:

$$\left.\frac{\partial M}{\partial x}\right|_{x_\Gamma^+} = \left.\frac{\partial M}{\partial x}\right|_{x_\Gamma^-}. \tag{A.29}$$

Assuming no force is applied on the fold simplifies the moment field in the element, which can be one linear function over the entire element. If the application of a force on the fold is to be maintained, standard linear interpolations with a weak enrichment should be used in the discretization. Finally, back substituting Equation A.20 and A.21 into the potential energy equation, all Lagrange multipliers are interpreted as:

$$\begin{aligned}\Pi = \int_0^{x_\Gamma^-} \left\{-\frac{1}{2EI}M^2 + M\frac{\partial \phi}{\partial x} + \frac{\partial M}{\partial x}\phi - \frac{\partial M}{\partial x}\frac{\partial w}{\partial x} - q(x)w\right\} dx + \frac{1}{2}k_t \Delta\phi^2 - \\ \left.\frac{\partial M}{\partial x}\right|_{x_\Gamma^-}(w_\Gamma - w_\Gamma^-) - \left.\frac{\partial M}{\partial x}\right|_{x_\Gamma^+}(w_\Gamma^+ - w_\Gamma) + \\ \int_{x_\Gamma^+}^{L} \left\{-\frac{1}{2EI}M^2 + M\frac{\partial \phi}{\partial x} + \frac{\partial M}{\partial x}\phi - \frac{\partial M}{\partial x}\frac{\partial w}{\partial x} - q(x)w\right\} dx + W.\end{aligned} \tag{A.30}$$

A.2. Simplification of the potential energy function

Terms from the integral are moved to the boundaries to remove the need for interpolating functions for $\phi(x)$ and $w(x)$ on the beam. This is done by applying two mathematical relations. Firstly we use:

$$M\frac{\partial \phi}{\partial x} = \frac{d}{dx}(M\phi) - \frac{\partial M}{\partial x}\phi, \tag{A.31}$$

and insert it into the modified potential energy function to remove $\phi(x)$ from the integral:

$$\begin{aligned}\Pi = \int_0^{x_\Gamma^-} \left\{-\frac{1}{2EI}M^2 - \frac{\partial M}{\partial x}\frac{\partial w}{\partial x} - q(x)w\right\} dx + [M\phi]_0^{x_\Gamma^-} + \frac{1}{2}k_t\Delta\phi^2 - \\ \left.\frac{\partial M}{\partial x}\right|_{x_\Gamma^-}(w_\Gamma - w_\Gamma^-) - \left.\frac{\partial M}{\partial x}\right|_{x_\Gamma^+}(w_\Gamma^+ - w_\Gamma) + \\ \int_{x_\Gamma^+}^{L} \left\{-\frac{1}{2EI}M^2 - \frac{\partial M}{\partial x}\frac{\partial w}{\partial x} - q(x)w\right\} dx + [M\phi]_{x_\Gamma^+}^{L} + W.\end{aligned} \tag{A.32}$$

Secondly we use:

$$-\frac{\partial M}{\partial x}\frac{\partial w}{\partial x} = -\frac{d}{dx}\left(\frac{\partial M}{\partial x}w\right) + \frac{\partial^2 M}{\partial x^2}w, \tag{A.33}$$

and insert it into the modified potential energy function to remove $\partial M/\partial x$ from the integral:

$$\begin{aligned}\Pi = \int_0^{x_\Gamma^-} \left\{-\frac{1}{2EI}M^2 + \left(\frac{\partial^2 M}{\partial^2 x} - q(x)\right)w\right\} dx - \left[\frac{\partial M}{\partial x}w\right]_0^{x_\Gamma^-} + [M\phi]_0^{x_\Gamma^-} + \frac{1}{2}k_t\Delta\phi^2 - \\ \left.\frac{\partial M}{\partial x}\right|_{x_\Gamma^-}(w_\Gamma - w_\Gamma^-) - \left.\frac{\partial M}{\partial x}\right|_{x_\Gamma^+}(w_\Gamma^+ - w_\Gamma) + \int_{x_\Gamma^+}^{L} \left\{-\frac{1}{2EI}M^2 + \left(\frac{\partial^2 M}{\partial^2 x} - q(x)\right)w\right\} dx - \\ \left[\frac{\partial M}{\partial x}w\right]_{x_\Gamma^+}^{L} + [M\phi]_{x_\Gamma^+}^{L} + W.\end{aligned} \tag{A.34}$$

Different terms concerning the displacement are present in the potential energy function. The terms containing w_Γ^- and w_Γ^+ are removed by using:

$$\begin{aligned}-\left[\frac{\partial M}{\partial x}w\right]_0^{x_\Gamma^-} - \left.\frac{\partial M}{\partial x}\right|_{x_\Gamma^-}(w_\Gamma - w_\Gamma^-) - \left.\frac{\partial M}{\partial x}\right|_{x_\Gamma^+}(w_\Gamma^+ - w_\Gamma) - \left[\frac{\partial M}{\partial x}w\right]_{x_\Gamma^+}^{L} = \\ \left.\frac{\partial M}{\partial x}\right|_0 w_1 - \left.\frac{\partial M}{\partial x}\right|_L w_2 + w_\Gamma\left(\left.\frac{\partial M}{\partial x}\right|_{x_\Gamma^+} - \left.\frac{\partial M}{\partial x}\right|_{x_\Gamma^-}\right),\end{aligned} \tag{A.35}$$

resulting in the modified potential energy function:

$$\begin{aligned}\Pi = \int_0^{x_\Gamma^-} \left\{-\frac{1}{2EI}M^2 + \left(\frac{\partial^2 M}{\partial^2 x} - q(x)\right)w\right\} dx + [M\phi]_{x=0}^{x=x_\Gamma^-} + \frac{1}{2}k_t\Delta\phi^2 + \\ \left.\frac{\partial M}{\partial x}\right|_0 w_1 - \left.\frac{\partial M}{\partial x}\right|_L w_2 + w_\Gamma\left(\left.\frac{\partial M}{\partial x}\right|_{x_\Gamma^+} - \left.\frac{\partial M}{\partial x}\right|_{x_\Gamma^-}\right) + \\ \int_{x_\Gamma^+}^{L} \left\{-\frac{1}{2EI}M^2 + \left(\frac{\partial^2 M}{\partial^2 x} - q(x)\right)w\right\} dx + [M\phi]_{x_\Gamma^+}^{L} + W.\end{aligned} \tag{A.36}$$

Assuming no external force is applied on the fold and Equation A.29 to hold, we simplify the potential energy formulation one final time to:

$$\begin{aligned}\Pi = \int_{0}^{x_\Gamma^-} \left\{ -\frac{1}{2EI}M^2 + \left(\frac{\partial^2 M}{\partial^2 x} - q(x)\right) w \right\} dx + [M\phi]_{x=0}^{x=x_\Gamma^-} + \frac{1}{2}k_t \Delta\phi^2 + \left.\frac{\partial M}{\partial x}\right|_0 w_1 - \\ \left.\frac{\partial M}{\partial x}\right|_L w_2 + \int_{x_\Gamma^+}^{L} \left\{ -\frac{1}{2EI}M^2 + \left(\frac{\partial^2 M}{\partial^2 x} - q(x)\right) w \right\} dx + [M\phi]_{x_\Gamma^+}^{L} + W. \qquad \text{(A.37)}\end{aligned}$$

Two potential energy equations are derived, and will be used to discretize the folded beam. Equation A.36 contains w_Γ and will lead to a 6 DOF beam element, while Equation A.37 does not contain w_Γ which will lead to a 5 DOF foldable beam element.

B

Load application foldable beam

B.1. Equivalent load vector derivation

No interpolation field for the displacement is used in deriving the folded beam elements. This causes the application of a distributed force through an equivalent load vector to become difficult. In this section, it will be shown that with some extra calculations it is possible to apply a distributed load, and even a point load at the fold. All calculations are done using the 5 DOF system. A constant distributed load is applied to the system as:

$$q(x) = c. \tag{B.1}$$

In reality, this would lead to a quadratic shape of the moment field in the beam, since:

$$M(x) = \int q(x)dxdx = O(x^2), \tag{B.2}$$

we thus expect a residual error when calculating the displacements of the beam under a distributed load. The equivalent load vector is computed by discretizing the part in the potential energy term concerning distributed loads,

$$\int_0^{x_\Gamma^-} \left\{\frac{\partial^2 M}{\partial^2 x} - q(x)\right\} w dx + \int_{x_\Gamma^+}^{L} \left\{\frac{\partial^2 M}{\partial^2 x} - q(x)\right\} w dx. \tag{B.3}$$

Since linear shape functions are used for the moment field, $\partial^2 M/\partial x^2 = 0$, and this term can be removed from the equation. Only functions for the moment $M(x)$ are used in the discretization, and interpolations for the displacement field $w(x)$ need to be defined to construct an equivalent load vector. Combining Equation 2.6, the relation between moment and curvature, and the relation between rotation and curvature in Equation 2.4, we find:

$$\phi(\xi) = \frac{L}{k_{b1}} \int_0^{\xi_\Gamma^-} M(\xi)d\xi + \frac{L}{k_{b2}} \int_{\xi_\Gamma^+}^{1} M(\xi)d\xi. \tag{B.4}$$

Using the interpolation field as in Equation 2.27, the rotational field is calculated as:

$$\phi^L(\xi) = \frac{L}{k_{b1}} \left\{(\xi - \frac{1}{2}\xi^2)M_1 + \frac{1}{2}\xi^2 M_2 + C_1^L\right\} \text{ on } \Omega_1, \tag{B.5}$$

$$\phi^R(\xi) = \frac{L}{k_{b2}} \left\{(\xi - \frac{1}{2}\xi^2)M_1 + \frac{1}{2}\xi^2 M_2 + C_1^R\right\} \text{ on } \Omega_2. \tag{B.6}$$

Integrating once more, an expression for the displacement field is found as:

$$w^L(\xi) = \frac{L^2}{k_{b1}}\left\{(\frac{1}{2}\xi^2 - \frac{1}{6}\xi^3)M_1 + \frac{1}{6}\xi^3 M_2 + C_1^L\xi + C_2^L\right\} \text{ on } \Omega_1, \tag{B.7}$$

$$w^R(\xi) = \frac{L^2}{k_{b2}}\left\{(\frac{1}{2}\xi^2 - \frac{1}{6}\xi^3)M_1 + \frac{1}{6}\xi^3 M_2 + C_1^R\xi + C_2^R\right\} \text{ on } \Omega_2. \tag{B.8}$$

Four boundary conditions are needed to calculate the four different integration constants:

$$\phi(0) = \phi_1 \text{ and } \phi(1) = \phi_2, \tag{B.9}$$

$$w(0) = w_1 \text{ and } w(1) = w_2. \tag{B.10}$$

Inserting these conditions in the displacement function, results in the integration constants of:

$$C_1^L = \frac{\phi_1 k_{b1}}{L} \text{ and } C_2^L = \frac{w_1 k_{b1}}{L^2}, \tag{B.11}$$

$$C_1^R = \frac{\phi_2 k_{b2}}{L} - \frac{1}{2}(M_1 + M_2) \text{ and} \tag{B.12}$$

$$C_2^R = \frac{w_2 k_{b2}}{L^2} - \frac{1}{6}(2M_1 + M_2) - C_1^R = \frac{w_2 k_{b2}}{L^2} - \frac{\phi_2 k_{b2}}{L} + \frac{1}{6}(M_1 + 2M_2). \tag{B.13}$$

The displacement function, $w(\xi)$, contains both auxiliary DOFs from the vector $\boldsymbol{m}$, and primary DOFs from the vector $\boldsymbol{u}$. It follows that the discretized form of Equation B.3 will contain both auxiliary and primary DOFs. writing the left and right displacements in matrix form, we find:

$$w^L(\xi) = \boldsymbol{N}^L(\xi)\mathbf{m} + \boldsymbol{W}^L(\xi)\mathbf{u}, \tag{B.14}$$

$$w^R(\xi) = \boldsymbol{N}^R(\xi)\mathbf{m} + \boldsymbol{W}^R(\xi)\mathbf{u}, \tag{B.15}$$

$$\boldsymbol{N}^L(\xi) = \frac{L^2}{k_{b1}}[\frac{1}{2}\xi^2 - \frac{1}{6}\xi^3, \frac{1}{6}\xi^3], \tag{B.16}$$

$$\boldsymbol{N}^R(\xi) = \frac{L^2}{k_{b2}}[-\frac{1}{6}\xi^3 + \frac{1}{2}\xi^2 - \frac{1}{2}\xi + \frac{1}{6}, \frac{1}{6}\xi^3 - \frac{1}{2}\xi + \frac{1}{3}], \tag{B.17}$$

$$\boldsymbol{W}^L(\xi) = [1, L\xi, 0, 0, 0], \tag{B.18}$$

$$\boldsymbol{W}^R(\xi) = [0, 0, 1, L(\xi - 1), 0]. \tag{B.19}$$

Inserting $w(\xi)$ and $q(x)$ into Equation B.3, simplified using $\partial^2 M/\partial x^2 = 0$, we find:

$$\begin{aligned} -cL\int_0^{\xi_\Gamma^-} w(\xi)d\xi - cL\int_{\xi_\Gamma^+}^1 w(\xi)d\xi = -cL\int_0^{\xi_\Gamma^-} \left\{\boldsymbol{N}^L(\xi)\mathbf{m} + \boldsymbol{W}^L(\xi)\mathbf{u}\right\} d\xi \\ - cL\int_{\xi_\Gamma^+}^1 \left\{\boldsymbol{N}^R(\xi)\mathbf{m} + \boldsymbol{W}^R(\xi)\mathbf{u}\right\} d\xi = -\boldsymbol{L}^T\mathbf{m} - \mathbf{f}_c^T\mathbf{u}, \end{aligned} \tag{B.20}$$

where the equivalent load vector will be defined using:

$$\boldsymbol{L}^T = cL\int_0^{\xi_\Gamma^-} \boldsymbol{N}^L(\xi)d\xi + cL\int_{\xi_\Gamma^+}^1 \boldsymbol{N}^R(\xi)d\xi, \tag{B.21}$$

$$\mathbf{f}_c^T = cL\int_0^{\xi_\Gamma^-} \boldsymbol{W}^L(\xi)d\xi + cL\int_{\xi_\Gamma^+}^1 \boldsymbol{W}^R(\xi)d\xi. \tag{B.22}$$

In Equation B.21 there is an integration over a cubic function. In the stiffness matrix calculation, only quadratic terms are evaluated. Performing these calculations analytically, results in:

$$\boldsymbol{L} = \frac{L^3 c}{24 k_1 k_2} \begin{bmatrix} k_1(6\xi_\Gamma^2 - 4\xi_\Gamma + 1) + (k_2 - k_1)(4\xi_\Gamma^3 - \xi_\Gamma^4) \\ k_1(6\xi_\Gamma^2 - 8\xi_\Gamma + 3) + (k_2 - k_1)\xi_\Gamma^4 \end{bmatrix} \text{and} \tag{B.23}$$

$$\mathbf{f}_c = Lc \begin{bmatrix} \xi_\Gamma \\ \frac{L\xi_\Gamma^2}{2} \\ 1 - \xi_\Gamma \\ \frac{L(\xi_\Gamma - 1)^2}{2} \\ 0 \end{bmatrix}. \tag{B.24}$$

Inserting these terms in the potential energy derivation causes it to take a shape of:

$$\Pi = -\frac{1}{2}\mathbf{m}^T \boldsymbol{A}\mathbf{m} - \mathbf{m}^T \boldsymbol{B}\mathbf{u} + \frac{1}{2}\mathbf{u}^T \boldsymbol{K}_t \mathbf{u} - \mathbf{f}^T \mathbf{u} - \boldsymbol{L}^T \mathbf{m} - \mathbf{f}_c^T \mathbf{u}. \tag{B.25}$$

Following the known procedure to formulate the stiffness matrix, the equivalent load vector is calculated. Firstly, we vary with respect to **m**:

$$\partial\Pi = \frac{\partial\Pi}{\partial\mathbf{m}}\delta\mathbf{m} = \{-\boldsymbol{A}\mathbf{m} - \boldsymbol{B}\mathbf{u} - \boldsymbol{L}\}\delta\mathbf{m} = 0, \tag{B.26}$$

and rewrite to find the expression for **m**,

$$\mathbf{m} = -\boldsymbol{A}^{-1}\boldsymbol{B}\mathbf{u} - \boldsymbol{A}^{-1}\boldsymbol{L}. \tag{B.27}$$

Secondly, we vary with respect to **u**:

$$\partial\Pi = \frac{\partial\Pi}{\partial\mathbf{u}}\delta\mathbf{u} = \{-\mathbf{m}^T\boldsymbol{B} + \mathbf{u}^T\boldsymbol{K}_t - \mathbf{f}^T - \mathbf{f}_c^T\}\delta\mathbf{u} = 0, \tag{B.28}$$

and insert the term for **m**, making use of the fact that $\boldsymbol{A}$ is a symmetric matrix:

$$(\boldsymbol{B}^T\boldsymbol{A}^{-1}\boldsymbol{B} + \boldsymbol{K}_t^T)\mathbf{u} = \mathbf{f} + \mathbf{f}_c - \boldsymbol{B}^T\boldsymbol{A}^{-1}\boldsymbol{L}, \tag{B.29}$$

an equivalent load vector is found of the form:

$$\mathbf{f}_{el} = \mathbf{f}_c - \boldsymbol{B}^T\boldsymbol{A}^{-1}\boldsymbol{L}. \tag{B.30}$$

B.2. Testing the equivalent load vector

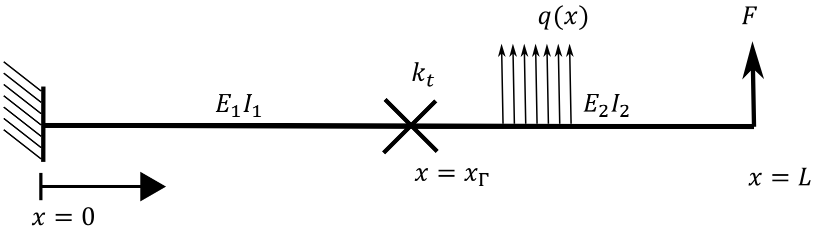

Figure B.1: A clamped folded beam loaded with a distributed force and an moment and force on the right end.

To test the application of the distributed forces on the beam, the test case as shown in Figure B.1 is used, with parameters as in Table B.1. A constant load is applied on the entire element. The 5 DOF system is compared to the assembled system, containing the 7 DOFs: $\mathbf{u}^T = [w_1,\ \phi_1,\ \phi_\Gamma^-,\ w_\Gamma,\ \phi_\Gamma^+,\ w_2,\ \phi_2]$. In the 7 DOF system, to account for the distributed force, an equivalent load vector is added as:

$$F_c^T = \begin{bmatrix} \frac{cL_a}{2} & \frac{cL_a^2}{12} & -\frac{cL_a^2}{12} & \frac{cL}{2} & \frac{cL_b^2}{12} & \frac{cL_b}{2} & -\frac{cL_b^2}{12} \end{bmatrix} \text{ where,} \tag{B.31}$$

EI [N m^2]	k$_t$[N m	F [N]	q(x) [N m^{-1}]	ξ_Γ
100	500	10	1	0.5

Table B.1: Values used in testing distributed force formulation.

$$L_a = L\xi_\Gamma \text{ and } L_b = L(\xi_\Gamma - 1). \tag{B.32}$$

As exact solution for the tip displacement at $x = L$, we use:

$$w_2 = w(x = L) = \frac{FL^3}{3EI} + \frac{cL^4}{8EI} + \frac{L_b\left(L_bF + \frac{1}{2}cL_b^2\right)}{k_t} \tag{B.33}$$

Both systems aThe defined equivalent load vector is thus sufficiently accurate to capture the behavior of the system when a constant distributed load is applied.

B.3. Applying a force on the fold

One possibility lacking in the 5 DOF system, which the 6 DOF system has, is the ability to add a force on the fold. Using the functions in Equations B.15 for the displacement of the beam, it is possible to apply a force on the fold in the 5 DOF system. In the potential energy derivation of the 5 DOF system, it is assumed that $F_\Gamma = 0$ and Equation A.29 should still hold resulting in a C^1-continuous moment field. After the discretization, F_Γ is again introduced into the modified potential energy dfunction:

$$W = F_1w_2 + M1\phi_1 - F_2w_2 - M_2\phi_2 - F_\Gamma w_\Gamma. \tag{B.34}$$

Doing this is not much different than how the distributed load is added. While discretizing, the distributed load is ignored, and we assume:

$$\int \left\{\frac{\partial^2 M}{\partial^2 x} - f(x)\right\} dx = 0, \tag{B.35}$$

but it is added when computing the equivalent load vector. In adding F_Γ we ignore it's existence in the modified potential energy formulation, and we assume:

$$\lambda_3 - \lambda_4 = F_\Gamma = 0, \tag{B.36}$$

and apply it after discretization, using an equivalent load vector. Either the left or right equation for the displacement field ,$w^L(\xi)$ or $w^R(\xi)$, can be used to calculate the fold displacement. The fold displacement is calculated using the left displacement field as shown in Equation B.15, resulting in:

$$w^L(\xi_\Gamma) = \boldsymbol{N}^L(\xi_\Gamma)\mathbf{m} + \boldsymbol{W}^L(\xi_\Gamma)\mathbf{u}, \tag{B.37}$$

$$\boldsymbol{N}^L(\xi_\Gamma) = \frac{L^2}{k_{b1}}[\frac{1}{2}\xi_\Gamma^2 - \frac{1}{6}\xi_\Gamma^3, \frac{1}{6}\xi_\Gamma^3], \tag{B.38}$$

$$\boldsymbol{W}^L(\xi_\Gamma) = [1, L\xi_\Gamma, 0, 0, 0]. \tag{B.39}$$

As in Equation B.20, the potential energy due to the load is expressed using the vectors $\boldsymbol{L}$ and $\mathbf{f}_c$. No integration is required to represent $-F_\Gamma w_\Gamma$, we find:

$$-F_\Gamma w_\Gamma = -\boldsymbol{L}^\intercal\boldsymbol{m} - \boldsymbol{f}_c^\intercal\boldsymbol{u}, \tag{B.40}$$

where the different terms are defined as:

$$L^T(\xi_\Gamma) = F_\Gamma \cdot \boldsymbol{N}^L(\xi_\Gamma) \text{ and } \mathbf{f}_c(\xi_\Gamma) = F_\Gamma \cdot \boldsymbol{W}^L(\xi_\Gamma). \tag{B.41}$$

The further derivation is equal to the derivation for the equivalent load vector for a distributed force, again resulting in Equation B.30. Using this equivalent load vector, the test case in Figure B.2 is used to compare the 6 and 5 DOF system, loaded by a force on the fold. As test parameters the values in Table B.1 are used, with an additional load on the fold of $F_\Gamma = 10$N. As analytical solution for the right tip displacement, we use:

$$w(x = L) = w_2 = \frac{L_b F L_a^2}{2EI} + \frac{(F + F_\Gamma)L_a^3}{3EI} + \frac{L_b(L_b * F + k_t \phi_\Gamma^-)}{k_t} + \frac{F L_b^3}{3EI}, \tag{B.42}$$

where,

$$\phi_\Gamma^- = \frac{L_b F L_a}{EI} + \frac{(F + F_\Gamma)L_a^2}{2EI}. \tag{B.43}$$

Both the 5 and 6 DOF system are found to achieve numerical accuracy when a force is applied on the fold.

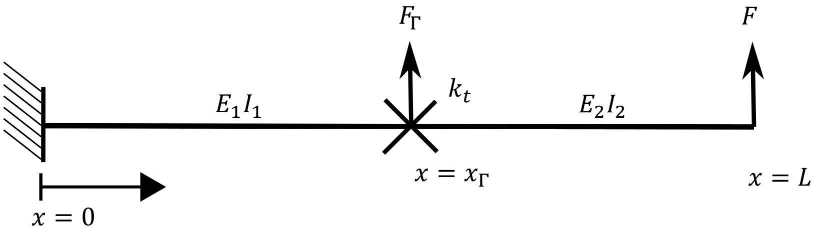

Figure B.2: A clamped folded beam loaded with by a force on the fold and a force at its free end. The parameters as in Table B.1 are used with an addition of a fold force of $F_\Gamma = 10$

C

Scaling of the 6 DOF system

In this appendix we investigate the possibility of improving the matrix condition of the 6 DOF beam system by introducing the scaling paramter s. Firstly, we introduce s using the method of IG-FEM [11] as:

$$M^6(\eta) = (1-\eta)M_1 + \eta M_2 + s \cdot \alpha \begin{cases} \frac{\eta}{\eta_\Gamma} & 0 \leq \eta \leq \eta_\Gamma \\ \frac{\eta-1}{\eta_\Gamma-1} & \eta_\Gamma \leq \eta \leq 1 \end{cases} . \tag{C.1}$$

We look at the matrices used in formulating the stiffness matrix, and notice on which locations the scaling parameter will multiply the values. For the $\boldsymbol{B}$-matrix, we find that it will be scaled by:

$$\boldsymbol{B}_s^6 = \begin{bmatrix} 1 & 1 & 1 & 1 & 1 & 1 \\ 1 & 1 & 1 & 1 & 1 & 1 \\ s & s & s & s & s & s \end{bmatrix},$$

and the $\boldsymbol{A}$-matrix is scaled by:

$$\boldsymbol{A}_s^6 = \begin{bmatrix} 1 & 1 & s \\ 1 & 1 & s \\ s & s & s^2 \end{bmatrix}.$$

Resulting in the scaling of the stiffness matrix:

$$\boldsymbol{K}_s^6 = \boldsymbol{B}_s^{6^T} \boldsymbol{A}_s^{6^{-1}} \boldsymbol{B}_s^6 = \begin{bmatrix} 1 & 1 & s \\ 1 & 1 & s \\ 1 & 1 & s \\ 1 & 1 & s \\ 1 & 1 & s \\ 1 & 1 & s \end{bmatrix} \begin{bmatrix} 1 & 1 & \frac{1}{s} \\ 1 & 1 & \frac{1}{s} \\ \frac{1}{s} & \frac{1}{s} & \frac{1}{s^2} \end{bmatrix} \begin{bmatrix} 1 & 1 & 1 & 1 & 1 & 1 \\ 1 & 1 & 1 & 1 & 1 & 1 \\ s & s & s & s & s & s \end{bmatrix}$$

$$= \begin{bmatrix} 1 & 1 & 1 & 1 & 1 & 1 \\ 1 & 1 & 1 & 1 & 1 & 1 \\ 1 & 1 & 1 & 1 & 1 & 1 \\ 1 & 1 & 1 & 1 & 1 & 1 \\ 1 & 1 & 1 & 1 & 1 & 1 \\ 1 & 1 & 1 & 1 & 1 & 1 \end{bmatrix}. \tag{C.4}$$

We thus conclude that straightforward scaling of the enrichment function will not change the stiffness matrix and its conditioning.

Since introducing a scaling parameter as commonly done in IGFEM has no effect on the matrix condtion number, other methods of introducing a scaling parameter to improve the

6 DOF condition number are investigated. A way of introducing the scaling parameter is by inserting it directly into the displacement vector as: $\mathbf{u}^\intercal = [w_1, \phi_1, w_2, \phi_2, s_w \cdot w_\Gamma, s_\phi \cdot \Delta\phi]$. Firstly only scaling w_Γ causes the elements in the $\boldsymbol{B}$-matrix to be scaled with:

$$\boldsymbol{B}^6_{w_\Gamma s} = \begin{bmatrix} 1 & 1 & 1 & 1 & \frac{1}{s_w} & 1 \\ 1 & 1 & 1 & 1 & \frac{1}{s_w} & 1 \\ 1 & 1 & 1 & 1 & \frac{1}{s_w} & 1 \end{bmatrix}, \tag{C.5}$$

and no change in the A matrix, resulting in the scaled stiffness matrix:

$$\boldsymbol{K}^6_{w_\Gamma s} = \begin{bmatrix} 1 & 1 & 1 & 1 & \frac{1}{s_w} & 1 \\ 1 & 1 & 1 & 1 & \frac{1}{s_w} & 1 \\ 1 & 1 & 1 & 1 & \frac{1}{s_w} & 1 \\ 1 & 1 & 1 & 1 & \frac{1}{s_w} & 1 \\ \frac{1}{s_w} & \frac{1}{s_w} & \frac{1}{s_w} & \frac{1}{s_w} & \frac{1}{s_w^2} & \frac{1}{s_w} \\ 1 & 1 & 1 & 1 & \frac{1}{s_w} & 1 \end{bmatrix}. \tag{C.6}$$

Scaling $\Delta\phi$ has similar effects, and results in the scaled stiffness matrix:

$$\boldsymbol{K}^6_{\Delta\phi s} = \begin{bmatrix} 1 & 1 & 1 & 1 & 1 & \frac{1}{s_\phi} \\ 1 & 1 & 1 & 1 & 1 & \frac{1}{s_\phi} \\ 1 & 1 & 1 & 1 & 1 & \frac{1}{s_\phi} \\ 1 & 1 & 1 & 1 & 1 & \frac{1}{s_\phi} \\ 1 & 1 & 1 & 1 & 1 & \frac{1}{s_\phi} \\ \frac{1}{s_\phi} & \frac{1}{s_\phi} & \frac{1}{s_\phi} & \frac{1}{s_\phi} & \frac{1}{s_\phi} & \frac{1}{s_\phi^2} \end{bmatrix}. \tag{C.7}$$

Calculating the matrix condition number as a function of the scaling at $\xi_\Gamma = 0.1$, and using zero rotational stiffness in the fold, results in Figure C.1 and C.2. The optimal scaling factor for w_Γ lies at infinity, but the condition number does not change significantly after a scaling of $s \approx 10$. The optimal scaling factor of $\Delta\phi$ is slightly below $s = 0.1$. Both scaling methods have a minimum condition number of $\chi \approx 1 \cdot 10^3$.

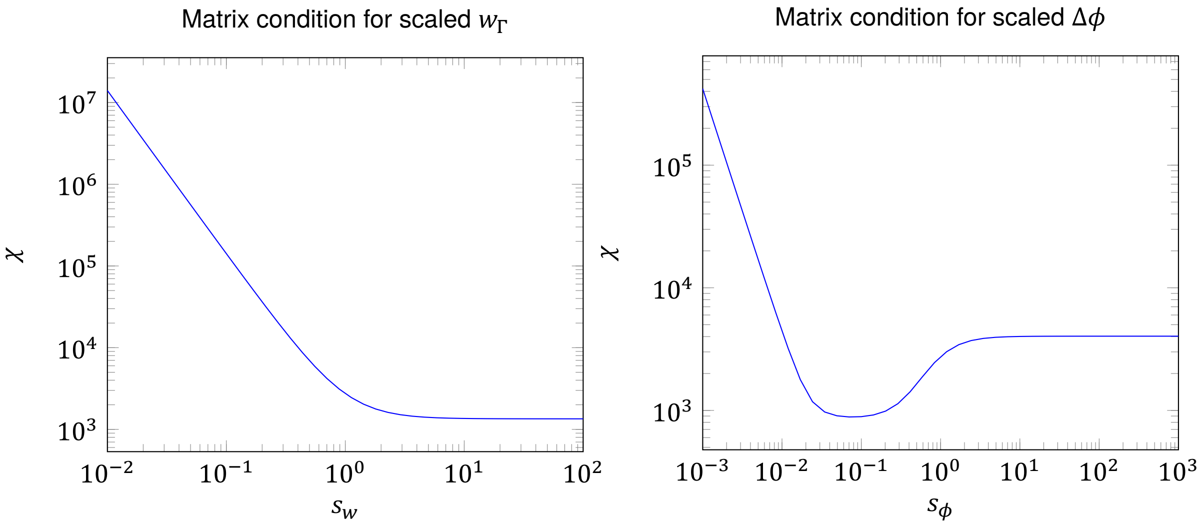

Figure C.1: The matrix condition of the 6 DOF system for varying the scaling s of w_Γ for a beam with a fold located at $\xi_\Gamma = 0.1$ and the material parameters as in Table 2.1, using zero fold stiffness

Figure C.2: The matrix condition of the 6 DOF system for varying the scaling s of $\Delta\phi$ for a beam with a fold located at $\xi_\Gamma = 0.1$ and the material parameters as in Table 2.1, using zero fold stiffness

To optimize the condition number, the scaling of w_Γ and $\Delta\phi$ is combined. By dividing w_Γ by s_w instead of multiplying, the condition plot is flipped along the vertical axis causing the two optima in Figure C.1 and C.2 to overlap. Using a scaling of $\mathbf{u}^\intercal = [w_1,\ \phi_1,\ w_2,\ \phi_2,\ \frac{w_\Gamma}{s},\ \Delta\phi \cdot s]$, the condition numbers as shown in Figure C.3 are found. The condition numbers are calculated using the material parameters found in Table 2.1, but with zero fold stiffness, the effects of the rotational stiffness are later examined. The optimal condition number decreased to

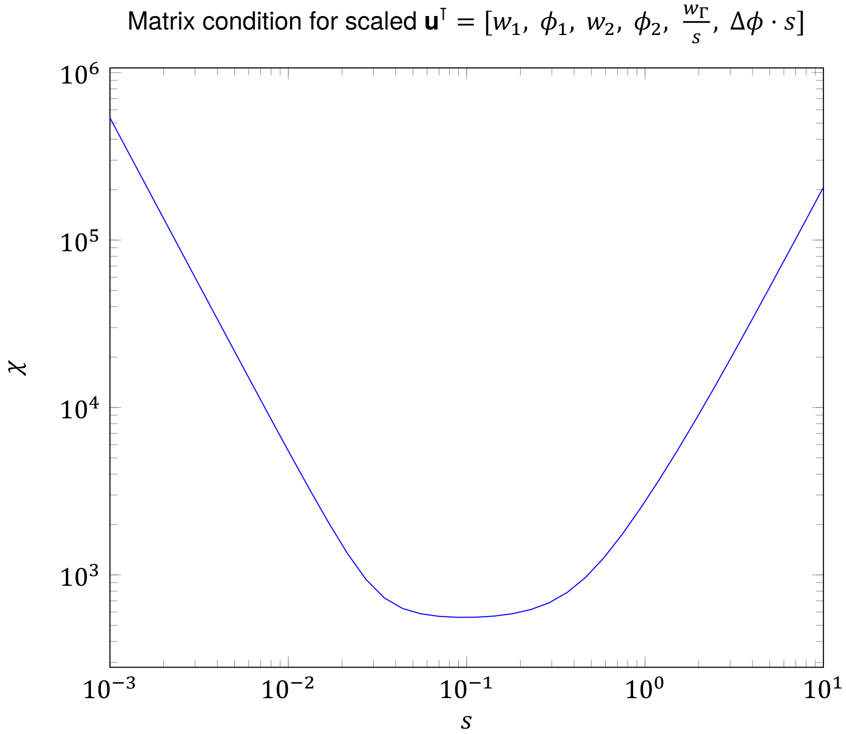

Figure C.3: The matrix condition of the 6 DOF system for varying the scaling s of $\mathbf{u}^\intercal = [w_1,\ \phi_1,\ w_2,\ \phi_2,\ \frac{w_\Gamma}{s},\ \Delta\phi \cdot s]$ for a beam with a fold located at $\xi_\Gamma = 0.1$ and the material parameters as in Table 2.1, but using zero fold stiffness.

$\chi \approx 558$, and can be found at $s^* \approx 0.1$. The beam stiffness k_b does not influence the condition number because it is used as a pre-multiplier of the stiffness matrix, although it is expected that choosing different k_1 and k_2 on the two subdomains of the beam will change the condition number. Adding higher values of k_t causes the matrix condition number to worsen and the optimal value of s to increase. It is noted that for $\frac{k_t}{k_b} < 50$ the optimizer does not change significantly, and only the optimal condition increases.

To improve the 6 DOF beam element, the optimal scaling s^* as a function of ξ_Γ is found in MATLAB using the optimizer fminbnd(). The DOFs are scaled using $\mathbf{u}^\intercal = [w_1, \phi_1, w_2, \phi_2, \frac{w_\Gamma}{s}, \Delta\phi\cdot s]$, and the problem is simplified by assuming no rotational stiffness at the fold, $k_t = 0$. Optimizing for a minimal matrix condition number results in the scaling in Figure C.4a, accompanied by the optimal condition in Figure C.4b. An estimate for the optimizer s^* is found as:

$$s(\xi_\Gamma) = (1 - \xi_\Gamma)\xi_\Gamma, \tag{C.8}$$

this function approximates the optimal scaling well at the borders of the domain but does not fit the optimal scaling well around $\xi_\Gamma = 0.5$. As can be seen in Figure C.4b, this does not matter much for the final condition number.

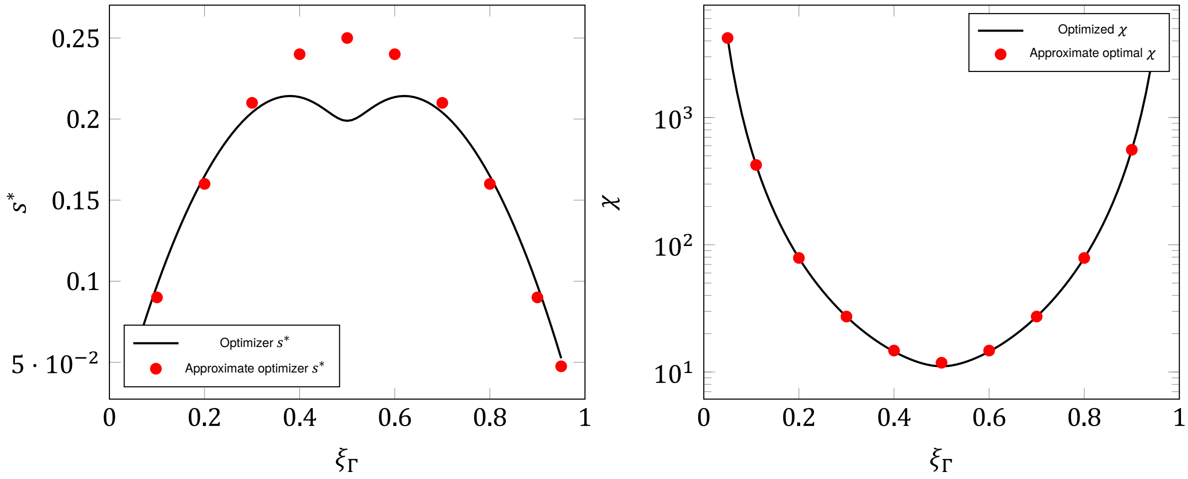

(a) The optimizer s^* for varying ξ_Γ.

(b) The optimal χ for varying ξ_Γ

Figure C.4: The optimal scaling factor s^* ,introduced as $\mathbf{u}^\intercal = [w_1, \phi_1, w_2, \phi_2, \frac{w_\Gamma}{s}, \Delta\phi\cdot s]$, and optimal matrix condition for a beam with varying fold location ξ_Γ using the material parameters as in Table 2.1. The optimized values are calculated in MATLAB and approximated with a scaling factor of $s(\xi_\Gamma) = (1 - \xi_\Gamma)\xi_\Gamma$.

An interpretation of the physical effect of the scaling function can be given by examining its effect on the enrichment function. In the 6 DOF B-matrix formulation, w_Γ is only multiplied by the enriched auxiliary DOF α at B_{53}, and not by the other auxiliary DOFs M_1 and M_2. In Equation 2.22, B_{53} represents the term:

$$B_{53} = \left.\frac{\partial M}{\partial x}\right|_{x_\Gamma^+} - \left.\frac{\partial M}{\partial x}\right|_{x_\Gamma^-} = \frac{1}{L}\left(\left.\frac{\partial \Psi}{\partial \xi}\right|_{\xi_\Gamma +} - \left.\frac{\partial \Psi}{\partial \xi}\right|_{\xi_\Gamma^-}\right), \tag{C.9}$$

which only includes derivatives of the enrichment function. Multiplying the enrichment function with the introduced scaling for w_Γ results in:

$$s(\xi_\Gamma)\cdot\begin{cases} \frac{\xi}{\xi_\Gamma} & 0 \le \xi \le \xi_\Gamma \\ \frac{\xi - 1}{\xi_\Gamma - 1} & \xi_\Gamma \le \xi \le 1 \end{cases} = (1 - \xi_\Gamma)\xi_\Gamma \cdot \begin{cases} \frac{\xi}{\xi_\Gamma} & 0 \le \xi \le \xi_\Gamma \\ \frac{\xi - 1}{\xi_\Gamma - 1} & \xi_\Gamma \le \xi \le 1 \end{cases} = \begin{cases} \xi(1 - \xi_\Gamma) & 0 \le \xi \le \xi_\Gamma \\ \xi_\Gamma(1 - \xi) & \xi_\Gamma \le \xi \le 1 \end{cases}, \tag{C.10}$$

which has a jump in derivative at the fold of:

$$\left.\frac{\partial \Psi}{\partial \xi}\right|_{\xi_\Gamma +} - \left.\frac{\partial \Psi}{\partial \xi}\right|_{\xi_\Gamma^-} = -\xi_\Gamma - (1 - \xi_\Gamma) = -1, \tag{C.11}$$

ensuring a constant jump in derivative independent of fold location. As can be seen in Equation 2.11, the jump in derivative of the moment field at the fold is equal to the force at the fold. By introducing this scaling factor the auxiliary DOF α is thus connected to the force at the fold and multiplied by the displacement at the fold in the $\boldsymbol{B}$-matrix. A possibility is that because the force and displacement at the fold are energetically conjugated, this results in better condition number.

D

5 DOF static beam condensation

Using the static condensation algorithm as described in [44], the 5 DOF folded beam element is condensed to a 4 DOF system. The stiffness matrix is split into a standard and an enriched part by defining the sub matrices:

$$\boldsymbol{K}^5 \cdot \boldsymbol{u} = \begin{bmatrix} \boldsymbol{K}_{11} & \boldsymbol{K}_{12} \\ \boldsymbol{K}_{21} & \boldsymbol{K}_{22} \end{bmatrix} \cdot \begin{bmatrix} \boldsymbol{u}^4 \\ \Delta\phi \end{bmatrix} = \begin{bmatrix} F_1 \\ M_1 \\ F_2 \\ M_2 \\ 0 \end{bmatrix} = \begin{bmatrix} \boldsymbol{f}^4 \\ 0 \end{bmatrix} \tag{D.1}$$

where $\boldsymbol{u}^{4^\intercal} = [w_1,\ \phi_1,\ w_2,\ \phi_2]$ is the standard displacement vector of a beam element, $\boldsymbol{K}_{11}$ the standard stiffness matrix of an Euler beam, $\boldsymbol{K}_{12}$ the 4 × 5 upper right part of $\boldsymbol{K}^5$ as,

$$\boldsymbol{K}_{12} = \begin{bmatrix} -\frac{6k_b(2\xi_\Gamma - 1)}{L^2} \\ -\frac{2k_b(3\xi_\Gamma - 2)}{L} \\ \frac{6k_b(2\xi_\Gamma - 1)}{L^2} \\ -\frac{2k_b(3\xi_\Gamma - 1)}{L} \end{bmatrix} \tag{D.2}$$

and $\boldsymbol{K}_{22}$ is the lower right part of $\boldsymbol{K}^5$ as:

$$\boldsymbol{K}_{22} = \frac{4k_b(3\xi_\Gamma^2 - 3\xi_\Gamma + 1)}{L} + k_t. \tag{D.3}$$

Due to the matrix symmetry, it is know that $\boldsymbol{K}_{12}^\intercal = \boldsymbol{K}_{21}$. The lower part of the system of equations is found as:

$$\boldsymbol{K}_{21}\boldsymbol{u}^4 + \boldsymbol{K}_{22}\Delta\phi = 0, \tag{D.4}$$

and rewritten to find an expression for the jump in rotation:

$$\Delta\phi = -\boldsymbol{K}_{22}^{-1}\boldsymbol{K}_{21}\boldsymbol{u}^4. \tag{D.5}$$

To remove the jump in rotation from the equation, the expression for $\Delta\phi$ is substituted into the upper part of the system of equations to find:

$$\boldsymbol{K}_{11}\boldsymbol{u}^4 + \boldsymbol{K}_{12}\Delta\phi = (\boldsymbol{K}_{11} - \boldsymbol{K}_{12}\boldsymbol{K}_{22}^{-1}\boldsymbol{K}_{21})\boldsymbol{u}^4 = \boldsymbol{f}^4, \tag{D.6}$$

resulting in the new enriched 4 × 4 stiffness matrix:

$$\boldsymbol{K}^4 = \boldsymbol{K}_{11} - \boldsymbol{K}_{12}\boldsymbol{K}_{22}^{-1}\boldsymbol{K}_{21}, \tag{D.7}$$

which is a symmetric stiffness matrix constructed from the standard Euler beam stiffness matrix, $\boldsymbol{K}_{11}$, with an enrichment representing energy terms of the jump in rotation. The formulated condensed stiffness matrix attained the same conditioning and numerical accuracy as the condensed stiffness matrix in Section 2.5.

E

Potential energy formulation for a folded plate

In this appendix, the full modified potential energy derivation for a foldable plate is discussed. The standard potential energy equation is derived including the bending stiffness, torsional stiffness in the fold, and the potential energy due to the applied loads as:

$$\Pi = \int_{\Omega_i} \left\{ \frac{1}{2} \boldsymbol{\kappa}^{\intercal} \boldsymbol{D} \boldsymbol{\kappa} - q w \right\} dA_i + \int_{\Gamma_F} \frac{1}{2} \boldsymbol{\phi}^{T} \intercal \boldsymbol{K}_T \Delta \boldsymbol{\phi} dS_F - \int_{\Gamma} [F_\Gamma w + \boldsymbol{m}_\Gamma \boldsymbol{\phi}_\Gamma] dS, \tag{E.1}$$

where the inegral over Ω_i represents the two integrals overr sub domains Ω_1 and Ω_2. The kinematic equations are added via Lagrange multipliers:

$$\begin{aligned} \Pi = \int_{\Omega_i} & \left\{ \frac{1}{2} \boldsymbol{\kappa}^{\intercal} \boldsymbol{D} \boldsymbol{\kappa} + \boldsymbol{\lambda}_{1,3} \cdot (\boldsymbol{\phi} - \nabla w) + \boldsymbol{\Lambda}_{2,4} : (\boldsymbol{C} - \nabla \boldsymbol{\phi}) - q w \right\} dA_i \\ & + \int_{\Gamma_F} \left\{ \frac{1}{2} \Delta \boldsymbol{\phi}^{\intercal} \boldsymbol{K}_T \Delta \boldsymbol{\phi} + \lambda_5 (w_\Gamma^1 - w_\Gamma) + \lambda_6 (w_\Gamma - w_\Gamma^2) \right\} dS_F - \int_{\Gamma} [F_\Gamma w + \boldsymbol{m}_\Gamma \boldsymbol{\phi}_\Gamma] dS, \end{aligned} \tag{E.2}$$

where $\boldsymbol{\lambda_1}$ and $\boldsymbol{\Lambda}_2$ are the Lagrange multipliers in sub-domain Ω_1, and $\boldsymbol{\lambda_3}$ and $\boldsymbol{\Lambda}_4$ are the Lagrange multipliers in sub-domain Ω_2. $\boldsymbol{\lambda_1}$ and $\boldsymbol{\lambda_3}$ are vectors and $\boldsymbol{\Lambda}_2$ and $\boldsymbol{\Lambda}_4$ are matrices. During the derivation the Lagrange multipliers will switch between vector and matrix notation, when the curvature switches between notations as:

$$\boldsymbol{\lambda} = \begin{bmatrix} \boldsymbol{\Lambda}_{11} & \boldsymbol{\Lambda}_{22} & \boldsymbol{\Lambda}_{12} \end{bmatrix}, \tag{E.3}$$

where we assume the Lagrange multipliers to be symmetric, $\boldsymbol{\Lambda}_{12} = \boldsymbol{\Lambda}_{21}$.

E.1. Interpretation of Lagrange multipliers

The Lagrange multipliers are interpreted by means of virtual variations. We firstly vary with respect to $\boldsymbol{\kappa}$:

$$\partial \Pi = \frac{\partial \Pi}{\partial \boldsymbol{\kappa}} \delta \boldsymbol{\kappa} = \int_{\Omega_i} \{ \boldsymbol{D} \boldsymbol{\kappa} + \boldsymbol{\lambda}_{2,4} \} \delta \boldsymbol{\kappa} dA_i = 0, \tag{E.4}$$

resulting in the Lagrange multipliers:

$$\boldsymbol{\lambda}_{2,4} = -D\boldsymbol{\kappa} = -\boldsymbol{m} \text{ on } \Omega_{1,2} \text{ or,} \tag{E.5}$$

$$\boldsymbol{\Lambda}_{2,4} = \boldsymbol{M}. \tag{E.6}$$

Back substituting Equation E.5, and substituting the relation between moment and curvature in Equation 3.8, we find:

$$\Pi = \int_{\Omega_i} \left\{ -\frac{1}{2}\boldsymbol{m}^\intercal D^{-1}\boldsymbol{m} + \boldsymbol{\lambda}_{1,3} \cdot (\boldsymbol{\phi} - \nabla w) + \boldsymbol{M} : \nabla\boldsymbol{\phi} - qw \right\} dA_i + \\ \int_{\Gamma_F} \left\{ \frac{1}{2}\Delta\boldsymbol{\phi}^T = \intercal\boldsymbol{K}_T\Delta\boldsymbol{\phi} + \lambda_5(w_\Gamma^1 - w_\Gamma) + \lambda_6(w_\Gamma - w_\Gamma^2) \right\} dS_F - \int_\Gamma [F_\Gamma w + \boldsymbol{m}_\Gamma\boldsymbol{\phi}_\Gamma]dS. \quad (E.7)$$

To interpret $\boldsymbol{\lambda}_{1,3}$ the function is varied with respect to $\boldsymbol{\phi}$:

$$\partial\Pi = \frac{\partial\Pi}{\partial\boldsymbol{\phi}}\delta\boldsymbol{\phi} = \int_{\Omega_i} \left\{ \boldsymbol{\lambda}_{1,3}\delta\boldsymbol{\phi} + \boldsymbol{M} : \nabla\delta\boldsymbol{\phi} \right\} dA_i + \int_{\Gamma_F} \Delta\boldsymbol{\phi}^\intercal\boldsymbol{K}_T\Delta\delta\boldsymbol{\phi}dS_F - \int_\Gamma \boldsymbol{m}_\Gamma \cdot \delta\boldsymbol{\phi}_\Gamma dS = 0 \quad (E.8)$$

The divergence within the first integration is simplified using integration by parts:

$$\int_{\Omega_i} \boldsymbol{M} : \nabla\delta\boldsymbol{\phi}dA_i = -\int_{\Omega_i} \delta\boldsymbol{\phi} \cdot (\nabla \cdot \boldsymbol{M})dA_i + \int_{\Gamma_i} \delta\boldsymbol{\phi}_\Gamma \cdot \boldsymbol{Mn}dS, \quad (E.9)$$

where $\boldsymbol{n}$ is the vector normal to the boundary in the $x - y$ plane. Substituting the integration by parts into the varied potential energy function:

$$\partial\Pi = \frac{\partial\Pi}{\partial\boldsymbol{\phi}}\delta\boldsymbol{\phi} = \int_{\Omega_i} \left\{ \boldsymbol{\lambda}_{1,3} \cdot \delta\boldsymbol{\phi} - \delta\boldsymbol{\phi} \cdot (\nabla \cdot \boldsymbol{M}) \right\} dA_i + \int_{\Gamma_i} \delta\boldsymbol{\phi}_\Gamma \cdot \boldsymbol{Mn}dS \\ + \int_{\Gamma_F} \Delta\boldsymbol{\phi}^\intercal\boldsymbol{K}_T\Delta\delta\boldsymbol{\phi}dS_F - \int_\Gamma \boldsymbol{m}_\Gamma \cdot \delta\boldsymbol{\phi}_\Gamma dS = 0. \quad (E.10)$$

The Lagrange multipliers can now be interpreted as:

$$\boldsymbol{\lambda}_{1,3} = \nabla \cdot \boldsymbol{M} \text{ on } \Omega_{1,2}. \quad (E.11)$$

Splitting the sub-domain boundaries Γ_i into $\Gamma_1' + \Gamma_2' = \Gamma$, and Γ_F, we find on the boundaries:

$$\int_{\Gamma_F} \left\{ \Delta\boldsymbol{\phi}^\intercal\boldsymbol{K}_T\Delta\delta\boldsymbol{\phi} + \boldsymbol{M}_\Gamma^1\boldsymbol{n}_1\delta\boldsymbol{\phi}_1 + \boldsymbol{M}_\Gamma^2\boldsymbol{n}_2\delta\boldsymbol{\phi}_2 \right\} dS_F + \int_\Gamma (\boldsymbol{Mn} - \boldsymbol{m}_\Gamma) \cdot \delta\boldsymbol{\phi}_\Gamma dS = 0, \quad (E.12)$$

and we conclude that on the outer element boundary:

$$\boldsymbol{Mn} = \boldsymbol{m}_\Gamma \text{ on } \Gamma. \quad (E.13)$$

Furthermore inserting the variational relation for the jump in rotation $\Delta\delta\boldsymbol{\phi} = \delta\boldsymbol{\phi}_1 - \delta\boldsymbol{\phi}_2$, we find on the fold line that:

$$\int_{\Gamma_F} \left\{ \Delta\boldsymbol{\phi}^\intercal\boldsymbol{K}_T(\delta\boldsymbol{\phi}_1 - \delta\boldsymbol{\phi}_2) + \boldsymbol{M}_\Gamma^1\boldsymbol{n}_1 \cdot \delta\boldsymbol{\phi}_1 + \boldsymbol{M}_\Gamma^2\boldsymbol{n}_2 \cdot \delta\boldsymbol{\phi}_2 \right\} dS_F \\ = \int_{\Gamma_F} \left\{ \left(\boldsymbol{K}_T\Delta\boldsymbol{\phi} + \boldsymbol{M}_\Gamma^1\boldsymbol{n}_1\right) \cdot \delta\boldsymbol{\phi}_1 - \left(\boldsymbol{K}_T\Delta\boldsymbol{\phi} - \boldsymbol{M}_\Gamma^2\boldsymbol{n}_2\right) \cdot \delta\boldsymbol{\phi}_2 \right\} dS_F, \quad (E.14)$$

resulting in moment continuity at the fold as:

$$\boldsymbol{K}_T\Delta\boldsymbol{\phi} = -\boldsymbol{M}_\Gamma^1\boldsymbol{n}_1, \quad (E.15)$$

$$\boldsymbol{K}_T\Delta\boldsymbol{\phi} = \boldsymbol{M}_\Gamma^2\boldsymbol{n}_2 = -\boldsymbol{M}_\Gamma^2\boldsymbol{n}_1, \quad (E.16)$$

$$\boldsymbol{M}_\Gamma^1\boldsymbol{n}_1 = \boldsymbol{M}_\Gamma^2\boldsymbol{n}_1. \quad (E.17)$$

Back substituting the Lagrange multipliers into the modified potential energy function all multipliers are removed from the domain integral:

$$\Pi = \int_{\Omega_i} \left\{ -\frac{1}{2}\boldsymbol{m}^\intercal\boldsymbol{D}^{-1}\boldsymbol{m} + \nabla \cdot \boldsymbol{M} \cdot \boldsymbol{\phi} - \nabla \cdot \boldsymbol{M} \cdot \nabla w + \boldsymbol{M} : \nabla\boldsymbol{\phi} - qw \right\} dA_i + \\ \int_{\Gamma_F} \left\{ \frac{1}{2}\Delta\boldsymbol{\phi}^\intercal K_T\Delta\boldsymbol{\phi} + \lambda_5(w_\Gamma^1 - w_\Gamma) + \lambda_6(w_\Gamma - w_\Gamma^2) \right\} dS_F - \int_\Gamma [F_\Gamma w + \boldsymbol{m}_\Gamma\boldsymbol{\phi}_\Gamma]dS. \quad (E.18)$$

To interpret the last multipliers, the function is varied with respect to w as:

$$\partial\Pi = \frac{\partial\Pi}{\partial w}\delta w = \int_{\Omega_i} \{-\nabla\cdot\boldsymbol{M}\cdot\nabla\delta w - q\delta w\}\,dA_i + \int_{\Gamma_F} \left\{\lambda_5(\delta w_\Gamma^1 - \delta w_\Gamma) + \lambda_6(\delta w_\Gamma - \delta w_\Gamma^2)\right\} dS_F$$
$$- \int_\Gamma F_\Gamma \delta w = 0. \quad \text{(E.19)}$$

Integration by parts is again used to simplify the term within the domain integral:

$$-\int_{\Omega_i} \nabla\cdot\boldsymbol{M}\cdot\nabla\delta w dA_i = \int_{\Omega_i} \delta w\cdot(\nabla\cdot(\nabla\cdot\boldsymbol{M}))dA_i - \int_{\Gamma_i} \delta w\cdot(\nabla\cdot\boldsymbol{M})\cdot\boldsymbol{n}_i dS_i$$
$$= -\int_{\Gamma_i} \delta w\cdot(\nabla\cdot\boldsymbol{M})\cdot\boldsymbol{n}_i dS_i, \quad \text{(E.20)}$$

where we use the fact that no quadratic shape functions for m will be used causing: $\nabla\cdot(\nabla\cdot\boldsymbol{M}) = 0$. Substituting the integration by parts into the varied functional we attain:

$$\partial\Pi = \frac{\partial\Pi}{\partial w}\delta w = -\int_{\Omega_i} q\delta w dA_i - \int_{\Gamma_i} \delta w\cdot(\nabla\cdot\boldsymbol{M})\cdot\boldsymbol{n}_i dS_i$$
$$+ \int_{\Gamma_F} \left\{\lambda_5(\delta w_\Gamma^1 - \delta w_\Gamma) + \lambda_6(\delta w_\Gamma - \delta w_\Gamma^2)\right\} dS_F - \int_\Gamma F_\Gamma \delta w dS = 0. \quad \text{(E.21)}$$

Splitting Γ_i into Γ_F and Γ_i', and combining Γ_i' into $\Gamma = \Gamma_1' + \Gamma_2'$ results in:

$$\int_{\Gamma_F} \left\{\delta w_\Gamma^1(\lambda_5 - (\nabla\cdot\boldsymbol{M}_\Gamma^1)\cdot\boldsymbol{n}_1) - \delta w_\Gamma^2(\lambda_6 + (\nabla\cdot\boldsymbol{M}_\Gamma^2)\cdot\boldsymbol{n}_2) + \delta w_\Gamma(\lambda_6 - \lambda_5)\right\} dS_F$$
$$- \int_{\Omega_i} q\delta w dA_i - \int_\Gamma \delta w\,\{F_\Gamma + (\nabla\cdot\boldsymbol{M})\cdot\boldsymbol{n}\}\,dS_F = 0. \quad \text{(E.22)}$$

We conclude for the Lagrange multipliers that:

$$\lambda_5 = (\nabla\cdot\boldsymbol{M}_\Gamma^1)\cdot\boldsymbol{n}_1 \text{ on } \Gamma_F, \quad \text{(E.23)}$$
$$\lambda_6 = -(\nabla\cdot\boldsymbol{M}_\Gamma^2)\cdot\boldsymbol{n}_2 \text{ on } \Gamma_F, \quad \text{(E.24)}$$
$$\lambda_5 = \lambda_6 \text{ on } \Gamma_F, \quad \text{(E.25)}$$

Where we note the effect of not applying a force on the fold, as was the case for the beam, this results in a C^1-continuous moment field throughout the plate. Furthermore, a relation between the moment and the force on the boundary is retrieved as:

$$F_\Gamma = -(\nabla\cdot\boldsymbol{M})\cdot\boldsymbol{n} \text{ on } \Gamma. \quad \text{(E.26)}$$

One term error term remains: $\int_{\Omega_i} q\delta w dA_i$, which is the potential energy term due to the applied surface pressure, and will be applied via an equivalent load vector after element discretization. Back substituting the Lagrange multipliers, a modified potential energy equation is found as:

$$\Pi = \int_{\Omega_i} \left\{-\frac{1}{2}\boldsymbol{m}^\intercal\boldsymbol{D}^{-1}\boldsymbol{m} + \nabla\cdot\boldsymbol{M}\cdot\boldsymbol{\phi} - \nabla\cdot\boldsymbol{M}\cdot\nabla w + \boldsymbol{M} : \nabla\boldsymbol{\phi}) - qw\right\} dA_i +$$
$$\int_{\Gamma_F} \left\{\frac{1}{2}\Delta\boldsymbol{\phi}^\intercal\boldsymbol{K}_T\Delta\boldsymbol{\phi} + (\nabla\cdot\boldsymbol{M})\cdot\boldsymbol{n}_1(w_\Gamma^1 - w_\Gamma) - (\nabla\cdot\boldsymbol{M})\cdot\boldsymbol{n}_2(w_\Gamma - w_\Gamma^2)\right\} dS_F$$
$$- \int_\Gamma [F_\Gamma w + \boldsymbol{m}_\Gamma\boldsymbol{\phi}_\Gamma] dS. \quad \text{(E.27)}$$

E.2. Simplification of the potential energy equation

Terms concerning w and $\boldsymbol{\phi}$ are still present in the surface integral. Since we only want to use a moment field interpolation on the surface, these terms need to be removed. We start by inserting the relation $\boldsymbol{n}_1 = -\boldsymbol{n}_2$ on Γ_F:

$$\Pi = \int_{\Omega_i} \left\{ -\frac{1}{2}\boldsymbol{m}^{\mathrm{T}}\boldsymbol{D}^{-1}\boldsymbol{m} + \nabla\cdot\boldsymbol{M}\cdot\boldsymbol{\phi} - \nabla\cdot\boldsymbol{M}\cdot\nabla w + \boldsymbol{M} : \nabla\boldsymbol{\phi} - qw \right\} dA_i + \\ \int_{\Gamma_F} \left\{ \frac{1}{2}\Delta\boldsymbol{\phi}^{\mathrm{T}}\boldsymbol{K}_T\Delta\boldsymbol{\phi} + (\nabla\cdot\boldsymbol{M})\cdot\boldsymbol{n}_1(w_\Gamma^1 - w_\Gamma^2) \right\} dS_F - \int_\Gamma [F_\Gamma w + \boldsymbol{m}_\Gamma\boldsymbol{\phi}_\Gamma] dS. \quad \text{(E.28)}$$

Secondly, the formulation is simplified by using integration by parts as:

$$\int_{\Omega_i} \boldsymbol{\phi}\cdot(\nabla\cdot\boldsymbol{M}) dA_i = -\int_{\Omega_i} \nabla\boldsymbol{\phi} : \boldsymbol{M} dA_i + \int_{\Gamma_i} \boldsymbol{\phi}\cdot\boldsymbol{M}\boldsymbol{n}_i dS_i, \quad \text{(E.29)}$$

and substituting it into the modified potential energy function:

$$\Pi = \int_{\Omega_i} \left\{ -\frac{1}{2}\boldsymbol{m}^{\mathrm{T}}\boldsymbol{D}^{-1}\boldsymbol{m} - \nabla\cdot\boldsymbol{M}\cdot\nabla w - qw \right\} dA_i + \int_{\Gamma_i} \boldsymbol{\phi}\cdot\boldsymbol{M}\boldsymbol{n}_i dS_i \\ \int_{\Gamma_F} \left\{ \frac{1}{2}\Delta\boldsymbol{\phi}^{\mathrm{T}}\boldsymbol{K}_T\Delta\boldsymbol{\phi} + (\nabla\cdot\boldsymbol{M})\cdot\boldsymbol{n}_1(w_\Gamma^1 - w_\Gamma^2) \right\} dS_F - \int_\Gamma [F_\Gamma w + \boldsymbol{m}_\Gamma\boldsymbol{\phi}_\Gamma] dS. \quad \text{(E.30)}$$

To remove ∇w from the integration over the sub-domains, integration by parts is again used:

$$\int_{\Omega_i} \nabla w\cdot(\nabla\cdot\boldsymbol{M}) dA_i = -\int_{\Omega_i} w\cdot(\nabla\cdot(\nabla\cdot\boldsymbol{M})) dA_i + \int_{\Gamma_i} w\cdot(\nabla\cdot\boldsymbol{M})\cdot\boldsymbol{n}_i dS_i \\ = \int_{\Gamma_i} w\cdot(\nabla\cdot\boldsymbol{M})\cdot\boldsymbol{n}_i dS_i, \quad \text{(E.31)}$$

where we again assume no quadratic or higher order shape functions will be used for $\boldsymbol{M}$. Substituting the equation in the modified potential energy function, we find:

$$\Pi = -\int_{\Omega_i} \left\{ \frac{1}{2}\boldsymbol{m}^{\mathrm{T}}\boldsymbol{D}^{-1}\boldsymbol{m} + qw \right\} dA_i - \int_{\Gamma_i} w\cdot(\nabla\cdot\boldsymbol{M})\cdot\boldsymbol{n}_i dS_i + \int_{\Gamma_i} \boldsymbol{\phi}\cdot\boldsymbol{M}\boldsymbol{n}_i dS_i \\ \int_{\Gamma_F} \left\{ \frac{1}{2}\Delta\boldsymbol{\phi}^{T}\boldsymbol{K}_T\Delta\boldsymbol{\phi} + (\nabla\cdot\boldsymbol{M})\cdot\boldsymbol{n}_1(w_\Gamma^1 - w_\Gamma^2) \right\} dS_F - \int_\Gamma [F_\Gamma w + \boldsymbol{m}_\Gamma\boldsymbol{\phi}_\Gamma] dS. \quad \text{(E.32)}$$

Again splitting Γ_i into Γ_i' and Γ_F, and combining Γ_i' into $\Gamma = \Gamma_1' + \Gamma_2'$ we attain:

$$\Pi = -\int_{\Omega_i} \left\{ \frac{1}{2}\boldsymbol{m}^{\mathrm{T}}\boldsymbol{D}^{-1}\boldsymbol{m} + qw \right\} dA_i - \int_{\Gamma} w\cdot(\nabla\cdot\boldsymbol{M})\cdot\boldsymbol{n} dS + \int_{\Gamma_i} \boldsymbol{\phi}\cdot\boldsymbol{M}\boldsymbol{n}_i dS \\ \int_{\Gamma_F} \left\{ \frac{1}{2}\Delta\boldsymbol{\phi}^{\mathrm{T}}\boldsymbol{K}_T\Delta\boldsymbol{\phi} + (\nabla\cdot\boldsymbol{M})\cdot\boldsymbol{n}_1(w_\Gamma^1 - w_\Gamma^2) - w_\Gamma^1\cdot(\nabla\cdot\boldsymbol{M})\cdot\boldsymbol{n}_1 - w_\Gamma^2\cdot(\nabla\cdot\boldsymbol{M})\cdot\boldsymbol{n}_2 \right\} dS_F \\ - \int_\Gamma [F_\Gamma w + \boldsymbol{m}_\Gamma\boldsymbol{\phi}_\Gamma] dS. \quad \text{(E.33)}$$

To remove w_Γ completely from the equation, the relation between $\boldsymbol{n}_1$ and $\boldsymbol{n}_2$ is inserted:

$$\Pi = -\int_{\Omega_i} \left\{ \frac{1}{2}\boldsymbol{m}^{\mathrm{T}}\boldsymbol{D}^{-1}\boldsymbol{m} + qw \right\} dA_i - \int_{\Gamma} w\cdot(\nabla\cdot\boldsymbol{M})\cdot\boldsymbol{n}_i dS_i + \int_{\Gamma_i} \boldsymbol{\phi}\cdot\boldsymbol{M}\boldsymbol{n}_i dS_i \\ \int_{\Gamma_F} \frac{1}{2}\Delta\boldsymbol{\phi}^{\mathrm{T}}\boldsymbol{K}_T\Delta\boldsymbol{\phi} dS_F - \int_\Gamma [F_\Gamma w + \boldsymbol{m}_\Gamma\boldsymbol{\phi}_\Gamma] dS. \quad \text{(E.34)}$$

Finally we again split boundaries Γ_i and use the relation between $\boldsymbol{n}_1$ and $\boldsymbol{n}_2$ on Γ_F to combine $\boldsymbol{\phi}_1$ and $\boldsymbol{\phi}_2$ into $\Delta\boldsymbol{\phi} = \boldsymbol{\phi}_1 - \boldsymbol{\phi}_2$ and find:

$$\Pi = -\int_{\Omega_i} \frac{1}{2}\boldsymbol{m}^{\mathrm{T}}\boldsymbol{D}^{-1}\boldsymbol{m}dA_i - \int_{\Gamma}\{w \cdot (\nabla \cdot \boldsymbol{M}) \cdot \boldsymbol{n} - \boldsymbol{\phi} \cdot \boldsymbol{M}\boldsymbol{n}\}\,dS + \int_{\Gamma_F}\left\{\frac{1}{2}\Delta\boldsymbol{\phi}^T\boldsymbol{K}_T\Delta\boldsymbol{\phi} + \Delta\boldsymbol{\phi} \cdot \boldsymbol{M}\boldsymbol{n}_1\right\}dS_F - \int_{\Gamma}[F_\Gamma w + \boldsymbol{m}_\Gamma\boldsymbol{\phi}_\Gamma]dS - \int_{\Omega_i} qwdA_i. \tag{E.35}$$

The modified potential energy equation for foldable plates is very similar to the modified potential energy equation for foldable beams. The functional contains four evaluations:

1. An integral over the element domain, which evaluates the bending energy in the element, and will be related to the $\boldsymbol{A}$-matrix
2. An evaluation on the outer element boundary Γ, which considers the energy due to the reaction forces of the element, and will be related to the $\boldsymbol{B}_S$-matrix
3. An evaluation on the fold Γ_F, which considers the torsional spring and the reaction forces of the element, and will be related to the $\boldsymbol{K}_t$-matrix and $\boldsymbol{B}_E$-matrix
4. An evaluation of the energy due to applied loads on the surface Ω and boundary Γ, which will be related to the load vector $\boldsymbol{f}$.

F

Further convergence analysis results on a square plate

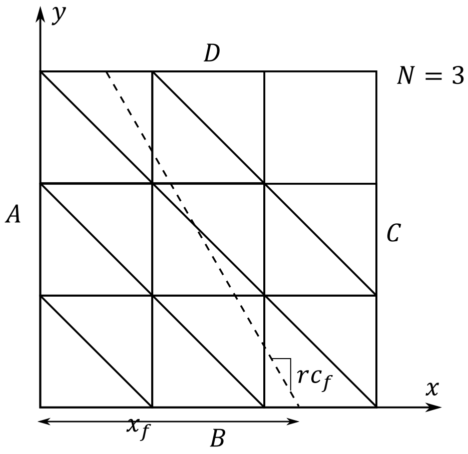

Figure F.1: A square plate discretized using N elements on each of its edges, resulting in a total of $N \times N$ triangular elements. Either a tilted fold is impose on the plate at $x = x_f - rc_f * x$, Side A is clamped and a distributed force F is applied on side C, or no fold is imposed on the plate side A is clamped, the rotation of sides B and D is fixed, and a constant pressure is applied on the pate's surface.

In Chapter 4, the convergence behavior of the square plate in Figure F.1 was investigated. Besides the results presented in Section 4.1, other results were generated which illustrate the degradation of the $KL1^{(2)}$-element convergence rate. Firstly, to illustrate the already low convergence rate of the foldable $KL1$ and HSM elements, a non-folded square plate is examined. The plate in Figure F.1 is used without imposing a fold, and thus only standard elements are used, side A is clamped, the rotation of sides B and D are fixed $\phi_n = 0$, and a pressure is applied on the plate's surface. Using the material parameters in Table 4.1, an analytical solution is derived as:

$$w^{(4)}(x) = \frac{PL(L-x)x^3}{3D} + \frac{PL(L-x)^2x^2}{4D} + \frac{Px^4}{8D} \tag{F.1}$$

resulting in the standard element convergence behavior found in Figure F.2. Due to the higher order moment field interpolation, the standard $KL1$-element achieved a convergence rate of $rc_{log} \approx -2$. Contrary to the convergence of $rc_{log} \approx -2$ found in Figure 4.7, the standard HSM-element only achieves a convergence rate of $rc_{log} = -1$. Investigating the results for the standard HSM elements is [37], the HSM element is also found to have varying convergence rates, for different test cases.

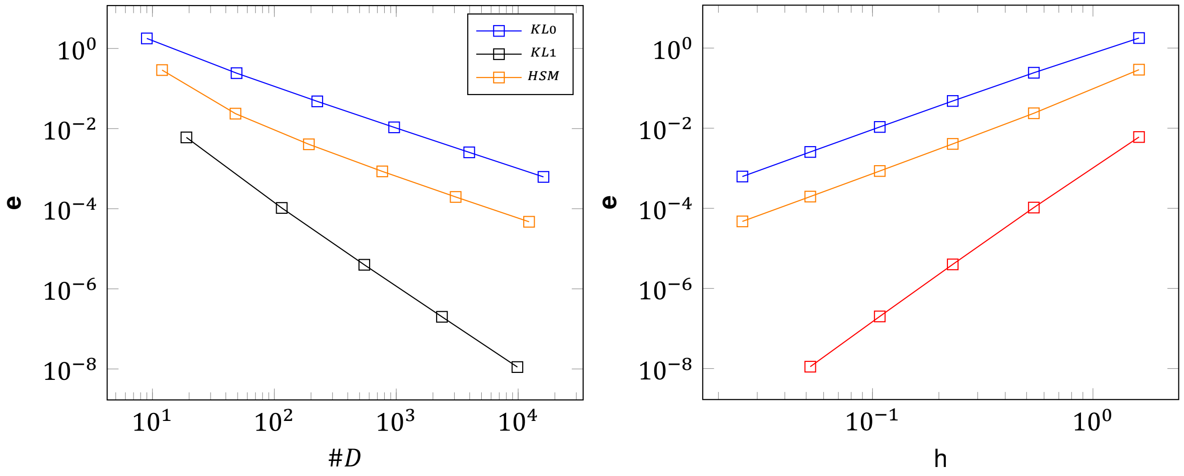

Figure F.2: The displacement error convergence of the folded plate in Figure F.1 where no fold is imposed on the system. Side A is clamped, the rotation of sides B and D is fixed $\phi_n = 0$, and a constant pressure is applied on the plate's surface. Since no fold is imposed only standard elements are used and the linear moment HSM and $KL1$ elements are found to attain higher convergence rates.

Secondly, some more tilted folds are examined, using the plate in Figure F.1, but with an imposed tilted fold. All further results in this Appendix are computed using a hinged $KL0$ element solution as a reference solution, following the method as described in Section 4.1. Subsequently, the displacement error is calculated using Equation 4.1. Firstly, a fold is inserted at $x_f = 0.51 - 0.1y$, resulting in Figure F.3. All foldable $KL0$ formulations converge as expected, the $KL1^{(2)}$-element converges slightly slower with a convergence rate of $rc_{log} \approx -0.95$. The $KL1^{(c)}$-element converges slightly faster, this is due to the decrease in enriched edge continuity error. Increasing the complexity of the problem, a fold is inserted at $x_f = 0.61 - 0.3y$, resulting in Figure F.4. The convergence rate of the $KL1^{(2)}$-element decreased even further to $rc_{log} \approx -0.82$. The convergence rate of the $KL1^{(c)}$-element begins relatively high. Since the $KL1^{(c)}$-element has an enriched edge continuity error, and the $KL1^{(2)}$ element does not, the $KL1^{(c)}$ error can not be lower than the $KL1^{(2)}$ error. When the $KL1^{(c)}$ error approached the $KL1^{(2)}$ error, the $KL1^{(c)}$ convergence rate decreases, and the $KL1^{(c)}$ error remains higher than the $KL1^{(2)}$ error. Finally, Figure F.5 shows the convergence rate when a fold is applied at $x_f = 0.21 + 0.5y$, in this figure it can clearly be seen that the convergence rates of the $KL1^{(2)}$ and $KL1(c)$ elements has degraded.

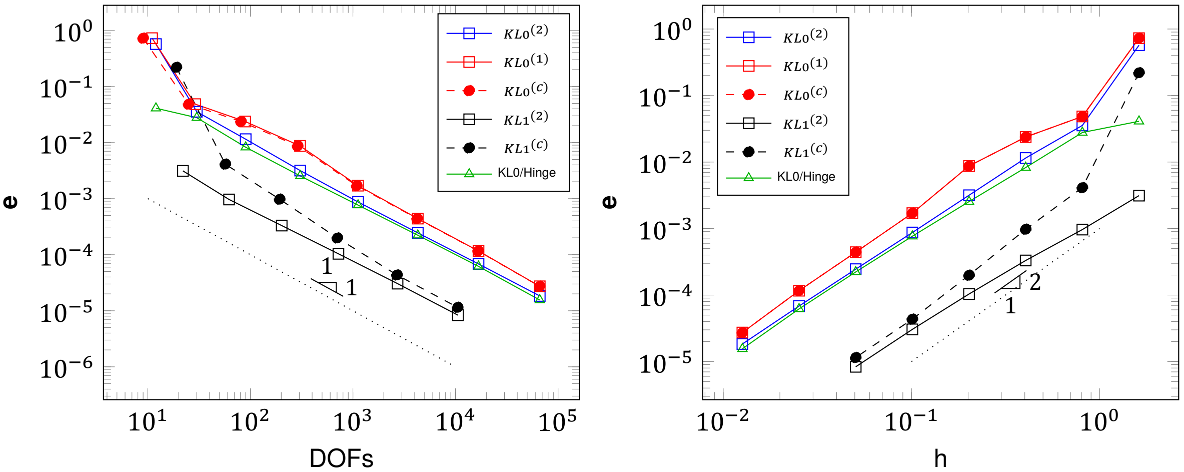

Figure F.3: The displacement error convergence of the folded plate in Figure F.1 using a hinged KL0 element on a reference mesh defined by $N_{ref} = 256$. As test parameters the values in Table 4.1 are used, side A is clamped and the distributed force is applied on side C. A fold is implemented at $x_f = 0.51 - 0.1y$.

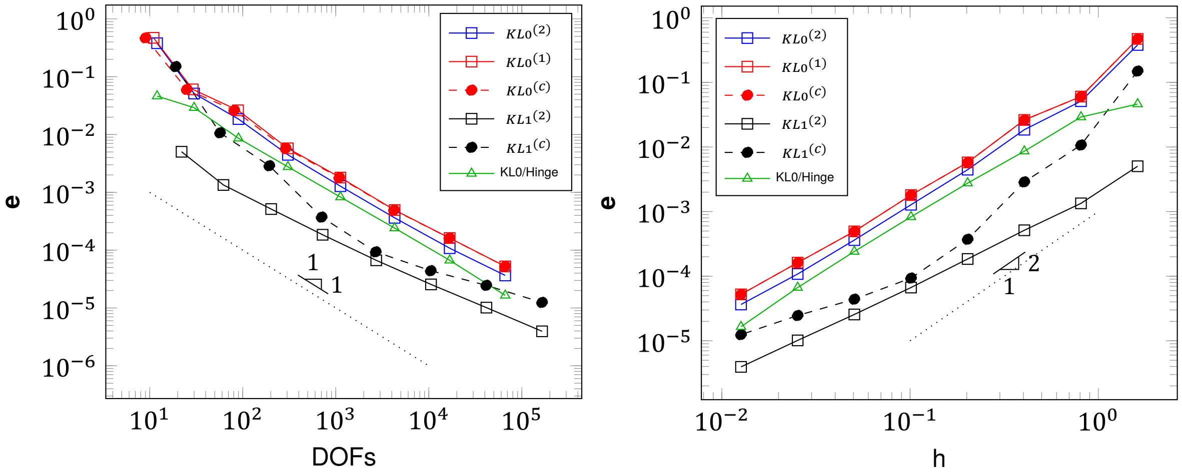

Figure F.4: The displacement error convergence of the folded plate in Figure F.1 using a hinged KL0 element on a reference mesh defined by $N_{ref} = 256$. As test parameters the values in Table 4.1 are used, side A is clamped and the distributed force is applied on side C. A fold is implemented at $x_f = 0.61 - 0.3y$.

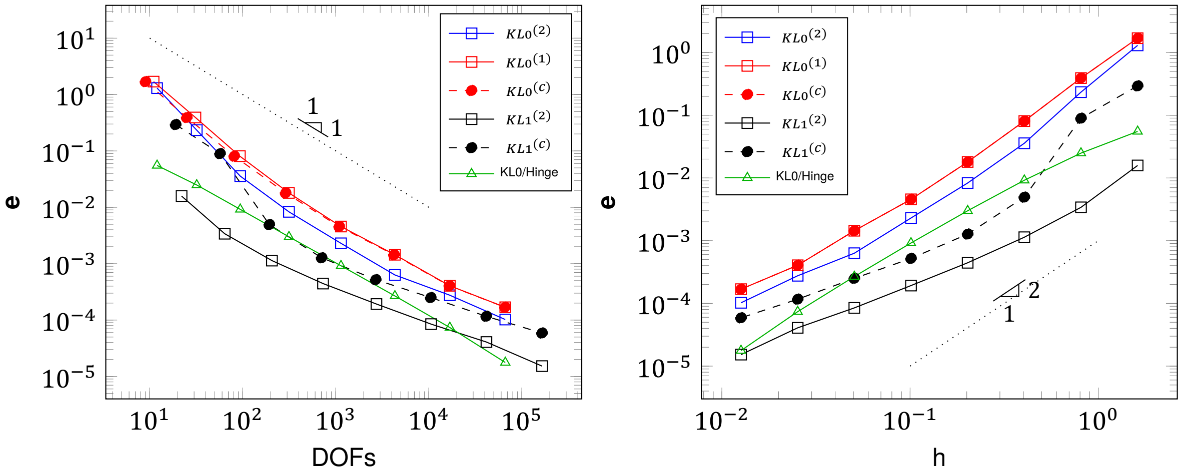

Figure F.5: The displacement error convergence of the folded plate in Figure F.1 using a hinged KL0 element on a reference mesh defined by $N_{ref} = 256$. As test parameters the values in Table 4.1 are used, side A is clamped and the distributed force is applied on side C. A fold is implemented at $x_f = 0.21 + 0.5y$.

G

Analytical solution circular fold

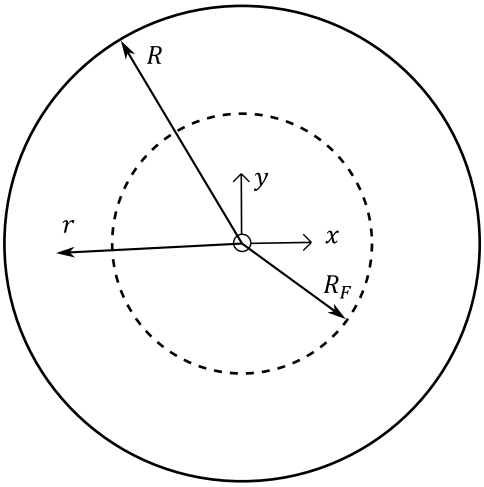

Figure G.1: A circular plate with radius R and a circular fold at radius $R_F < R$. The plate is simply supported on its outer edge, and a pressure is applied on its entire surface.

To analyze curved folds, an analytical solution is derived for the problem in Figure G.1. The problem consists of a circular plate of radius $R = 2$ m, clamped on its outer edge. A circular fold with radius $R_F = 1.5$ m is imposed on the plate, and a pressure of $q = -100\ \mathrm{N\,m^{-2}}$ is applied on its entire surface. Furthermore, the material parameters as in Table G.1 are used. The polar coordinate r is defined as the distance from the center of the plate. For a circular plate, loaded by a pressure on its surface a general solution is found in [46]:

$$\phi(r) = -\frac{dw}{dr} = -\frac{qr^3}{16D} - \frac{C_1 r}{2} - \frac{C_2}{r}, \tag{G.1}$$

$$w(r) = \frac{qr^4}{64D} + \frac{C_1 r^2}{4} + C_2 \ln r + C_3, \tag{G.2}$$

where the material parameter D is defined as:

$$D = \frac{Eh^3}{12(1-\nu^2)}. \tag{G.3}$$

Furthermore, the moment per unit length tangential to r is defined as:

$$M_r = D\left(\frac{d\phi}{dr} + \frac{\nu}{r}\phi\right) = -\frac{(3+\nu)qr^2}{16} - \frac{C_1 D(1+\nu)}{2} + \frac{C_2 D(1-\nu)}{r^2} \tag{G.4}$$

E [N m^{-2}]	k_t [N m rad^{-1} m^{-1}]	h [m]	ν	R [m]	R_F [m]	q [N m^{-2}]
$69 \cdot 10^9$	500	0.01	0.33	2	1.5	100

Table G.1: Values used in the circular plate calculations.

The problem is split into two domains:

$$\Omega^- = \{r : 0 \leq r < R_F\}, \tag{G.5}$$

$$\Omega^+ = \{r : R_F < r < R\}. \tag{G.6}$$

On the two domains, two solutions are defined:

$$\phi^-(r) = -\frac{dw}{dr} = -\frac{qr^3}{16D} - \frac{C_1^- r}{2} - \frac{C_2^-}{r}, \tag{G.7}$$

$$w^-(r) = \frac{qr^4}{64D} + \frac{C_1^- r^2}{4} + C_2^- \ln r + C_3^-, \tag{G.8}$$

on Ω^-, and

$$\phi^+(r) = -\frac{dw}{dr} = -\frac{qr^3}{16D} - \frac{C_1^+ r}{2} - \frac{C_2^+}{r}, \tag{G.9}$$

$$w^+(r) = \frac{qr^4}{64D} + \frac{C_1^+ r^2}{4} + C_2^+ \ln r + C_3^+, \tag{G.10}$$

on Ω^+. To interpret the constants six integration constants, C_1^-, C_2^-, C_3^-, C_1^+, C_2^+, C_3^+, six boundary conditions are defined. Firstly, due to the clamped outer edge, the rotation and displacement at $r = R$ are 0:

$$w^+(R) = 0, \tag{G.11}$$

$$\phi^+(R) = 0. \tag{G.12}$$

Furthermore, the displacement field at $r = R_F$ should be continuous:

$$w^+(R_F) - w^-(R_F) = 0. \tag{G.13}$$

Because the circular plate is a symetric problem, it can be assumed that there is no rotation at the center of the plate:

$$\phi^-(0) = 0. \tag{G.14}$$

The final two boundary conditions are constructed by imposing moment continuity at the fold. The moment per unit length at the fold due to the two displacement fields are defined:

$$M_r^- = -\frac{(3+\nu)qr^2}{16} - \frac{C_1^- D(1+\nu)}{2} + \frac{C_2^- D(1-\nu)}{r^2}, \tag{G.15}$$

$$M_r^+ = -\frac{(3+\nu)qr^2}{16} - \frac{C_1^+ D(1+\nu)}{2} + \frac{C_2^+ D(1-\nu)}{r^2}, \tag{G.16}$$

and the moment in the fold is defined as:

$$M_F = k_t \left(\phi^+(R_F) - \phi^-(R_F)\right). \tag{G.17}$$

Using these definitions the final two boundary conditions are defined as:

$$M_F - M_r^-(R_F) = 0, \tag{G.18}$$

$$M_F - M_r^+(R_F) = 0. \tag{G.19}$$

Using the symbolic toolbox in MatLab, the six integration constants are interpreted. As the found symbolic solution is quite lengthy, it is not displayed in this thesis. For the material parameters in Table G.1, the solution becomes:

$$w^-(r) = \frac{qr^4}{64D} + \frac{0.01057r^2}{4} - 0.00525, \tag{G.20}$$

$$w^+(r) = \frac{qr^4}{64D} + \frac{0.00923^+ r^2}{4} + -0.00297 \ln r + -0.00330. \tag{G.21}$$